

**MEASURING THE ANTINEUTRINO SPECTRUM AT THE DAYA BAY NUCLEAR
REACTORS**

by
Christine A. Lewis

A dissertation submitted in partial fulfillment of
the requirements for the degree of

Doctor of Philosophy
(Physics)

at the
UNIVERSITY OF WISCONSIN–MADISON
2014

Date of final oral examination: 2/4/2014

The dissertation is approved by the following members of the Final Oral Committee:

Karsten M. Heeger, Professor, Physics

Baha Akif Balantekin, Professor, Physics

Dan McCammon, Professor, Physics

Stefan Westerhoff, Professor, Physics

Paolo Desai, Associate Scientist, Astronomy and Physics

© Copyright by Christine A. Lewis 2014

All Rights Reserved

To Harvey Weinstock, who told me physics was hard.

ACKNOWLEDGMENTS

This thesis would not have been possible without the guidance and support of many people. First and foremost, I would like to thank my committee. Their patience and accommodation in scheduling my defense has been a great help. In particular, I would like to thank my advisor, Karsten Heeger. Throughout my graduate career he has provided me with the opportunities and challenges and encouragement that have enabled me to be successful.

Second, I would like to thank the whole Daya Bay Collaboration. Without the collective effort of my collaborators, there would be no Daya Bay Reactor Neutrino Experiment, and this thesis would not exist. I have particularly benefited from discussions, explanations, questions, and/or suggestions from Wei Wang, Yasu Nakajima, Dan Dwyer, Jiajie Ling, David Jaffe, Patrick Huber, and Weili Zhong. Wei and Yasu have both been hugely helpful responding to my questions and providing feedback on drafts of my analysis and cross-checking numbers. Any remaining inconsistency or inaccuracy is entirely my own fault.

Wei Wang was the post-doc in the UW Daya Bay group when I joined it, and has been an excellent role model of an effective scientist and all-around good person. I have appreciated the physics discussions, advice, practice-talk criticism, brainstorming, and moral support of Mike McFarlane, Bryce Littlejohn, Paul Hinrichs, and David Webber. Tom Wise was instrumental in getting the filling system together and I cannot imagine that filling would have gone smoothly without him.

In working on the filling system, I had the privilege of working with the many of the engineers and staff at PSL. They were universally brilliant, helpful, and a joy to work with. In particular, Harold Mattison, Dan Wenman, Darrell Hamilton, Jack Ambuel, and Jeff Cherwinka, and Qiang Xiao made my numerous trips out to Stoughton both pleasant and productive. On-site at Daya Bay,

Jeff made all things work-related go smoothly. He and Robin Cherwinka also kept me well-fed during many trips on-site and generally made Daya Bay feel more like home.

My classmates and friends have provided fun, laughter, and sanity. I especially appreciate the support and understanding of Laura Gladstone, Elliot Kaplan, Valerie Plaus, Eli Parke, Brad Madajczyk, and Ian Wisher. Nathan Wilson has been incredibly patient and understanding as my attempts finish and acquire gainful employment have made me increasingly stressed. By running errands, keeping me company, and gently encouraging me to keep trying, he has made the last few months doable.

Finally, I would like to acknowledge the strong, wholehearted support of my family. My grandparents and extended family have always encouraged and supported my academic endeavors. My brother assisted by being stationed in Hawaii just as filling travel left me burned-out and faced with an excessive frequent flyer mile problem. Lastly, I would like to thank my parents. They are responsible for the educational opportunities that set me on the path to graduate school in the first place. Their advice, encouragement, sympathy, and insistence that just quitting is a bad idea are the reasons I stayed.

TABLE OF CONTENTS

	Page
LIST OF TABLES	vii
LIST OF FIGURES	ix
NOMENCLATURE	xiv
ABSTRACT	xvi
1 Introduction	1
1.1 Organization of This Work	1
1.2 Neutrinos in the Standard Model	2
1.3 Electroweak Interactions	3
1.3.1 β Decay and the Creation of Reactor Antineutrinos	3
1.4 Oscillating neutrinos	5
1.4.1 Matter Effects and Resonance Oscillations	7
1.5 Experimental Mysteries in the Detection of Neutrinos	7
1.5.1 The Solar Anomaly	7
1.5.2 The Atmospheric Anomaly	8
1.6 Unknown Neutrino Properties	8
1.6.1 Number of Neutrinos	11
2 Experimental Landscape of Massive Neutrinos	13
2.1 The Quest For $\sin^2 2\theta_{13}$	13
2.1.1 CHOOZ	14
2.1.2 MINOS	15
2.1.3 T2K	15
2.1.4 Double Chooz	17
2.1.5 RENO	17
2.1.6 Daya Bay	18
2.2 Revisiting the Reactor Antineutrino Flux and Spectrum	19
2.2.1 Bugey 4	19
2.2.2 Bugey-3	20
2.2.3 Recent Developments	21

	Page
2.3 Summary	21
3 The Daya Bay Reactor Neutrino Experiment	23
3.1 Motivation	23
3.2 Experimental Site	24
3.3 Inverse Beta Decay Signal	27
3.3.1 Cross section	27
3.3.2 Backgrounds	28
3.4 Antineutrino Detection	28
3.4.1 Detector Liquids	30
3.4.2 Muon Veto	31
3.5 An Antineutrino Detector Event	32
3.5.1 Electronics and Trigger	33
3.5.2 Position and Energy Reconstruction	34
3.6 Signal Rate and Uncertainties	37
3.6.1 Target Protons	37
3.6.2 Detection Efficiencies	38
3.7 Inverse Beta Decay Data Selection	39
3.7.1 Vetoes	40
3.7.2 Coincidence selection	42
3.8 Backgrounds	45
3.8.1 Accidentals	45
3.8.2 Cosmogenic Isotopes	46
3.8.3 Fast Neutrons	46
3.8.4 AmC Neutron Source	48
3.8.5 $C(\alpha, n)$	48
3.9 Nominal Energy Response Model	48
3.9.1 Inner Acrylic Vessel Energy Loss	49
3.9.2 Nonlinearity of Energy Response	50
3.9.3 Energy Resolution	54
3.10 Summary	54
4 Predicted Reactor Antineutrino Spectrum	57
4.1 Conversion to Reconstructed Energy	59
4.2 Power Company Data	61
4.2.1 Fission Fraction Uncertainties	63
4.3 Energy Released Per Fission, e_i	64
4.4 Antineutrino Spectrum, $S_i(E)$	64

	Page
4.4.1 Interpolation and Extrapolation	66
4.4.2 Measured Component Uncertainties	66
4.4.3 ^{238}U Component Uncertainties	70
4.5 Non-equilibrium Corrections, $c_i(E, t)$	71
4.6 Spent Fuel Neutrinos	75
4.6.1 Estimated Magnitudes of SNF Contributions	78
4.6.2 Correlations Between Bins and Detectors	80
4.7 Final Nominal Prediction and Uncertainties	82
5 Analysis	85
5.1 Data Set	85
5.2 Nominal Model of the Inverse Beta Decay Spectra	86
5.2.1 The Nominal Prediction of the Data	87
5.3 The Oscillation Results	88
5.3.1 Discussion	90
5.4 Data Compared to Nominal Flux Models	91
5.4.1 Covariance Matrices and Uncertainty Combination	93
5.4.2 Results	95
5.4.3 Discussion	98
5.5 Conclusion	100
6 Conclusions	102
6.1 Reactor Prediction	102
6.2 Reactor Antineutrino Spectrum Role in Oscillation Results	103
6.3 Consistency of Nominal Reactor Predictions and Data	104
6.3.1 Impact of new U-238 Measurement	105
6.4 Future Prospects	105
LIST OF REFERENCES	107
APPENDIX The Daya Bay Antineutrino Detector Target Mass	118

LIST OF TABLES

Table	Page
2.1 CHOOZ systematic uncertainties, from[52].	15
3.1 Daya Bay detector overburdens, muon rates, mean muon energy. Numbers from [68] .	26
3.2 Distances (in meters) between reactors and detectors installed during this analysis. From [68].	26
3.3 Summary of detection efficiencies along with absolute (AD-correlated) and relative (AD-uncorrelated) uncertainties affecting the absolute expected rate. Numbers are consistent with those in [68]. Multiplicity and muon veto efficiencies vary by detector and are listed in Table 3.4.	55
3.4 The summary of IBD candidate events and expected backgrounds. From [69].	56
4.1 Correlations in simulated fission fraction variations between isotopes. From [111]. . .	63
4.2 Magnitudes of non-equilibrium corrections applied to each isotope at 2 MeV at the beginning and end of each core's fuel cycle. The values reflect the assumption that cores have 1/3 of the fuel irradiated for 0, 1, and 2 full fuel cycles. The size of the corrections falls of to zero by 4.5 MeV.	73
4.3 Summary of correlations in various prediction components. The energy released per fission and power uncertainties are not considered in detail in this work as they have negligible impact on spectral uncertainties.	83
4.4 Percent uncertainties on the measured IBD rate at a single Daya Bay detector from each input uncertainty in the reactor calculation.	84
5.1 Best-fit oscillation results when starting from the new and old reactor models. Uncer- tainties listed on the oscillation parameters are directly from the fitter. They closely match the values obtained in a scan of the parameter space around the minimum. . . .	89

Table	Page
5.2 The χ^2/dof for the comparison of expected and observed spectra after normalizing each predicted spectrum to the data. The observed spectrum does not match either reactor model.	95

LIST OF FIGURES

Figure	Page
1.1 The ratio of measured to expected ν_e and ν_μ type events as a function of L/E. Reproduced from [9].	9
2.1 Measured positron spectrum from CHOOZ and expected spectrum with no oscillation after background subtraction (top) and the ratio of measurement to expectation (bottom). All errors are statistical. Reproduced from [52].	16
2.2 The comparison of Bugey-3's positron spectrum with the expectation based on the converted ILL β spectra. Errorbars are statistical and the errorband includes the quoted ILL uncertainties and a 0.8% energy scale uncertainty. Reproduced from [77].	20
3.1 Layout of the Daya Bay experimental site. From [90].	25
3.2 Approximate proportions of IBD events during the data period analyzed in this work coming from each of the reactors.	26
3.3 Annotated cut-away drawing of an AD. From [90].	29
3.4 Diagram of the electronics. From [66].	33
3.5 The mean single p.e. PMT gain as a function of time. From [100].	35
3.6 The stability of the energy scale in each detector as a function of time. A degradation of slightly more than 1%/year is observed. From [100].	35
3.7 The stability of the neutron capture peak on Gd over time in each detector. From [100].	36
3.8 The relative Gd neutron capture peak between the detectors. The relative energy scale uncertainty between ADs is taken to be spread of these points, or 0.35%. From [100] .	37

Figure	Page
3.9 The singles spectrum illustrating the reduction of spurious signal by the flasher cut and the muon veto. The peak at 8 MeV is from neutron captures on Gadolinium, which forms the delayed component of the IBD signal. The bottom image shows the distribution of coincidences with in prompt and delayed energy. The red region contains the IBD signal.	41
3.10 A characteristic flasher hit pattern (left). The flasher discriminator used in IBD selection (right). From [68]	41
3.11 The neutron capture time for coincidences in all six detectors. From [100].	43
3.12 The distribution of delayed events in energy. The uncertainty on the delayed energy cut comes from the proportion of events around 6 MeV. From [100].	44
3.13 The expected background spectrum for AD1 for the full 6-AD data set. Contributions from individual components are shown.	45
3.14 The accidental rates in each AD as a function of time during the data period considered in this work. From [100]	46
3.15 Distribution of events as a function of time since last muon. The 0 ms to 1000 ms region comes from cosmogenic isotopes ^9Li and ^8He . At longer times, the distribution shows the uncorrelated background. From [100].	47
3.16 The IAV energy loss conversion matrix. From [107]	49
3.17 The ratio of reconstructed to expected energy from calibration sources and radioactive decays in the singles spectrum. From [69]	51
3.18 The measured ^{12}B spectrum compared to the expectation from the nominal detector nonlinearity model. From [69]	52
3.19 The nominal nonlinearity model compared to measured β spectra from ^{12}B and additional backgrounds. From [100]	52
3.20 The nominal positron nonlinearity and uncertainty band obtained from combining alternative models. From [69, 109].	52
3.21 Correlation matrix (left) for detector energy nonlinearity uncertainties in detected IBD spectrum and corresponding fractional uncertainties at each AD (right).	53

Figure	Page
3.22 The energy resolution compared to peak positions of various gammas in the detector. From [69]	54
4.1 Neutrino energy to prompt (positron plus annihilation gamma) energy conversion.	60
4.2 In neutrino energy, the IBD rate (top, left) and spectrum (top, right) variations induced at AD1 for 500 variations in the fission fractions. After conversion to reconstructed energy, the proportional uncertainties in the final analysis bins for the IBD spectrum at each AD (bottom left) and correlation matrix (bottom right) are also shown.	65
4.3 The IBD spectrum uncertainties from Huber[19] with ^{238}U from [81] (left) and original ILL conversion[72, 73] with ^{238}U from [88]. The outer band shows the total specified uncertainty for each isotope assuming 0.25 MeV bins; the inner band shows the energy and isotope-correlated components	67
4.4 The ratio between the expected IBD spectrum calculated using the ILL converted beta spectra to the expectation using the Huber conversion. Differences at each hall are plotted separately to illustrate that differences in predicted IBD spectra are similar at each hall for the six-AD data period, irrespective of the reactor model.	67
4.5 The fraction of IBDs coming from each isotope as a function of neutrino energy for the Huber (left) and ILL (right) models. The majority of IBDs come from ^{235}U , however extrapolation of the spectrum above 8 MeV leads to an apparent dominance of ^{238}U at higher energy. The actual composition above 8 MeV is not well known.	68
4.6 Fractional uncertainties at each AD from the energy and isotope correlated components of the β to ν conversion procedure (left). The corresponding correlation matrix is shown for final analysis bins in all detectors (right).	69
4.7 Fractional uncertainties at each AD from the energy and isotope uncorrelated components of the β to ν conversion procedure (left). The corresponding correlation matrix is shown for final analysis bins in all detectors (right).	70
4.8 ^{238}U uncertainty bands and fractional uncertainties in the predicted IBD spectrum for each AD in the energy-correlated case (top left) and the corresponding correlation matrix (top right). Lower plots show the fractional uncertainties and correlations where ^{238}U uncertainties are treated as uncorrelated in energy.	72
4.9 Fraction of IBDs attributable to the non-equilibrium correction at AD1.	74

Figure	Page
4.10 Fractional uncertainties at each AD from non-equilibrium corrections (left) and the associated correlation matrix for final analysis bins in all detectors (right).	75
4.11 The estimated antineutrino flux from the spent fuel pool corresponding to the most-recently-removed fuel assemblies for each of the six reactor cores (top). Increases correspond to core shutdowns, for which fuel remaining in the core is treated as “effective” SNF. The approximate age of the most-recently-removed fuel assemblies calculated as days since the beginning of each core’s last shutdown (bottom).	77
4.12 Total predicted SNF events over the data period corresponding to this analysis (left). Fraction of total expected IBD events ($/0.05$ MeV) attributed to SNF at AD1 illustrating the impact of in-core decays during reactor shutdown periods (right).	78
4.13 Total predicted SNF events over the data period corresponding to this analysis (left). Fraction of total expected IBD events ($/0.05$ MeV) attributed to SNF at AD1 illustrating the impact of previously unloaded fuel on the prediction (right).	79
4.14 Total predicted SNF events over the data period corresponding to this analysis (left). Fraction of total expected IBD events ($/0.05$ MeV) attributed to SNF at AD1. Cyan corresponds to the nominal SNF prediction used (right).	80
4.15 Fractional uncertainties at each AD from SNF (left) and the associated correlation matrix (right).	81
4.16 Fractional uncertainty in the IBD spectrum for each component of the reactor prediction that causes variations in the spectrum shape. ^{238}U uncertainties are treated as uncorrelated between energy bins and are included with uncorrelated β conversion uncertainty. Uncertainties are shown as a function of neutrino energy before adjustments for detector response.	82
4.17 Correlations between 0.25 MeV bins due to the combination of reactor component uncertainties.	83
5.1 The ratio of data to best-fit spectrum in each hall. Error bars correspond to the statistical uncertainties on the data.	90

Figure	Page
5.2 The expected total prompt spectrum for the six-AD data period based on the nominal ILL (blue) and Huber (red) flux models and nominal detector response (left). Each prediction has been normalized to the data and all ADs are combined. Measured prompt spectra are shown (black points) with statistical uncertainties. The right figure shows the fractional difference between the data and the prediction, with statistical errors added to the Huber model for reference.	91
5.3 The fractional difference between nominal predictions and observed data for the Huber (red) and ILL (blue) models for individual ADs. Each predicted spectrum has been normalized to the data from the corresponding AD. Statistical errors are included on the Huber curve for reference.	92
5.4 An example matrix, C , combining initial calculation bins for six ADs into final analysis bins for three halls.	94
5.5 For the Huber reactor fluxes, the covariance (top left) and correlation (top right) matrices corresponding to the nominal reactor model. The lower figures show the covariance (left) and correlation (right) matrices with the conservative detector nonlinearity uncertainty also included.	96
5.6 The difference between observed and expected events compared to the Huber (left) and ILL (right) reactor models and detector nonlinearity uncertainties. In each case, the predicted spectrum and prediction covariance matrix have been normalized to match the total number of observed events. Error bars represent the statistical uncertainty of the data with all ADs combined. The inner error bands are from the diagonal elements of the reactor prediction covariance matrix. The outer error bands are from the diagonal elements of the prediction covariance matrix where the positron nonlinearity uncertainty is also included.	97
5.7 The contribution to the overall χ^2 from each analysis bin.	97
6.1 Measurement precision for this data set and projected sensitivity to the small mixing angle and mass splitting Δm_{ee}^2 including data from full eight detector running. From [129].	106

NOMENCLATURE

ACU	Automatic calibration unit
AD	Antineutrino Detector
ADC	Analog-to-digital converter
CC	Charged current
DYB	Daya Bay
D1, D2	Guangdong (Daya Bay) reactors 1 and 2
FEE	Front-end electronics
GdLS	Gd-doped Liquid Scintillator
IAV	Inner acrylic vessel
IBD	Inverse beta decay
ILL	Institute Laue-Langevin, site of measurements of beta spectra from ^{235}U , ^{239}Pu , and ^{241}Pu fission.
L1, L2, L3, L4	Ling Ao reactors 1 through 4
LAB	Linear alkyl benzene
LS	Liquid Scintillator

MO	Mineral Oil
NC	Neutral current
NPP	Nuclear power plant
OAV	Outer acrylic vessel
p.e./PE	Photoelectron
PMT	Photomultiplier tube
SSV	Stainless steel vessel
SNF	Spent nuclear fuel
TDC	Time-to-digital converter

ABSTRACT

The Daya Bay Reactor Antineutrino Experiment is a multi-detector oscillation experiment that has used antineutrinos produced at the Guangdong and Ling Ao nuclear reactors in Southern China to measure the neutrino mixing angle $\sin^2 2\theta_{13}$ and the mass-splitting Δm_{ee}^2 . Between December 24, 2011 and July 28, 2012, the experiment collected 338310 candidate inverse beta decay events with six, 20-ton detectors placed at varying distances from the reactor cores. This work calculates the expected antineutrino flux and spectrum at all Daya Bay detectors from models of the reactor spectrum and compares the predictions to the observation to evaluate their consistency. This is of interest because of an apparent deficit, the “reactor neutrino anomaly,” noted in 2011 between measured antineutrino fluxes and the most recent reactor flux model predictions. In this work, we find an excess of events in the 5 MeV region of the observed spectrum. It is demonstrated that this excess is inconsistent with the commonly used reactor models, and does not appear to be consistent with the detector response. The cause of the excess has not been determined, but some avenues of further investigation are discussed. Additionally, we verify that in a three-neutrino oscillation picture with the current detector response model, Daya Bay’s oscillation results are independent of the underlying reactor model.

Chapter 1

Introduction

Neutrinos first became a challenge for scientists in the early 20th century. Between 1914 and 1930, Chadwick, Ellis, Meitner, Hahn, and others studying the decay of radioactive nuclei found continuous energy spectra for beta decay, which had been presumed to be a two-body decay. Conservation of energy in a two-body decay should lead to a discrete energy spectrum. In 1930, Wolfgang Pauli proposed that an additional massless, electrically-neutral particle participated in beta decays, carrying away energy[1]. Fermi incorporated this “little neutral particle,” or neutrino, in his theory of beta decay in 1934[2, 3]. It took more than two decades before the existence of neutrinos was experimentally confirmed by Reines and Cowan at a nuclear reactor[4, 5].

Since then, neutrinos have continued to be the subject of several mysteries in physics. Measurements of the neutrino flux from the Sun led to the solar neutrino problem, in which approximately 30% of predicted neutrinos were observed[6, 7]. Measurements of neutrinos produced in cosmic-ray-induced showers in the atmosphere showed an anomalous ratio of electron to muon-flavor neutrinos[8]. Within the last 20 years, these mysteries were resolved with the conclusive demonstration that neutrinos oscillate between flavors as they propagate[9, 10, 11].

1.1 Organization of This Work

Subsequent sections of this chapter contain introductory material describing the general history of neutrinos and the theoretical background pertaining to neutrino oscillations and the production and detection of reactor antineutrinos. Chapter 2 provides an overview of our experimental knowledge of neutrinos and current mysteries in the field. Chapter 3 describes the goals of the Daya

Bay Reactor Neutrino Experiment, the experimental site, detector technology, and event selection. Chapter 4 provides a general overview of neutrino production in nuclear power reactors and describes the prediction of the signal spectrum at each of the Daya Bay detectors. For each component of the calculation that effects the spectrum, the treatment of possible correlation between isotopes, energies, reactor cores, and detectors is described. Chapter 5 includes results of the Daya Bay's relative rate plus spectral shape oscillation results and analyzes the agreement between the predicted and measured spectra. Chapter 6 summarizes the results of Chapters 4 and Chapter 5 and discusses some of their implications for further analysis and future results. Appendix A reproduces a paper[12] written on the process of filling the antineutrino detectors and its implications for the relative mass uncertainty between detectors.

Original Contributions of This Work The Daya Bay Reactor Neutrino Experiment is a collaborative effort of more than two hundred scientists. The contribution of this work to the experiment's construction is in the area of detector filling, which is described in the Appendix. In support of Daya Bay's physics analyses, data from the filling system and target mass monitoring systems produce the expected target mass of each detector along with the uncertainty on the mass differences between detectors. These numbers contribute to the calculation of the expected signal rates and uncertainties between detectors. Additionally, the independent calculation of the expected reactor antineutrino flux and spectrum presented in Chapter 4 illustrates the method used to determine the relative spectrum uncertainties in the oscillation analysis. This calculation also provides a nominal prediction of the measured data and a set of covariance matrices used to quantify the disagreement between the measured and predicted spectra. Information that is not original to this work is cited to the publication in which it is described or to the internal report from which it is taken if an external publication is not yet available.

1.2 Neutrinos in the Standard Model

The Standard Model of Particle physics is a relativistic quantum field theory that was largely developed in the 1960s by Glashow[13], Weinberg[14], and Salam[15]. It successfully explains

nearly all observed phenomena in particle physics and incorporates all of the fundamental forces except gravity.

Fundamental particles of the Standard model are divided into spin-0 bosons and spin-1/2 fermions. The fundamental bosons are the force carriers for the Strong (g), Electromagnetic (γ), and Weak (W^\pm and Z^0) Forces. The fundamental fermions are divided into leptons and quarks. There are three generations of quarks, each with two particles of differing electric charge. The up, charm, and top quarks have electric charge $+2/3$. The down, strange, and bottom quarks have electric charge $-1/3$. Quarks are the constituent particles of mesons (containing two quarks) and hadrons (containing three quarks). There are also three generations of leptons, each containing one massive, electrically charged particle (e^- , μ^- , and τ^-) and one massless, electrically neutral particle (ν_e , ν_μ , and ν_τ). We now know that the neutrinos are not massless, but they are at least six orders of magnitude smaller than the charged leptons. The exact nature of their mass is an area of active research.

1.3 Electroweak Interactions

As neutrinos lack electric or color charge, they interact only via the Weak Force. There are two types of weak interactions: charged current (CC), moderated by the W^\pm bosons ($m = 80.385 \pm 0.015$ GeV[16]), and neutral current (NC), moderated by the Z^0 boson ($m = 91.1876 \pm 0.0021$ GeV[16]). The CC beta decay interaction is particularly relevant to the Daya Bay Reactor Antineutrino Experiment and discussed below.

1.3.1 β Decay and the Creation of Reactor Antineutrinos

In a fission reactor, nuclear binding energy is released when relatively heavy nuclei split into, usually two, smaller nuclei. Typical energy released per fission is around 200 MeV. Roughly 90% of the energy goes into the kinetic energy of the fission products, with the remaining energy released later in decays of the initial fission daughters. Because nuclei with higher proton number,

Z, require proportionally more neutrons to counteract the Coulomb repulsion between positively-charged protons than nuclei with smaller Z, when an atom fissions the daughters will have a neutron excess.

Nuclei with unequal numbers of protons and neutrons are generally unstable and decay, converting a nucleon of the over-abundant type into the other. Conservation of charge dictates that an additional charged particle be created in these interactions. Historically this particle was called a β^\pm , which we now know is an electron or positron. Conservation of energy, angular momentum, and lepton flavor requires that neutrinos participate as well. In nuclei with excess neutrons, β^- decay can occur, transforming one of the neutrons into a proton: $n \rightarrow p + e^- + \bar{\nu}_e$. In nuclei with excess protons, β^+ decay or electron capture (EC) can occur, transforming one of the protons into a neutron: $p \rightarrow n + e^+ + \nu_e$ or $p + e^- \rightarrow n + \nu_e$. All of these processes conserve the total mass number, A, of the involved nucleus, but Z will change by one.

The generic theory of beta decay was proposed by Fermi in 1934[2, 3] and largely incorporated into Standard Model weak interactions. Fermi's original theory was expanded to incorporate spins of the beta and neutrino by Gamow and Teller[17]. The energy available in beta decay, the Q value, is defined by the difference between the total energies of the initial and final atoms:

$$\begin{aligned} Q_{\beta^-} &= [M_{Z,A}c^2 - Zm_e c^2 + \sum_{i=1}^Z B_i] \\ &\quad - [M_{Z+1,A}c^2 - (Z+1)m_e c^2 + \sum_{i=1}^{Z+1} B_i] - m_e c^2 \\ &\approx (M_{Z,A} - M_{Z+1})c^2 \end{aligned} \quad (1.1)$$

where the electron mass and binding energy differences are neglected in approximation because they are small compared to the nuclear binding energies. The total energy is shared between the outgoing electron and antineutrino.

From Fermi's Golden Rule, we can write the transition rate for beta decay as:

$$\lambda = \frac{2\pi}{\hbar} |M_{fi}|^2 \times \rho(E_f) \quad (1.2)$$

where M_{fi} is the transition amplitude and ρ_f is the phase space for the final state. Following the notation of [18], the transition amplitude is written: $|M_{if}|^2 = \int \psi_f^* V \psi_i d^3r$. The final state wavefunction is given by the combination of wavefunctions for the nucleus, electron, and neutrino

$\psi_{Z+1,A}\psi_{e^-}\psi_{\bar{\nu}}$. Solutions for the electron and neutrino wavefunctions can be written as:

$$\begin{aligned}\psi_{e^-} &\propto e^{i\mathbf{p}_e \cdot \mathbf{r}/\hbar}, \\ \psi_{\bar{\nu}} &\propto e^{i\mathbf{p}_\nu \cdot \mathbf{r}/\hbar}\end{aligned}\tag{1.3}$$

which can be expanded to:

$$\psi_{e^-}\psi_{\bar{\nu}} \propto 1 + \frac{i(\mathbf{p}_e + \mathbf{p}_\nu) \cdot \mathbf{r}}{\hbar} + \dots\tag{1.4}$$

The first term, 1, gives the ‘‘allowed’’ decays. In these cases, the combined beta and neutrino orbital momentum, l , is 0. In some cases, the matrix element of the momentum-independent term vanishes and the higher-order terms need to be considered. The higher order decays are called ‘‘forbidden’’ decays and classified based on the first term in the series to contribute to the transition amplitude. For example, the first momentum-dependent term gives the first forbidden decays, which have $l = 1$. The difference in spin (total angular momentum) between the initial and final nucleus in beta decay is $I_i - I_f = l + s$ where s is 0 (1) if the beta and neutrino spins are opposite (equal). The $s = 1$ case corresponds to the Gamow-Teller transitions.

The shape of an allowed beta spectrum has the basic form:

$$N_\beta(E) = Kp^2(E - E_0)^2F(Z, E)\tag{1.5}$$

where K is a normalization constant, $p^2(E - E_0)^2$ is a phase space factor and $F(Z, E)$ is the Fermi function [19]. Nominally, the Fermi function assumes a point nucleus. Corrections are generally applied for the size of the nucleus[20], radiation of photons by the electron or nucleus[21], screening of the nuclear charge by atomic electrons[22], and induced currents (weak magnetism)[23].

1.4 Oscillating neutrinos

Neutrino oscillation is a quantum interference phenomenon that was originally described by Pontecorvo[24], Maki, Nagasaka, and Sakata[25] in the 1960s. It occurs because the neutrino mass states (ν_1 , ν_2 , and ν_3) are rotated with respect to the neutrino flavor states (ν_e , ν_μ , and ν_τ). Neutrinos are produced in charged current weak interactions with a flavor corresponding to that of the involved charged lepton. Each flavor of neutrino is a linear combination of mass states. As

a neutrino propagates through space, the wavefunctions for each mass component will evolve at differing rates. The resulting phase difference leads to a probability that the neutrino will later interact as a different flavor. The matrix representing the combination of mass states in each flavor states is referred to a U_{PMNS} :

$$U_{PMNS} = \begin{pmatrix} 1 & 0 & 0 \\ 0 & \cos_{23} & \sin_{23} \\ 0 & -\sin_{23} & \cos_{23} \end{pmatrix} \begin{pmatrix} \cos_{13} & 0 & \sin_{13} e^{-i\delta} \\ 0 & 1 & 0 \\ -\sin_{13} e^{i\delta} & 0 & \cos_{13} \end{pmatrix} \begin{pmatrix} \cos_{12} & \sin_{12} & 0 \\ -\sin_{12} & \cos_{12} & 0 \\ 0 & 0 & 1 \end{pmatrix}$$

The three mixing angles, θ_{12} , θ_{23} , and θ_{13} , relate the three mass states to the three flavor states. An additional parameter, δ , gives the Dirac CP violating phase. If $\delta \neq (0, \pi)$ it would imply that charge and parity are not conserved in the neutrino sector. There are two additional Majorana CP phases, which are not shown here because they do not effect oscillation probabilities. If the three observed neutrinos are the only ones, U_{PMNS} would be unitary.

In a two-neutrino case, which approximately describes several experimental situations, the rotation between flavor and mass states reduces to:

$$\begin{pmatrix} \nu_1 \\ \nu_2 \end{pmatrix} = \begin{pmatrix} \cos \theta & \sin \theta \\ -\sin \theta & \cos \theta \end{pmatrix} \begin{pmatrix} \nu_\alpha \\ \nu_\beta \end{pmatrix} \quad (1.6)$$

We can write the time evolution of a neutrino created in the flavor state α as

$$|\nu_\alpha(t)\rangle = e^{-iE_1 t} \cos \theta |\nu_1\rangle - e^{-iE_2 t} \sin \theta |\nu_2\rangle,$$

where $E_i = \sqrt{p^2 + m_i^2}$ ($\hbar = c = 1$). The survival probability is the probability that the neutrino will interact with its initial flavor. Converting time to distance, L , this is given by,

$$P_{\nu_\alpha \rightarrow \nu_\alpha} = |\langle \nu_\alpha | \nu_\alpha(t) \rangle|^2 = 1 - \sin^2 2\theta \sin^2 \frac{\Delta m_{21}^2 L}{4E}. \quad (1.7)$$

The mixing angle in the first sine governs the maximum probability of neutrino disappearance. The difference in the squared neutrino masses, $\Delta m_{21}^2 = m_2^2 - m_1^2$, determines the characteristic frequency of the oscillation. When designing experiments to study oscillation, if the mass-splitting is known the energy and distance can be chosen such that the argument of the second sine in Eq. 1.7

term is $\pi(n + 1/2)$ to maximize the possible deficit in signal. If Δm^2 is unknown, experimental sensitivity will cover a range of $\Delta m^2 - \sin^2 2\theta$ space that depends on the energy of the neutrinos and the distance at which they are observed. For example, reactor-based oscillation experiments measure neutrinos with energies between approximately 1.8 and 10 MeV. An experiment placed around 100 km from the reactor will be sensitive to oscillation due to a mass-splitting of order 10^{-5}eV^2 . An experiment placed around 1 km from the reactor will be sensitive to oscillation due to a mass-splitting of order 10^{-3}eV^2 . In the three neutrino case, there are three different mass splittings: Δm_{21}^2 , Δm_{31}^2 and Δm_{32}^2 . $\Delta m_{31}^2 = \Delta m_{21}^2 \pm \Delta m_{32}^2$ implies that a two-neutrino splitting is a reasonable approximation if there is a large difference between Δm_{21}^2 and Δm_{32}^2 .

1.4.1 Matter Effects and Resonance Oscillations

Matter contains electrons orbiting its constituent nuclei, but muons and taus are less ubiquitous in nature. This leads to differences in how ν_e s interact matter compared to ν_μ s or ν_τ s. The effect of matter on neutrino oscillations was explained in 1978 by Wolfenstein[26]. Coherent forward scattering in matter changes the Hamiltonian governing neutrino propagation leading to a modification of the effective mixing angles.

$$H_{matter} = H_0 + \sqrt{2}G_F n_{e^-} \quad (1.8)$$

Over long distances or under specific density conditions, matter effects become important. In 1985, Mikheev and Smirnov showed that there could be resonant conversion of neutrinos from the Sun due to their transition for a region of high density to the near-vacuum of the solar system[27]. This resonance is called the MSW effect after the authors who explained it.

1.5 Experimental Mysteries in the Detection of Neutrinos

1.5.1 The Solar Anomaly

While the low interaction cross-sections for neutrinos make them difficult to detect, they also make them attractive as an indicator of processes occurring large distances away. John Bahcall and

Ray Davis realized that with a large enough detector, neutrinos could be measured and used to understand the rates of nuclear processes occurring in the Sun. Davis built a large detector filled with Chlorine in the Homestake mine in Lead, SD and looked for evidence of neutrino interactions leaving Argon atoms in the liquid[6, 7]. The rate of neutrino collection was only around 30% of the expected neutrino flux based on standard solar models at the time[28, 29]. This led to controversy over whether the complicated chemistry Davis relied on to extract small numbers of Argon atoms from the detector or the solar model itself was incorrect. Subsequent experiments were done using different detection methods, all of which confirmed that the number of electron neutrinos from the Sun was a fraction of the predicted number.

Ultimately, the SNO experiment[30] analyzed the total flux of neutrinos from the Sun with sensitivity to all flavors. They found that NC interactions, involving all flavors of neutrinos occur at the rate expected by solar models[10]. Meanwhile, CC interactions, involving only the electron flavored neutrinos occurred at a fraction of the rate expected by solar models. This provided conclusive evidence that matter effects in the Sun had caused a resonant conversion[27, 26].

1.5.2 The Atmospheric Anomaly

Neutrinos coming from cosmic-ray interactions in the atmosphere were first detected in 1965 by Reines and others[31, 32]. Further studies were motivated by their role as a background in searches for proton decay[33]. Experiments found, with varying degrees of statistical certainty, the detected number of muon-neutrino events was lower than predicted and comprised a smaller fraction of the atmospheric neutrino flux than expected[34, 8, 35].

It became clear that oscillation played a role in explaining the atmospheric neutrino discrepancies in 1998, when the Super Kamiokande experiment showed that there was a distance- and energy-dependence to the ν_μ/ν_e ratio. The result, taken from [9] is shown in Figure 1.1.

1.6 Unknown Neutrino Properties

In addition to the known neutrino properties, there are several issues that remain unknown or ambiguous.

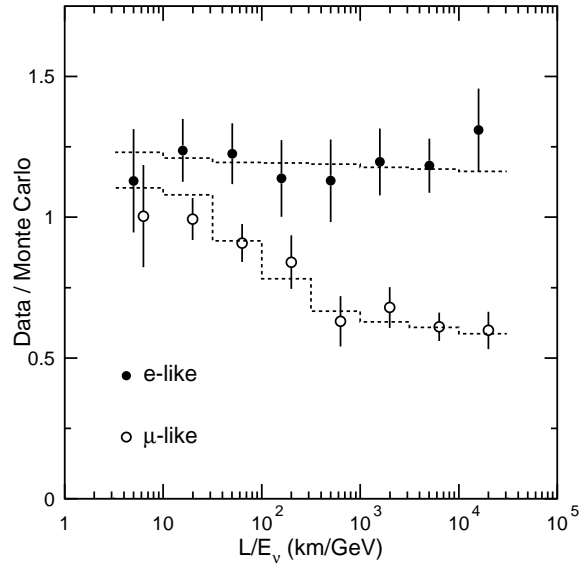


Figure 1.1 The ratio of measured to expected ν_e and ν_μ type events as a function of L/E. Reproduced from [9].

1.6.0.1 CP violation

Given that there are three non-zero mixing angles it is possible that neutrinos violate charge-parity (CP) conservation. In this case, neutrinos would interact differently than antineutrinos. One of the ultimate goals of current neutrino oscillation experiments is to enable measurement of the Dirac CP phase, δ_{CP} . If δ_{CP} is not 0 or π , it is possible that neutrinos could play a role in explaining the baryon asymmetry of the observed universe.

1.6.0.2 Mass hierarchy

Of the three neutrino mass states, we know from solar neutrino experiments that $m_{\nu_1} < m_{\nu_2}$. The absolute value of the mass-squared difference between ν_3 and the others is measured by atmospheric, reactor, and most precisely by accelerator experiments. However, experiments have not yet determined whether ν_3 is the heaviest or lightest of the massive neutrinos. In the “normal” hierarchy, $m_{\nu_3} > m_{\nu_{1,2}}$ and $\Delta m_{31}^2 > 0$; in the “inverted” hierarchy, $m_{\nu_3} < m_{\nu_{1,2}}$ and $\Delta m_{31}^2 < 0$. For experiments studying oscillation by measuring survival of a single neutrino flavor, the disappearance probability (Eq. 1.7) is insensitive to the sign of the mass-splitting. However, in searches for the appearance of a some new flavor, the oscillation probability is not even with respect to the mass-splitting. This leads to degeneracy between the mass-hierarchy and values of other oscillation parameters in accelerator-based experiments searching for possible CP violation in the neutrino sector.

1.6.0.3 Absolute masses

Oscillation requires mass differences between neutrinos, but provides minimal constraint on what the actual masses might be. Experiments looking for neutrino mass study the masses of neutrino flavor eigenstates.

The electron neutrino mass limits are determined by looking at distortions near the end point energies of beta decay spectra. Typically, tritium is used for this purpose. The current upper limit on m_{ν_e} is 2.3 eV (95% C.L.) set by the Mainz experiment in 2004[36]. KATRIN[37] will attempt to measure m_{ν_e} with a factor of 10 improvement in sensitivity in the near future[38].

The muon neutrino mass limits are obtained from kinematic studies of pion decays: $\pi \rightarrow \mu^+ \nu_\mu$. The current limit is 0.170 MeV (90% C.L.) at the Paul Scherrer Institute in the mid-1990s[39].

The tau neutrino mass limits are obtained from kinematic studies of tau decays. The current limit is 18.2 MeV (95% C.L.), set by the ALEPH collaboration[40].

1.6.0.4 Majorana particles

The nature of the neutrino masses is also unknown. Neutrinos may be their own antiparticles, in which case they would have non-zero Majorana masses. The experimental signature of Majorana neutrinos is neutrinoless double- β decay, $0\nu\beta\beta$. In contrast to normal double- β decay, which produces two neutrinos, in the $0\nu\beta\beta$ case the neutrinos will annihilate. This will give a small peak in the total beta energy at the Q-value of the decay's spectrum.

Searches for $0\nu\beta\beta$ allow limits to be placed on the Majorana masses of neutrinos, within limits on our knowledge of the nuclear matrix elements. The double- β interaction can be observed in several nuclei where single β decay is kinematically forbidden. Several experiments have looked for this signal in ^{76}Ge . The Heidelberg-Moscow experiment set a limit $T_{1/2} > 1.9 \times 10^{25}$ years at 90% C.L. A subset of the experiment claimed observation of a $0\nu\beta\beta$ signal corresponding to $T_{1/2} = 1.19_{-0.23}^{+0.37} \times 10^{25}$ years[41], however, this has not been independently supported. For example, the GERDA experiment has obtained a limit, $T_{1/2} > 3.0 \times 10^{25}$ years at 90% C.L[42], disfavoring the claim of [41].

Additional current or near-future experiments looking at ^{136}Xe (EXO-200[43] and KamLAND-Zen[44]), ^{130}Te (CUORE), ^{76}Ge (GERDA and MAJORANA), ^{82}Se (SuperNEMO[45]) will improve half-life sensitivity by around an order of magnitude reducing Majorana mass limits to approximately $\langle m_{\beta\beta} \rangle < 0.1$ eV.

1.6.1 Number of Neutrinos

The standard model includes three neutrino flavors, all of which have been observed experimentally. Additionally, collider experiments indicate the existence of three ($N_\nu = 2.9840 \pm 0.0082$) weakly-interacting neutrinos based on the width of the Z resonance[46]. However, there have been

anomalous experimental results[47, 48] that suggest the possibility of additional neutrinos. Sterile neutrinos could participate in oscillation, but because they would have no NC or CC interactions their experimental signature would look like neutrino disappearance.

The LSND collaboration reported evidence for $\bar{\nu}_e$ appearance in a $\bar{\nu}_\mu$ beam at Los Alamos. They interpreted their result as an oscillation with Δm^2 between 0.2 and 10 eV²[47]. More recently, MiniBOONE has tested the LSND result and found a 2.8σ excess of $\bar{\nu}_e$ events in their $\bar{\nu}_\mu$ beam[48], which is not inconsistent with the LSND result. Additionally, recent re-evaluation of the expected reactor antineutrino flux have led to the suggestion that there may be an additional neutrino mass-splitting in the 0.1-1 MeV range[49]. These are not consistent with the well-established atmospheric and solar mass-splittings, leading to the suggestion that there may be additional massive neutrinos.

Chapter 2

Experimental Landscape of Massive Neutrinos

At the time that the current generation of reactor and accelerator neutrino experiments were proposed, the oscillatory nature of neutrinos was already well established[9, 10]. Furthermore, the field had entered a precision era in which experiments aim primarily to solidify the specific mixing parameter values. The Daya Bay, Double Chooz, and RENO experiments were proposed in the mid-2000's for the purpose of measuring the smallest of the mixing angles, θ_{13} , using reactor-produced antineutrinos. These intended to measure this angle, or improve previous limits on its value by an order of magnitude. Failure to measure the angle would have implications for the next generation of accelerator-based experiments which hope to observe CP violation among neutrinos. This chapter provides context for the current issues in the field pertaining to Daya Bay and related current experiments.

2.1 The Quest For $\sin^2 2\theta_{13}$

Ultimately, physicists would like to know whether neutrinos might play a role in explaining the matter-antimatter asymmetry in the universe. This requires looking for differences in the probabilities $\nu_\alpha \rightarrow \nu_\beta$ and $\bar{\nu}_\alpha \rightarrow \bar{\nu}_\beta$. Practically, this would be most simply done by looking for ν_e or $\bar{\nu}_e$ in a ν_μ or $\bar{\nu}_\mu$ beam, respectively, and mapping differences to allowed values of the CP-violation parameter δ_{CP} . A complication arises because the probability formula governing this transition also depends on the (currently unknown) mass hierarchy and $\sin^2 2\theta_{13}$, leading to degeneracies in much of the possible parameter space. Precise knowledge of a non-zero value of $\sin^2 2\theta_{13}$ is important for reducing this degeneracy or looking for alternative experimental paths to δ_{CP} .

To this end, a generation of experiments was planned with the goal of making a clean measurement of $\sin^2 2\theta_{13}$ at nuclear reactors. The Daya Bay, Double Chooz, and RENO experiment designs were optimized based on knowledge of the atmospheric mass splitting to place detectors at a distance of around 2 km from the reactors to maximize the deficit of neutrinos in the inverse β decay range. Additionally, they were all designed to employ “identical” detectors deployed in a near/far configuration. The near detectors provide a measurement of the reactor antineutrino flux and spectrum close to the cores where the survival probability is high. Then the flux and spectrum measured at the far detectors, where the survival probability is reduced, are compared to the near measurements. This increases sensitivity to a $\sin^2 2\theta_{13}$ -driven deficit by reducing the impact of uncertainties from both reactor antineutrino creation and antineutrino detection.

2.1.1 CHOOZ

Prior to measurements at Double Chooz, Daya Bay, and RENO, the CHOOZ experiment held the upper limit on oscillations due to θ_{13} . The CHOOZ experiment[50] employed a single three-zone detector, installed in an underground hall approximately 1 km from the Chooz B Nuclear Power Station. The power plant has two 4.2 GW_{th} pressurized water reactor cores. The detector’s target region was contained within a Plexiglas geode and filled with 5 tons of 0.09% Gd-doped scintillator. The gamma catcher region contained PMTs and undoped scintillator. The outermost region was optically separated from the inner regions and served as a muon veto. It was also filled with undoped scintillator and held additional PMTs.

CHOOZ collected data between April of 1997 and July of 1998. Their first results were published in 1998[50] and found no evidence for oscillation. Improved results reaching a similar conclusion were published the following year[51]. Maximal electron neutrino disappearance was ruled out at 90% C.L. for $\Delta m^2 > 7 \times 10^{-4} \text{ eV}^2$ and for large Δm^2 a limit was set $\sin^2 2\theta < 0.10$

CHOOZ’s data-taking ceased because of an extended reactor shutdown and scintillator degradation. The ultimate limit obtained on $\sin^2 2\theta_{13}$ was 0.15 at 90% C.L.[52]. The neutrino signal rate over the life of the experiment was $2.58 \pm 0.07 \text{ day}^{-1}\text{GW}^{-1}$ [52]. The uncertainty on CHOOZ’s

Parameter	Relative error (%)
Reaction cross-section	1.9
Number of protons	0.8
Detection efficiency	1.5
Reactor power	0.7
Energy released/fission	0.6
Combined	2.7

Table 2.1 CHOOZ systematic uncertainties, from[52].

determination of the absolute normalization is reproduced in Table 2.1. The combined uncertainty of 2.7% represents the limits of single-detector experiments in measuring the small mixing angle.

2.1.2 MINOS

In 2010, the MINOS Experiment released a result for the $\sin^2 2\theta_{13}$ limit determined from the ν_μ to ν_e appearance channel. They found a 0.7σ excess as compared to expected backgrounds and assigned a limit to the quantity $2 \sin^2 2\theta_{13} \sin^2 \theta_{23} < 0.12(0.20)$ at 90% C.L. for the normal (inverted) mass hierarchy[53]. Because the oscillation probability in accelerator experiments depends on $\sin^2 2\theta_{13}$, the mass hierarchy, and the value of δ_{CP} , this is a somewhat more ambiguous limit than that set by CHOOZ.

Improvements on this result were subsequently published in [54] and [55]. The best-fit obtained was $2 \sin^2 2\theta_{13} \sin^2 \theta_{23} = 0.051^{+0.038}_{-0.030}(0.093^{+0.054}_{-0.049})$ for the normal (inverted) mass hierarchy.

2.1.3 T2K

T2K[56], like MINOS, is an accelerator experiment that looks for ν_e appearance in a ν_μ beam. In 2011, they released results with a positive signal of six ν_e . This excluded a zero value of $\sin^2 2\theta_{13}$ at 2.5σ . For maximal atmospheric mixing and $\delta_{CP} = 0$, their best-fit was $\sin^2 2\theta_{13} = 0.11(0.14)$ for the normal (inverted) mass hierarchy[57].

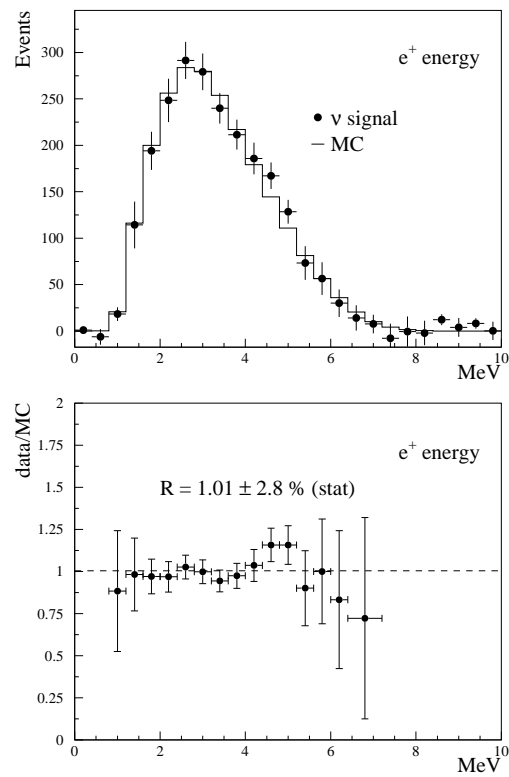


Figure 2.1 Measured positron spectrum from CHOOZ and expected spectrum with no oscillation after background subtraction (top) and the ratio of measurement to expectation (bottom). All errors are statistical. Reproduced from [52].

T2K has subsequently released improved results[58]. With 11 ν_e signal events they obtained a best-fit value $\sin^2 2\theta_{13} = 0.088_{-0.039}^{+0.049}$ for the normal mass hierarchy, maximal atmospheric mixing and $\delta_{CP} = 0$.

2.1.4 Double Chooz

The Double Chooz Experiment was conceived as an improvement on CHOOZ[59]. It operates at the same power plant as the original CHOOZ and the original experimental hall houses the far detector. In the full experiment design, a near detector is employed to provide normalization of the un-oscillated reactor flux. Double Chooz's scintillator was reformulated to avoid the degradation observed by CHOOZ.

Early oscillation results from Double Chooz were published in 2011 and 2012 based on analysis of the measured far-site event rate[60] and the combination of event rate and spectral shape[61]. Results were $\sin^2 2\theta_{13} = 0.086 \pm 0.041 \pm 0.030$ and $\sin^2 2\theta_{13} = 0.109 \pm 0.030 \pm 0.025$ where 1σ errors are given for statistics and systematics, respectively. In order to reduce reactor-based systematic uncertainties in a single-detector measurement, the predicted inverse beta decay cross section (rate) was calculated based on the flux measured by the Bugey4 experiment[62]. With corrections for the fuel composition differences between the Bugey and Chooz reactor cores, this reduces the reactor flux uncertainty to roughly the 1.4% determined by Bugey4. This uncertainty is larger than can be obtained from a relative near/far measurement.

2.1.5 RENO

Similar to other reactor oscillation experiments of the current generation, RENO's design places detectors at varying distances from the cores of a large nuclear power complex[63]. The Yonggwang Nuclear Power Plant in South Korea has six 2.66-2.8 GW_{th} reactor cores. RENO's two, identical, detectors are placed in water pools at two halls approximately 300 m and 1400 m from the reactor center. Each detector has three concentric cylindrical zones: a 16-ton liquid scintillator target (0.1% Gd-doped), a liquid scintillator gamma catcher region (undoped), and a non-scintillating buffer region (mineral oil). The buffer region is instrumented with 354 PMTs.

The detectors are each placed inside a large water pool providing a 1.5 m buffer from radiation in the surrounding rock. RENO produced an initial rate based result in 2012, measuring $\sin^2 2\theta_{13} = 0.113 \pm 0.013 \pm 0.019$ [64].

2.1.6 Daya Bay

The Daya Bay Experiment is discussed in greater detail in the following chapters, but described in comparison to the competing reactor experiments here. It was designed[65] towards the same purpose as the Double Chooz and RENO experiments, but differs from each in a number of ways. The site consists of six 2.9 GW_{th} cores at the Guangdong and Ling Ao power plants approximately 55 km northeast of Shenzhen in Southern China. Unlike Double Chooz and RENO, there are two near sites. One provides normalization information for the Guangdong (D1 and D2) reactors and the other provides normalization information for the Ling Ao (L1, L2, L3, and L4) reactors. Like RENO, but in contrast to Double Chooz, initial results were produced based on a near/far rate ratio with multiple detectors deployed.

The detectors themselves are also similar to those employed by RENO and Double Chooz, but with key differences. Daya Bay's antineutrino detectors (ADs) have a nominal target mass of 20 tons, making them the largest of this generation. They each have 192 PMTs around the periphery of the buffer region. To increase effective photocathode coverage, specular reflectors are installed above and below the gamma catcher region. Additionally, there are eight detectors in the full design (six installed for current analyses) unlike two for RENO (both installed for initial analysis) and Double Chooz (one used for initial analyses). Between the increased total target mass and higher reactor power, Daya Bay has the highest statistical accuracy of the three.

Daya Bay began taking physics data on September 23, 2011. The earliest physics run included the first pair of detectors installed in the Daya Bay near hall. Three months of data were collected with the purpose of quantifying the relative performance of ADs exposed to the same neutrino flux. Initial results established a relative energy scale uncertainty of 0.4%, a relative neutron energy selection efficiency of 0.11%, and an overall relative detection efficiency of 0.11%[66]. It also

obtained the ratio of signal IBD events observed in AD1 to AD2 as $0.978 \pm 0.008(\text{stat}) \pm 0.003(\text{sys})$, in agreement with the expected ratio of 0.981.

During the initial three month period, four additional detectors were installed and commissioned at the Ling Ao Near Hall (one AD) and the Far Hall (three ADs). Six-detector data collection began on December 24, 2011. Using the first 55 days of data, Daya Bay's first, rate-based, oscillation result was published in early 2012. The mixing parameter result was $\sin^2 2\theta_{13} = 0.092 \pm 0.016(\text{stat}) \pm 0.005(\text{sys})$ and reached 5.2σ when ruling out $\sin^2 2\theta_{13} = 0$ [67]. An improvement to this analysis, based on a larger data sample was published in 2013[68]. The second results found $\sin^2 2\theta_{13} = 0.089 \pm 0.010(\text{stat}) \pm 0.005(\text{sys})$.

Oscillation results for the full six-AD run are under review as of this writing[69]. They include all six-AD data up to July 28, 2011. Measurements of $\sin^2 2\theta_{13}$ were made including rate-only, rate+spectral shape information, and shape information only. The work presented in this thesis corresponds to this data set.

2.2 Revisiting the Reactor Antineutrino Flux and Spectrum

Current knowledge of the rate and energy spectrum of reactor-produced antineutrinos comes largely from two neutrino experiments conducted at the Bugey power plant and a series of β spectrum measurements conducted with the BILL high-precision spectrometer at ILL in the 1980s. In the ILL measurements, foils of ^{235}U , ^{239}Pu , and ^{241}Pu were irradiated with thermal neutrons and the resulting beta spectra were measured[70, 71, 72, 73]. A conversion procedure is used to map these spectra into the corresponding $\bar{\nu}_e$ spectra. The conversion process involves fitting a number of "virtual" β branches to the observed spectrum and then applying corrections to account for positron-neutrino mass difference, and Coulomb potential difference.

2.2.1 Bugey 4

The Bugey 4 experiment collected approximately 300,000 neutrino events at the Bugey power plant over 88.47 days in the mid 1990s[62]. Their detector was installed 15 meters from the Bugey 5 core in a laboratory with 25 m.w.e. It was a neutron detector consisting of a roughly 2 m^3 tank

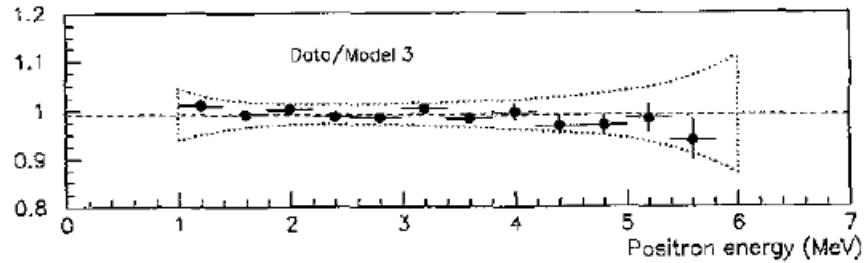


Figure 2.2 The comparison of Bugey-3's positron spectrum with the expectation based on the converted ILL β spectra. Errorbars are statistical and the errorband includes the quoted ILL uncertainties and a 0.8% energy scale uncertainty. Reproduced from [77].

of distilled water instrumented with a matrix of 252 ^3He counters. The neutrons from inverse beta decay events were detected when they captured on the ^3He nuclei.

Bugey 4 measured the total IBD cross section as $\sigma_f = 5.750 \times 10^{-43} \text{ cm}^2/\text{fission} \pm 1.4\%$ for isotopic fission fractions 0.538:0.078:0.328:0.056 for ^{235}U : ^{238}U : ^{239}Pu : ^{241}Pu [62]. To date, this is the most precise measurement of the integral inverse beta decay cross section.

2.2.2 Bugey-3

In 1996, Bugey-3 experiment[74] compared measurements of the reactor neutrino spectrum at 15 and 40 m baselines to three different models of the flux. Their experiment consisted of three 600 liter ^6Li -doped liquid scintillator[75] detectors are described in detail in [76].

With 120,000 events, they concluded that of the models considered at that time, the one comprising Schreckenbach et al.'s beta spectra measurements and Klapdor and Metzinger's U-238 calculation most closely matched the data[77]. Quantitatively, with 12 energy bins between 1 and 6 MeV (positron energy) the data/ILL model ratio fit to a constant gave 0.99 with a χ^2 of 9.23/11. When modifying their energy scale by 0.4% they obtained a χ^2 of 4.3/11. The comparison of the ILL conversion to the spectrum measured by Bugey-3 is reproduced in Figure 2.2.

Since the Bugey-3 result, the converted ILL beta spectra have been used to predict reactor spectra shapes (often combined with the Bugey-4 normalization) for subsequent experiments (CHOOZ

[52], Palo Verde [78, 79], KamLAND [11, 80], Double Chooz [61, 60], RENO [64], Daya Bay [67, 68]).

2.2.3 Recent Developments

In 2011, collaborators on the Double Chooz Experiment, motivated by a desire to reduce the reactor-related uncertainties that would dominate the single-detector phase of their experiment, revisited the calculation of the reactor antineutrino flux and the conversion procedure used to predict event rates at reactor experiments[81]. They found that information in nuclear databases remains insufficient to enable accurate prediction of the antineutrino spectra without also including information from the ILL measurements. However, upon updating several parameters used in the conversion they found an upward shift in the expected normalization. When reinterpreting past measurements in light of the currently expected flux, this leads to an apparent deficit in observed reactor antineutrinos, the reactor “anomaly”[49]. The recalculation of the expected fluxes and spectra was confirmed by Huber[19]. However, it has also been proposed that the anomaly is a result of under-estimation of the reactor flux uncertainties, specifically those related to the assumption that all branches have allowed β spectra shapes in the conversion of the ILL spectra[82].

2.3 Summary

The search for the small mixing angle $\sin^2 2\theta_{13}$ spurred the development of a generation of reactor-based precision oscillation experiments. Motivated by a need to maximize the sensitivity to a potentially small $\sin^2 2\theta_{13}$, indicated by the CHOOZ limit[52], these experiments were designed with multiple detectors to reduce the impact of reactor antineutrino flux uncertainties. This was based on an idea proposed by Mikaelyan and Sinev in 2000[83].

Indications from global analyses of neutrino data, for example [84, 85, 86, 87], began suggesting that $\sin^2 2\theta_{13}$ would be non-zero in 2008 and continuing through initial hints from MINOS, T2K[56], Double Chooz[60], and eventually first conclusive observations by Daya Bay[67], followed by RENO[64].

Despite the relative nature of present-generation $\sin^2 2\theta_{13}$ measurements, interest in the reactor antineutrino flux and spectrum increased when a re-evaluation[81] of the standard method to predict reactor antineutrino fluxes[72, 73, 62] turned up an apparent deficit, the “reactor anomaly”, between measured and predicted reactor fluxes[49]. The prediction method involves measured beta spectra from thermally-fissioning isotopes ^{235}U , ^{239}Pu , and ^{241}Pu into their antineutrino counterparts using around 30 virtual beta branches with allowed shapes and applying corrections for differences between the electron and neutrino interactions with the nucleus. The change in expected normalization noted by [81] was confirmed by [19].

Daya Bay’s design, which includes eight 20-ton detectors placed at one of the world’s largest nuclear power plants, allows it to reach the highest statistical precision of its generation of experiments. This puts it in a position to reassess the agreement of the antineutrino spectrum produced at nuclear power reactors to expectation from either new[19, 81] or old[72, 73, 88] conversion or the ILL β spectra.

Chapter 3

The Daya Bay Reactor Neutrino Experiment

3.1 Motivation

The Daya Bay Reactor Neutrino Experiment was designed to make a precision measurement of the smallest of the neutrino mixing angles, θ_{13} . A non-zero measurement of θ_{13} is a prerequisite to searches for CP violation in the neutrino sector. Knowledge of $\sin^2 2\theta_{13}$ also provides additional constraints to accelerator experiments trying to determine the neutrino mass hierarchy. Nuclear power reactors are convenient sources for this measurement because they produce roughly 10^{20} $\bar{\nu}_e$ /second per gigawatt of thermal power. The neutrinos produced have energies up to around 10 MeV.

Prior to the current generation of reactor-based oscillation experiments, $\sin^2 2\theta_{13}$ was known to be small. The experimental limit was set in the late 1990s by the CHOOZ collaboration [50, 51, 52]. They obtained the limit $\sin^2 2\theta_{13} < 0.1$ at 90% C.L. with data collected between April 1997 and July 1998. Uncertainties in the CHOOZ experiment were at the few percent level (2.7% for flux normalization uncertainty and 1.5% for detection efficiency). In general, reactor neutrino experiments that rely on a single detector are limited by knowledge of the reactor antineutrino spectrum.

Following the CHOOZ experiment, it was suggested that systematic uncertainties could be minimized by employing identical detectors at multiple distances from the reactor [83]. The expected event rate at a particular detector is:

$$N_{IBD} = \frac{N_p}{4\pi L^2} \int \epsilon S_\nu(E) \sigma_{IBD}(E) P(\theta_{13}, L, E) dE \quad (3.1)$$

where N_p is the number of protons, L is the distance between the detector and the source, S_ν is the spectrum of neutrinos produced at the source, σ_{IBD} is the inverse beta decay cross section, and $P(\theta_{13}, L, E)$ is the survival probability. If functionally identical detectors are deployed at multiple distances from the antineutrino source, the correlated uncertainty components in the reactor neutrino flux, cross section, and detection efficiencies will be reduced. In this scheme, sensitivity to $\sin^2 2\theta_{13}$ is reduced to the level of uncorrelated uncertainty between detectors as opposed to the larger, correlated, uncertainties on reactor neutrino production and absolute detection efficiency.

The Daya Bay Reactor Neutrino Experiment was designed to exploit this idea and measure $\sin^2 2\theta_{13}$ or reduce the previous limit to 0.01 using the six-core Guangdong Nuclear Power Generating Station as its neutrino source. Two near halls house detectors within a few hundred meters of the reactor cores to provide information on the normalization of the reactor antineutrino flux. A far hall houses detectors approximately 2 km from the cores to measure a relative deficit exceeding $1/L^2$. Eight, functionally-identical, 20 ton detectors are distributed between the near and far halls. Beyond, measuring the smallest mixing angle, the high (of order 1000 events/day) signal rate at the near halls puts Daya Bay in a position to collect a larger event sample than similar experiments of the previous and current-generations.

3.2 Experimental Site

Daya Bay has been built at the Guangdong Nuclear Power Generating Station in Dapeng, Guangdong, China. The power plant is roughly 55 km northeast of Hong Kong and Shenzhen. The complex as a whole produces 17.9 GW_{th} power at full capacity and consists of six, $2.9 \text{ GW}_{thermal}$, model M310 and CPR 1000 pressurized water reactors. The two oldest cores, referred to as the Guangdong or Daya Bay cores, D1 and D2, were connected to the power grid in 1993 and 1994. The newer four cores at the Ling Ao power plants, L1, L2, L3, and L4, were connected in 2002, 2002, 2010, and 2011 respectively [89].

In addition to the power of the reactors, the Daya Bay site is convenient for a neutrino experiment because there are large hills just inland of the reactor cores. By placing the experimental halls under these hills, detectors have roughly 100 m (300 m) of passive shielding from cosmic rays at

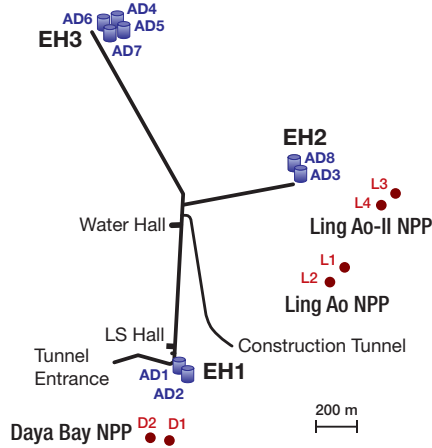


Figure 3.1 Layout of the Daya Bay experimental site. From [90].

the near (far) sites. Table 3.1 lists the overburdens, muon flux, and mean muon energies at each hall. Uncertainties in the antineutrino flux from the reactors would limit Daya Bay's sensitivity to $\sin^2 2\theta_{13}$ in a single-detector or single-site experiment. Having multiple sites at varying distance from the reactor cores enables a partial cancellation of the reactor uncertainties, increasing sensitivity to $\sin^2 2\theta_{13}$. Two halls used to provide flux normalization from the Daya Bay and Ling Ao cores are called Experimental Hall (EH) 1 and EH 2, respectively. The Daya Bay Near Hall (EH 1) is located approximately 360 m from from the two Daya Bay cores. The Ling Ao Near Hall (EH 2) is located approximately 450 m from the four Ling Ao cores. Each near hall is designed to hold two detectors. The far hall (EH 3) is located between 1.5 and 2 km from all cores. The location of EH 3 was chosen to provide sensitivity to an oscillation in the 2 to 10 MeV range driven by the atmospheric mass splitting, as $\Delta m_{31}^2 \approx \Delta m_{32}^2$. The far hall can hold up to four detectors to partially account for the reduction in flux at a distance from the cores. The site layout is shown in Figure 3.1. For the data collected during the period used in this work, physical ADs 1 and 2 were installed in EH 1, AD 3 was installed in EH 2, and ADs 4, 5, and 6 were installed in EH 3. Baselines from each core to each of the first six detectors are listed in Table 3.2. Figure 3.2 shows the proportion of events from each core in each experimental hall.

	Overburden [m.w.e]	R [Hz/m ²]	Mean E _μ [GeV]
EH1	250	1.27	57
EH2	265	0.95	58
EH3	860	0.056	137

Table 3.1 Daya Bay detector overburdens, muon rates, mean muon energy. Numbers from [68]

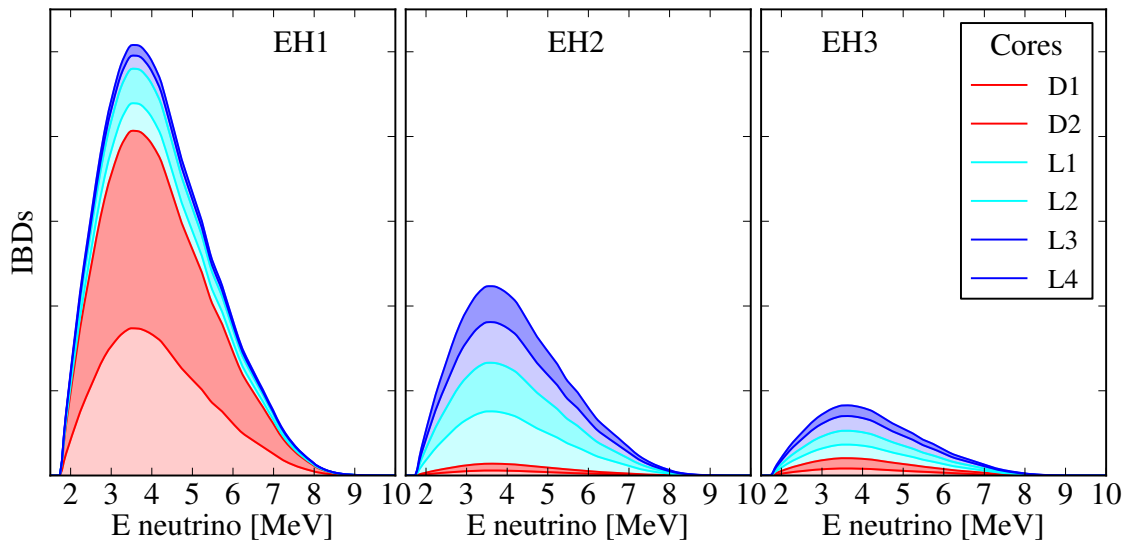


Figure 3.2 Approximate proportions of IBD events during the data period analyzed in this work coming from each of the reactors.

	D1	D2	L1	L2	L3	L4
AD1	362	372	903	817	1354	1265
AD2	358	368	903	817	1354	1266
AD3	1332	1358	468	490	558	499
AD4	1920	1894	1533	1534	1551	1525
AD5	1918	1982	1535	1535	1555	1528
AD6	1925	1900	1539	1539	1556	1530

Table 3.2 Distances (in meters) between reactors and detectors installed during this analysis. From [68].

3.3 Inverse Beta Decay Signal

As is common in reactor-based experiments, antineutrinos are detected indirectly via the inverse beta decay (IBD) interaction, $\bar{\nu} + p \rightarrow n + e^+$. IBD products are detected as a coincident signal. The coincidence assists in reducing single-event backgrounds from naturally occurring radioactive decays and cosmic-ray products. The positron carries away most of the neutrino's energy. It will lose kinetic energy into the scintillator through collisions and bremsstrahlung and then annihilate with an electron (creating two 511 keV gammas) in the signal's prompt component. Meanwhile, the neutron will thermalize and capture on an atom in the detector some time later. De-excitation of the nucleus yields γ s that comprise the signal's delayed component. The specific timing and energy of the delayed signal can be tuned through the choice of capture target and its density in the scintillator. In Daya Bay, the target scintillator is doped to 0.1% by weight with Gadolinium due to Gd's high neutron capture cross-section. Upon capturing a neutron, ^{155}Gd and ^{157}Gd end up in excited states with energies of 8.54 and 7.94 MeV, respectively. This will lead to a delayed signal of roughly 8 MeV occurring approximately 30 μs after the prompt event.

3.3.1 Cross section

Kinematically, the threshold antineutrino energy for the IBD interaction is roughly 1.8 MeV, which is needed to convert a proton into the more massive neutron and produce a positron at rest. The cross section for this process can be calculated analytically and evaluated given the masses of involved particles, antineutrino energy, neutron lifetime, and form factors[91].

The zeroth order total inverse beta decay cross section can be written as

$$\sigma^0 = \frac{2\pi^2/m_e^5}{f^R\tau_n} \times E_e p_e \quad (3.2)$$

where m_e is the positron mass, f^R is the phase space factor, τ_n is the neutron lifetime, E_e is the positron energy, and p_e is the positron momentum. The neutrino energy is related to the positron energy by $E_\nu = E_e + (M_n - M_p)$ and has a kinematic threshold of 1.806 MeV in the lab frame.

The angular dependence of the inverse beta decay cross section σ_{IBD} was calculated to order $1/M$, where M is the average nucleon mass, by Vogel and Beacom [91]. This formula is integrated over all angles for the purpose of predicting the Daya Bay IBD rate and spectrum.

3.3.2 Backgrounds

Backgrounds for the coincident IBD signal are intrinsically lower than one would expect for a single-event signal. Nonetheless, minimizing possible accidental or correlated backgrounds is important to maximizing the sensitivity to $\sin^2 2\theta_{13}$. Two main sources for backgrounds are cosmic muons and radioactive decays in material in and surrounding the ADs. These are reduced by placing detectors underground and by controlling the amounts of radioactive materials in the detectors.

To reduce the cosmic muon fluxes, detectors are installed under the mountains at the Daya Bay site. The experimental halls have between 100 and 300 m of overburden (250-800 m.w.e). The hall overburdens and corresponding muon rates and energies are listed in Table 3.1. In addition to the passive shielding provided by the mountains, the ADs are placed in instrumented water pools. The pools serve as Cherenkov detectors to identify and veto muons passing near the detectors. They also attenuate the spallation products of muons that pass through rock around the pools and the products of natural radioactivity from the rock.

To reduce the background components from radioactive contaminants detector materials are carefully chosen and handled. The detectors are assembled in a large Class 10000 clean room. Liquid nitrogen boil-off gas is used to cover the detector liquids stored underground prior to detector filling, reducing their exposure to Radon. N_2 cover gas is also used to fill spaces in non-liquid volumes of the detector after their installation in the water pools to prevent exposure to Radon.

3.4 Antineutrino Detection

The Daya Bay Experiment antineutrino detectors (ADs) are liquid scintillator detectors optimized for detection of the inverse beta decay interaction $\bar{\nu} + p \rightarrow n + e^+$. ADs are divided into three concentric, roughly cylindrical, regions: the central target region, a gamma catcher region,

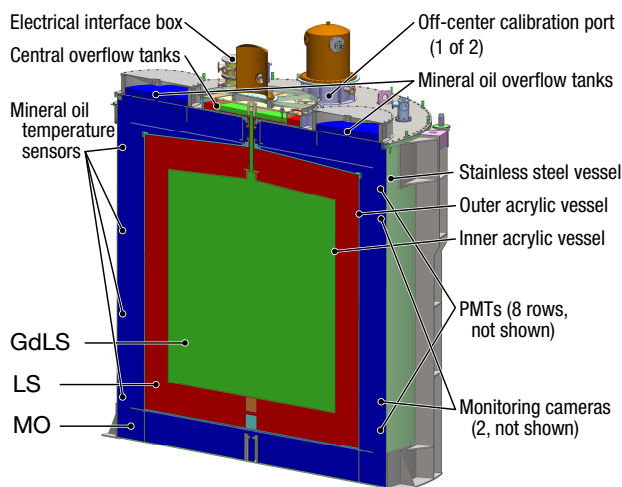


Figure 3.3 Annotated cut-away drawing of an AD. From [90].

and an outer buffer zone. A drawing of a detector is shown in Figure 3.3. The outer-most vessel is a 5-m diameter stainless steel cylinder (SSV). This region contains 192 8" Hamamatsu R5912 photomultiplier tubes (PMTs) their supporting structures, monitoring cameras, and top and bottom reflectors. PMTs are arranged in eight rings around the vessel walls. The SSV is filled with 36 tons of non-scintillating mineral oil. The mineral oil attenuates radiation from PMT glass and SSV welds, preventing it from reaching the inner volumes. A black acrylic absorber surrounds the PMTs to simplify the optical geometry. The top and bottom specular reflectors increase effective photocathode coverage to 12% without requiring PMTs on the top and bottom of the detector. Monitoring cameras mounted on PMT ladders are used to visually inspect the interior of the detector as necessary during filling or operation.

The middle, gamma catcher, region is surrounded by a 4-m diameter acrylic vessel (OAV). The gamma catcher is filled with roughly 22 tons of the liquid scintillator. It provides additional volume for the gammas released upon Gd de-excitation to scatter or pair-produce, depositing energy into the scintillator. The distance of the PMTs to the from the outer edge of the gamma catcher region was determined based on the need to create uniform light yield. Gamma catcher dimensions were chosen to optimize the neutron detection efficiency[65].

The innermost region is contained within a 3-m diameter acrylic vessel (IAV). This is the AD's primary inverse beta decay target region. The IAV is filled with roughly 20 tons of liquid scintillator containing 0.1% Gd (by weight). Having the neutron capture target physically confined in the central region of the detector localizes the IBD signal without requiring a fiducial volume cut.

The three main detector volumes are connected to regions above the main SSV lid. The upper regions hold liquid overflow tanks and calibration sources. Overflow tanks are a buffer against thermal fluctuations and resulting change in detector liquid densities. They hold some extra liquid to keep the main volumes full in the event of thermal contraction and provide space for thermal expansion. The overflow tanks are instrumented to monitor liquid levels, temperatures, and tilts of each tank[90].

Additionally, three automatic calibration units (ACUs), sit across the top of each AD. Sources stored in the ACUs are deployed along three axes into the target and gamma-catcher regions. LED sources are used for PMT gain calibration. 15 Hz ^{68}Ge sources, 0.7 Hz ^{241}Am - ^{13}C neutron sources, and 100 Hz ^{60}Co sources are used to characterize the energy response constant and the spatial non-uniformity of detector energy response. Sources are deployed for weekly calibration runs to monitor the stability of the detector response over time. Details of the ACU systems are given in [92].

3.4.1 Detector Liquids

The scintillator is mainly linear alkyl benzene (LAB). Two fluors, PPO and bis-MSB, are added to shift the emitted wavelengths into the region with highest PMT efficiency. The PPO concentration is 3 g/L and the bis-MSB concentration is 0.015 g/L. In the Gd-doped scintillator, Gd is added to a concentration of 0.1% by weight. The nominal density of the scintillators is 860 g/L. Scintillator requirements and chemistry are described in [93, 94].

Knowledge of the masses of the liquids, particularly in the target region, is important for calculating the absolute expected signal rate of each AD and the relative signal rate between ADs. In the case of the target region, the number of protons (H atoms) is directly proportional to the expected

signal rate. By filling from common liquid sources, the chemical composition of the liquid can be assumed to be identical between detectors. This implies that the relative uncertainties signal rates due to N_p (Eq. 3.1) will be predominantly from the relative mass differences between detectors. One of the main goals of Daya Bay’s filling system is to precisely measure the mass of all three liquids in each detector. When detectors are filled, care is taken to follow consistent calibration and filling procedures thus minimizing the relative and absolute uncertainties on the target mass. Details related to the mass of the liquids and the process used to fill the detectors can be found in Appendix A.

3.4.2 Muon Veto

ADs are installed in PMT-instrumented water pools covered with RPC arrays to assist in identifying and vetoing events caused by muons. The ADs are each surrounded by at least 2.5 m of ultrapure water. Water provides shielding from radiation and spallation neutrons originating in the rock surrounding the detectors. The water pool PMTs allow detection of Cherenkov light emitted when muons pass through the pools. Pools are divided into two optically-separated regions: the inner (IWP) and outer (OWP) water pools.

There are 121 (167) PMTs in the IWP (OWP) in each near hall. There are 160 (224) PMTs in the IWP (OWP) in the larger, far hall. Most water pool PMTs are Hamamatsu R5912 8” PMTs. Additional PMTs are EMI 9350KA and D642KB models originally from the MACRO experiment[95]. For vetoing muons in the neutrino data, the water pool trigger threshold is 12 hit PMTs.

The efficiency of the muon system is evaluated by comparing the water pool trigger and AD muon rates (defined as > 20 MeV of reconstructed AD energy). The efficiency of the IWS is $99.98 \pm 0.01\%$ in all halls. The efficiency of the OWS is hall-dependent: $97.2 \pm 0.2\%$, $97.4 \pm 0.2\%$, and $98.7 \pm 0.2\%$ in EH1, EH2, and EH3, respectively[96].

RPCs The water pools are covered with arrays of 2.17 m \times 2.20 m resistive plate chamber (RPC) modules. Each RPC module has four bare RPC chambers. The near hall pools have 6 \times 9 module

arrays. The far hall pool has a 9×9 module array. Modules are installed to overlap at edges. The RPC array support structure is on rails, enabling it to be easily removed from the pools. The RPCs have 8 cm spatial resolution. Triggers can be adjusted based on the number of hit layers in a module (i.e. 2/4, 3/4, 4/4). There is also a 10 Hz periodic trigger.

Muon rates measured by each detector (IWS, OWS, RPC, AD) in each hall are consistent. Further details of the muon system can be found in [96].

3.5 An Antineutrino Detector Event

The purpose of the ADs is to convert the energy of particles interacting therein into light. Subsequently, the light is collected by PMTs, producing a quantifiable electronic signal. By comparing the electronic signal to that obtained with well-understood calibration sources, the energy of the original particles is inferred. This subsection briefly describes how particle interactions in the detector come to be measured.

The IBD signal comprises interactions of positrons and neutrons in the ADs. Positrons (and similarly electrons), will primarily lose energy to electronic ionization of the scintillator. Radiative losses can also contribute. At a nominal density of 0.86 g/cm^2 , electrons and positrons will lose roughly 1.6 MeV/cm in the scintillator[97]. Ultimately, positrons will annihilate with electrons yielding two 511 keV gammas. Neutrons are detected on the basis of 8 MeV of energy distributed between several gammas that are produced as Gd atoms de-excite following a neutron capture. Gammas do not produce scintillation light directly. However, their energy is transferred to charged particles via photoelectric, scattering, and pair-production interactions. The attenuation length of the positron annihilation gammas in LAB is approximately 12 cm. The attenuation length increases with energy such that for the most energetic IBD-related gammas it will be around 40 cm[98].

The scintillator is responsible for the majority of the light production. A small amount of light produced in the detectors comes from Cherenkov radiation. Scintillator fluorescence is a molecular phenomenon in which molecular electrons and vibration modes are excited by passing radiation[99]. For singlet electronic states, photons are emitted when the first excited state decays

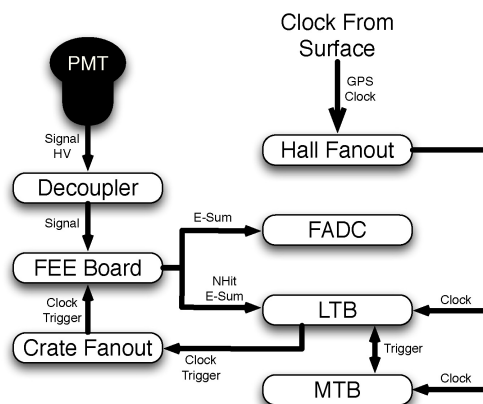


Figure 3.4 Diagram of the electronics. From [66].

to a vibrational mode of the ground state. Higher excited states internally degrade without producing light. Electrons in triplet spin states of the scintillator can become similarly excited, but they do not fluoresce as they de-excite. Instead, they can interact with additional triplet states leaving excited singlet states, which subsequently emit photons. Thus the timing of fluorescence light from scintillators depends on the proportion of singlet versus triplet states excited.

When a photon produced in the detector, generally through scintillation, reaches the photocathode of a PMT, the photocathode may emit a photoelectron (p.e.). The probability of this occurring depends on the wavelength of the photon and the quantum efficiency of the PMT. The Daya Bay scintillator has been designed to produce light with wavelengths matched to the peak sensitivity of the PMTs. Beyond its photocathode, a PMT consists of a series of dynodes and an anode. Electric fields within the PMT are designed to accelerate the photoelectron into the dynodes. At each dynode, more electrons are emitted and upon reaching the anode at the back of the PMT the electrons will produce a change in voltage that is interpreted by the electronics as a signal.

3.5.1 Electronics and Trigger

Daya Bay's electronics and trigger are described in detail [66], some information is reproduced in this section for completeness. A diagram of the electronics is shown in Figure 3.4. Low voltage signals from PMTs are decoupled from the high voltage used to bias PMTs. The low voltage

signal associated with p.e.s are sampled by the front-end electronics (FEE) at 40 MHz. Each FEE board monitors 16 PMTS. They send unshaped ADC pulses and a count of the number of channels with ADC values above threshold to the local trigger board (LTB). The threshold corresponds to approximately 0.25 p.e.

For trigger purposes, the number of channels with ADC over the 0.25 p.e. threshold is referred to as NHit. The integrated ADC pulses give the total charge associated with a channel. The sum of total charge across all channels is referred to as ESum. The local trigger board (LTB) will issue a trigger based on NHit or ESum conditions crossing pre-determined thresholds. Thresholds for physics triggers are $NHit \geq 45$ or $ESum \geq 65$ p.e. (corresponding to approximately 0.4 MeV energy) Physics trigger rates are around 280 Hz. Additionally triggers can be issued by other detector systems (cross-triggers), or periodically (for example, for calibrations). When a trigger is issued the FEE will read out average ADC in a 100 ns window prior to the trigger condition being met as well as the ADC and TDC information for the 1 μ s after the threshold. This information is stored for each detector channel[66].

Calibrations determine the conversion from observed PMT charge, in terms of ADC values, into a number of p.e. and ultimately, into physical energy. Two methods can be used to determine the single p.e. to ADC conversion. First, low intensity LED calibration sources that are deployed weekly for PMT timing calibration can also be used to check the gains. Second, information collected from periodic triggers corresponding to PMT dark noise can be used. PMT dark noise rates are of order 10 kHz and largely composed of single p.e.s. The p.e./ADC conversion can thus be determined over time for individual channels and incorporated into the overall energy reconstruction. Figure 3.5 shows the detector gains as a function of time.

3.5.2 Position and Energy Reconstruction

Energy reconstruction converts from p.e. to observed physical energy. This energy scale is primarily determined using spallation neutrons with ^{60}Co calibration sources serving as a cross-check. An AD will record approximately 165 p.e./MeV, which varies somewhat between ADs and over time. The energy scale of each detector as a function of time is shown in Figure 3.6. There are

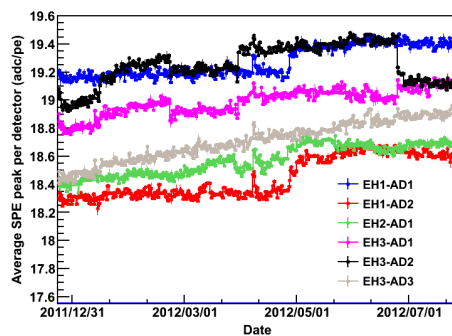


Figure 3.5 The mean single p.e. PMT gain as a function of time. From [100].

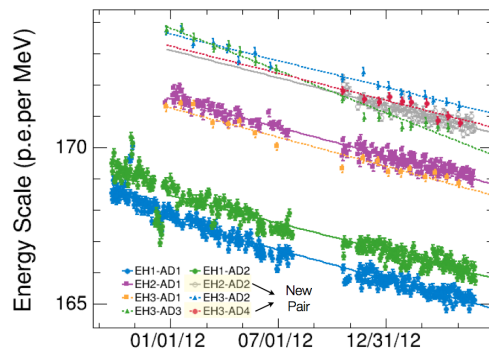


Figure 3.6 The stability of the energy scale in each detector as a function of time. A degradation of slightly more than 1%/year is observed. From [100].

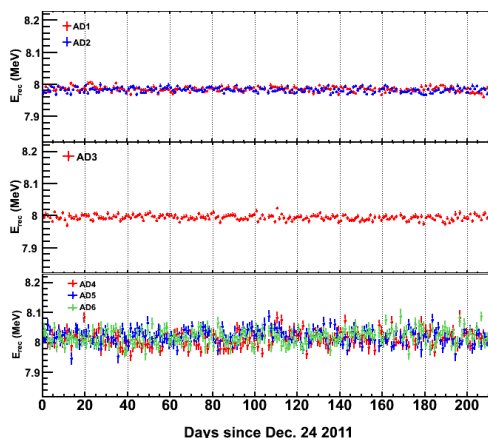


Figure 3.7 The stability of the neutron capture peak on Gd over time in each detector. From [100].

differing methods that can be used to determine the accurate p.e.-to-MeV conversion, incorporating position dependence between detectors. This section summarizes the method of [101].

For each event, observed charge is summed over all PMTs. In order to avoid instrumental biases from PMT effects such as after-pulsing, only initial hits for each PMT are included in the summed charge. Position reconstruction is based on a calculation of each event's center-of-charge (COC). The COC will be biased towards the center of the detector. The bias is evaluated and corrected through MC studies comparing true event position and reconstructed position and checked using calibration sources deployed to known positions in the detector.

Spallation neutrons are used to determine the energy scale for the full detector volume. Neutron captures on Gd give a well-defined signal that will be distributed uniformly in the target region of the AD. Two Gaussians, corresponding to the peaks from n-capture on ^{155}Gd and ^{157}Gd are fit to the spallation data accounting for the differing abundances and excitation energies of each. The peak of the higher-energy Gaussian is pegged to 8 MeV. The position of this peak over time is used to assess the stability of the energy scale of each detector over time. Figure 3.7 shows the reconstructed energy of the neutron capture peak over time in each detector. The relative difference between the neutron capture peaks between detectors is shown in Figure 3.8. This difference is taken as the AD-uncorrelated energy scale uncertainty.

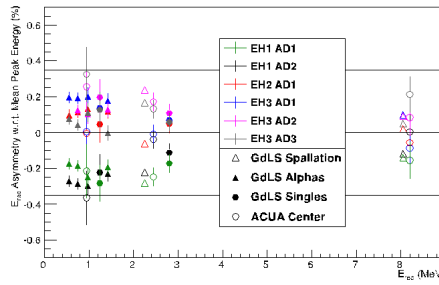


Figure 3.8 The relative Gd neutron capture peak between the detectors. The relative energy scale uncertainty between ADs is taken to be spread of these points, or 0.35%. From [100]

3.6 Signal Rate and Uncertainties

The expected number of inverse beta decay events (Eq. 3.1) depends on the number of target protons, N_p and detection efficiency, ϵ . This section discusses the defines the target protons and corresponding relative uncertainties. Additionally, intrinsic efficiency components, attributable to the probability of neutron capture on Gadolinium are summarized.

3.6.1 Target Protons

The number of target protons, N_p , is directly proportional to the expected number of inverse beta decay events. We define the target as the Gd-doped liquid scintillator contained within a detector's inner acrylic vessel. The number of target protons are then the number of Hydrogen atoms within the mass of scintillator in this volume. The number of protons is calculated using $N_p = (M_{Total\ GdLS} - M_{Non-target}) \times \rho_p$ where $M_{Total\ GdLS}$ is the mass of GdLS filled into the detector during assembly, $M_{Non-target}$ is the mass of GdLS in the tubes connecting the acrylic vessel to the overflow tank and overflow tank, and ρ_p is the Hydrogen density of the scintillator.

For the purposes of calculating the absolute number of expected events and uncertainty, the precise chemical composition of the scintillator must be known. Studies of the density and Hydrogen content of the scintillator yield an absolute uncertainty on the target protons of roughly 0.3% [102]. The scintillator is described in more detail in [93, 94]. However, the scintillator is

stored in common tanks and mixed equally when filling all detectors. This implies that it is reasonable to assume that the composition of scintillator between ADs is identical. Thus the relative target proton uncertainty is dominated by the relative mass differences in target liquid between ADs.

The target mass, $M_{Total\ GdLS} - M_{Non-target}$ is monitored continuously, as changes in temperature could cause the amount of liquid in the overflow volumes to change. The system responsible for monitoring the overflow mass is described in [90]. To date, the fluctuations have been well within uncertainties and are therefore treated as constant. Target masses of each detector fall in the range between 19.891 and 19.989 tons. Uncertainties are listed as percentages of a nominal 20 ton target mass. The target proton uncertainty components that are uncorrelated between detectors are dominated by the uncertainty on the total filled mass and are taken as 0.03 % of the nominal target mass. Details of the filling process and mass uncertainty evaluation can be found in [12], which is reproduced in Appendix A.

3.6.2 Detection Efficiencies

Gd-capture efficiency The Gd-capture efficiency is defined as[68]:

$$\epsilon_{Gd} = \frac{N_{IBDw/n-Gd}}{N_{IBDintarget}} \quad (3.3)$$

In order to pass the delayed energy cut at 6 MeV, neutrons from IBD events must capture on Gd. Naturally occurring Gadolinium has a neutron capture cross-section of 4900 barns and produce the main isotopes produce approximately 8 MeV of γ s upon de-excitation. ^{155}Gd (14.8% natural abundance) has a neutron capture cross-section of 517000 barns and releases 8.536 MeV of γ s. ^{157}Gd (15.65% natural abundance) has a neutron capture cross-section of 210000 barns and releases 7.937 MeV of γ s[103]. Hydrogen, meanwhile, has a neutron capture cross-section of 0.3326(7) barns and produces 2.224 MeV of γ s upon de-excitation. This introduces an inefficiency related to neutrons that capture on H rather than Gd. There is also a contribution to this efficiency from “spill-out,” in which neutrons from IBD interactions in the target region escape into the acrylic or the undoped scintillator.

The Gd-capture efficiency has been determined from Monte Carlo studies to be 83.8%, with a 2.2% contribution from spill-out. Its absolute uncertainty is 0.8% based on the level of agreement observed between Monte Carlo studies and AmC neutron source data. Its relative uncertainty is calculated based on differences in the neutron capture times between ADs; it is 0.1% [68].

Spill-in efficiency The spill-in efficiency used for this data period is taken from [68]. Spill-in events consist of an IBD vertex outside the target region where the subsequent neutron capture occurs inside the target. This efficiency represents the ratio of IBD neutrons produced in the detector that capture on Gd to IBD neutrons produced in the target region that capture on Gd.

$$\epsilon_{Spill-in} = N_{AD,Target} / N_{Target,Target} \quad (3.4)$$

The net spill-in efficiency is determined from Monte Carlo simulations to be $105 \pm 1.5\%$. This efficiency is geometry-dependent, and therefore largely correlated between detectors. The degree to which it is not correlated can be estimated based on measured differences between the inner acrylic vessels. Corresponding variations are made in the Monte Carlo and found to have a 0.02% relative uncertainty between ADs.

3.7 Inverse Beta Decay Data Selection

This section describes the data selection and quantifies the inefficiency arising from selection criteria. It follows that described in [69]. For all single events in the detector, selection criteria are applied to ensure that the data evaluated represents as pure an IBD signal as possible. The coincident physics signal consists of a prompt component, caused by the positron and then approximately 30 μ s later a delayed component of around 8 MeV, caused by the n-capture on Gadolinium.

The selection is summarized here with explanations for the efficiencies and uncertainties associated with the cuts used in the following paragraphs. A flasher veto is applied first to remove events caused by PMT light emission. The remaining single events are grouped into coincidence pairs that meet energy and timing cuts associated with the expected IBD signal characteristics. Coincidence candidates are then vetoed if they occur within a specific time window around a muon

event in the water pools or AD. The light yield in the muon event and detector system(s) in which it occurs determine the size of the veto time window. Additionally a multiplicity cut is applied to ensure that coincidences contain only one prompt candidate and one delayed candidate to avoid ambiguity and possible bias in the prompt spectrum. The single event spectrum and coincident IBD candidates are shown in the upper and lower panels, respectively, of Figure 3.9.

3.7.1 Vetoes

Flashing PMTs Light produced by arcing PMTs causes spurious events over the entire energy range of the detector. The cause of this is not known. Flashing PMTs produce a characteristic pattern of hits with most of the event's charge observed by the flashing PMT and the PMTs directly across the detector. Such events account for around 5% of the AD triggers and appear to originate with about 5% of the PMTs. An example flasher event is shown in the left half of Figure 3.10. A discriminator is used to remove signal from flashing PMTs based on event charge and topology.

$$FID = \log_{10}\left[\left(\frac{Q_{Max}}{0.45}\right)^2 + Quad^2\right] \quad (3.5)$$

where Q_{Max} is the fraction of the event charge seen by the PMT with the most charge. $Quad$ is $Q_3/(Q_2 + Q_4)$ where the PMTs are divided into four six-column groups based on their physical position within the detector. Q_1 is the quadrant containing the PMT with Q_{Max} , and Q_3 is the quadrant comprising the six PMT columns on the opposite side of the AD. Events with $FID > 0$ are rejected. A distribution of FID values are shown in the right half for Figure 3.10. Inefficiency in the flasher cut comes from more poorly discriminated low energy events. It is evaluated by looking for IBD-like events that have FID around 0 and found to be $99.98\% \pm 0.01\%$ [68].

Muons Cosmic ray muons are a troublesome source of background. They can produce coincident signals that mimic inverse beta decay. High energy muons produce spallation neutrons that can capture on materials in and around the detectors resulting in gammas. Additionally, they produce unstable isotopes that will β decay, potentially hundreds of milliseconds after the muon has passed. To minimize the impact of cosmic muons on the signal, events occurring in a time window around detector or water pool muons are vetoed. Events from $2 \mu s$ before to $600 \mu s$ after a water

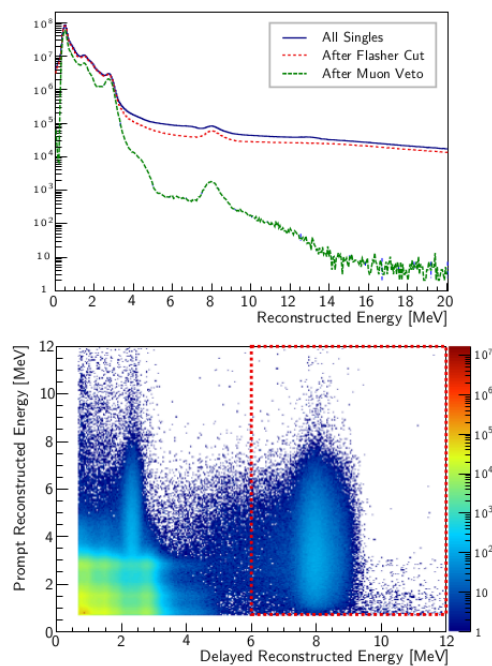


Figure 3.9 The singles spectrum illustrating the reduction of spurious signal by the flasher cut and the muon veto. The peak at 8 MeV is from neutron captures on Gadolinium, which forms the delayed component of the IBD signal. The bottom image shows the distribution of coincidences with in prompt and delayed energy. The red region contains the IBD signal.

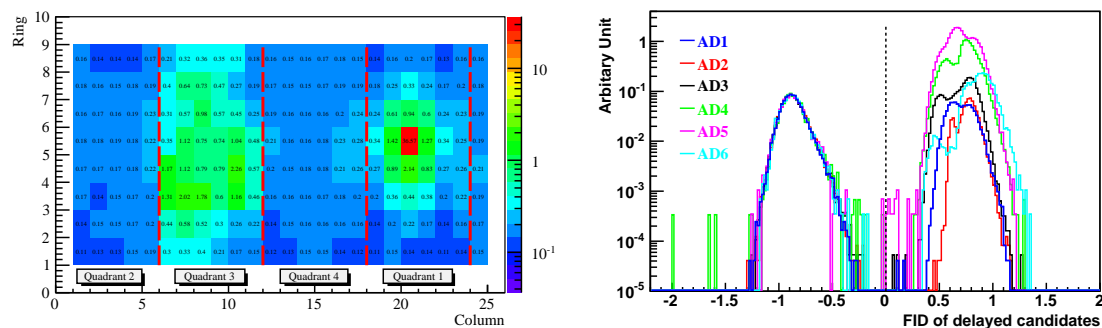


Figure 3.10 A characteristic flasher hit pattern (left). The flasher discriminator used in IBD selection (right). From [68]

pool event with > 12 hit PMTs are removed from ADs in that water pool. Events from $2 \mu\text{s}$ before to $1400 \mu\text{s}$ after an AD event with a total charge of > 3000 p.e. are removed from that AD. Events from $2 \mu\text{s}$ before to 0.4 s after an AD event with a total charge > 300000 p.e. are also removed from the data. The uncertainty from muon identification efficiency is negligible[69]. The detection inefficiency caused by vetoed time around muons is hall-dependent due to the varying overburdens. The values are calculated from the data and combined with the multiplicity cut efficiency. These are listed in Table 3.4.

Multiplicity Prompt and delayed candidates must fall within a 1 to $200 \mu\text{s}$ window. The multiplicity cut requires that there are no additional events over 0.7 MeV in a $400 \mu\text{s}$ window preceding each delayed candidate and no events above 6 MeV in a $200 \mu\text{s}$ window following the delayed candidate. Like the muon veto efficiency, it is calculated from data with negligible uncertainty[69]. Its value is summarized in Table 3.4.

3.7.2 Coincidence selection

Daya Bay is optimized to look for a coincident signal in which the prompt component is caused by a positron and the delayed component is caused by the neutron capture and subsequent de-excitation of a Gd atom. Application of a large number of cuts is undesirable due to the detection uncertainties they would introduce. Therefore, after removing events due to flashing PMTs or muons and with ambiguous coincidences, cuts are only applied to maintain the timing and energy distribution of the IBD signal. Their efficiencies and uncertainties are described in [68] and summarized below.

Capture time cut The capture time cut is $1 < \Delta t < 200 \mu\text{s}$. The efficiency is evaluated by comparing events with $\Delta t > 200 \mu\text{s}$ or $\Delta t < 1 \mu\text{s}$ to those passing the cut. The efficiency is 0.986 with a relative uncertainty of 0.01% . The absolute uncertainty is evaluated comparing AmC data and Monte Carlo and found to be 0.12% . The inefficiency comes mostly from events occurring

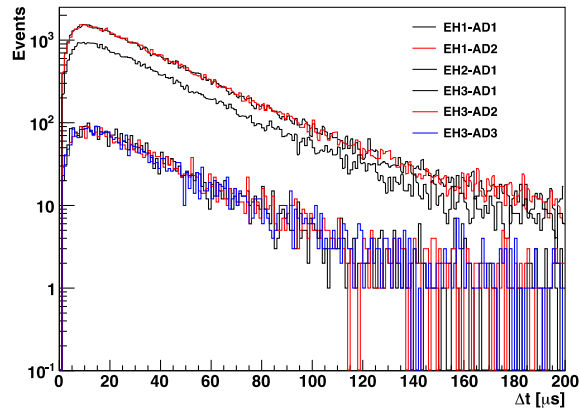


Figure 3.11 The neutron capture time for coincidences in all six detectors. From [100].

at times later than $200 \mu\text{s}$ (1.2%) with the remaining ones too early (0.2%). The capture timing distributions for all ADs is shown in Figure 3.11.

Delayed energy cut The delayed energy cut requires $6 < E_{\text{delayed}} < 12 \text{ MeV}$. Distributions of the delayed event energies in all ADs are shown in Figure 3.12. Its efficiency is $90.9\% \pm 0.6\%$. The absolute uncertainty comes from the difference between the efficiency in data and Monte Carlo extrapolated to cover the region below 6 MeV. It is evaluated based on the fraction of events from 6 to 7 MeV compared to all events from 6 to 12 MeV. The relative uncertainty on the delayed energy cut is 0.12%, and is obtained by comparing the number of events in a window around 6 MeV whose size is proportional to the energy scale differences between ADs.

Prompt energy cut The prompt energy cut is $0.7 < E_{\text{prompt}} < 12.0 \text{ MeV}$. Inefficiency comes from positrons with energies near the threshold depositing energy in non-scintillating volumes (i.e. the IAV) and falling below the threshold. Absolute efficiency is determined to be $99.88\% \pm 0.1\%$ with uncertainty evaluated based on differences between data and MC for nonlinearity and positional non-uniformity. The relative uncertainty is taken from asymmetries in the AD energy scales evaluated with a ^{60}Co source near the edge of the target region. A 2% difference in the energy scale leads to a 0.01% relative efficiency uncertainty[68].

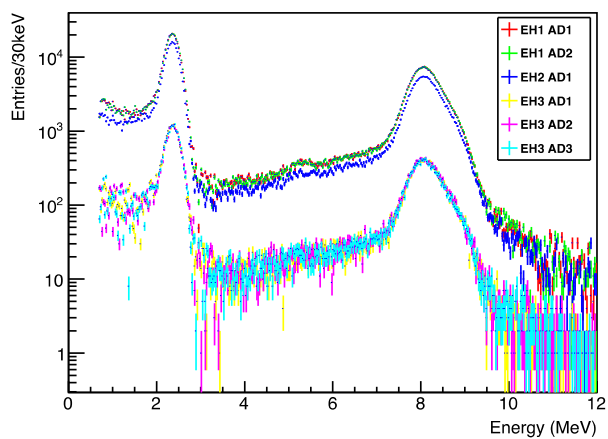


Figure 3.12 The distribution of delayed events in energy. The uncertainty on the delayed energy cut comes from the proportion of events around 6 MeV. From [100].

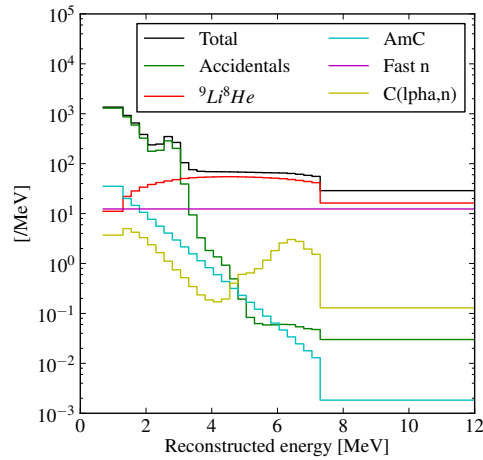


Figure 3.13 The expected background spectrum for AD1 for the full 6-AD data set. Contributions from individual components are shown.

3.8 Backgrounds

Inverse beta decay's coincident signal reduces potential backgrounds. Background sources that lead to correlated events and are not removed by the vetoes in data selection are the primary concern. The five considered backgrounds are summarized briefly in the following subsections in, roughly, decreasing order of contribution to the event rates. More detailed descriptions can be found in [68]. The total expected background spectrum for AD1 for the six-AD data period is shown in Figure 3.13; spectra are similar for other detectors. The expected background rates in each AD are included in Table 3.4.

3.8.1 Accidentals

Accidentals are the largest source of background. Accidental events occur when two single events happen to occur within the trigger time window and satisfy the IBD selection criteria. The measured single rates give an accidental rate in the final data set of 9.45 ± 0.03 , 7.44 ± 0.02 , and 2.92 ± 0.01 /AD/day at EH1, 2, and 3, respectively. The rate's stability over time in each AD is illustrated by Figure 3.14.

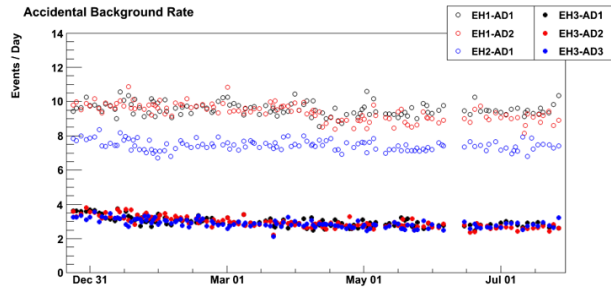


Figure 3.14 The accidental rates in each AD as a function of time during the data period considered in this work. From [100]

3.8.2 Cosmogenic Isotopes

Spallation neutrons from cosmic-ray muons passing through or near the ADs produce ${}^9\text{Li}$ ($\tau_{1/2} = 178.3$ ms and $Q = 13.6$ MeV[104]) and ${}^8\text{He}$ ($\tau_{1/2} = 119$ ms and $Q = 10.65$ MeV[104]) among other cosmogenic isotopes. The long half-lives of ${}^9\text{Li}$ and ${}^8\text{He}$ make them difficult to veto. When they decay, the β can form the prompt component of a coincidence. The delayed component comes from a neutron emitted along with the β or subsequently when the daughter nucleus disintegrates. The cosmogenic background rates per AD are 2.4 ± 0.86 , 1.2 ± 0.63 , and 0.22 ± 0.06 /day at EH1, 2, and 3, respectively. The cosmogenic background rate in each detector is constrained by looking at the time since last muon, illustrated in Figure 3.15 from [100].

3.8.3 Fast Neutrons

Fast neutrons are products of cosmic-ray spallation. They can elastically scatter with protons around and in the ADs, ultimately capturing on Gd in the target regions. Energy deposition from the scattering interactions causes a prompt signal component and the Gd capture gives the corresponding delayed event. The prompt-energy spectrum is observed to be flat when looking at coincidences with prompt energy up to 50 MeV. Rates in each hall are calculated by integrating the fitted flat line over the 0.7 to 12 MeV prompt range. The rates are 0.92 ± 0.46 , 0.62 ± 0.31 , and 0.04 ± 0.02 /AD/day at EH1, 2, and 3, respectively.

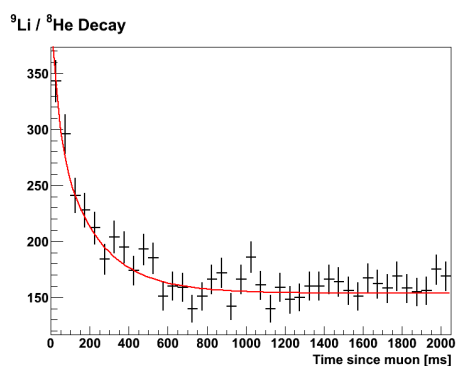


Figure 3.15 Distribution of events as a function of time since last muon. The 0 ms to 1000 ms region comes from cosmogenic isotopes ^9Li and ^8He . At longer times, the distribution shows the uncorrelated background. From [100].

3.8.4 AmC Neutron Source

The automatic calibration units (ACUs) above each AD contain weak (roughly 0.7 Hz neutron rate) $^{241}\text{Am}^{13}\text{C}$ neutron sources. When the sources are being housed above the detector, neutrons can inelastically scatter from and ultimately capture on metal nuclei in the surrounding structure. The scattering events can lead to a prompt event and the subsequent captures produce γ s that may cause delayed events. The AmC neutron rate is estimated from MC and special calibration data to be $0.26 \pm 0.12/\text{day}$ in all ADs. The spectrum of the AmC background was studied using a strong source (59 Hz neutron rate) placed on top of one of the EH3 ADs[105]. The background shape is modeled with an exponential, $p_0 e^{-E/p_1}$, where the two parameters are determined from a fit to the strong source data. Due to the similarity of the sources in each AD, the contribution is treated as correlated between detectors.

3.8.5 $\text{C}(\alpha, \text{n})$

^{13}C has a natural abundance of 1.1% and an (α, n) cross section that varies between 1 mb and 1000 mb over the 0.7 MeV to 7.9 MeV range[106]. The interaction can produce protons and gammas at low energy and at high energy the 6.05 and 6.13 MeV excited states of $^{16}\text{O}^*$ can produce gammas and electron/positron pairs. Natural radioactivity from $^{235,238}\text{U}/^{232}\text{Th}/^{210}\text{Po}$ has α rates of 1.4, 0.05/1.2/10 Bq in AD1. Combining the measured cross section and α rates in each detector, this background can be modeled and studied with Monte Carlo simulations. The overall rate of IBD candidates from $^{13}\text{C}(\alpha, \text{n})^{16}\text{O}$ is less than 0.1/AD/day in each detector. From simulations, it is assigned a 50% uncertainty.

3.9 Nominal Energy Response Model

For a rate-only oscillation result, an absolute understanding of the detectors' energy response is of limited interest. It will effect the absolute efficiency of the energy cuts placed on the prompt and delayed IBD signal components, but as long as these can be shown to be consistent between detectors, there is minimal contribution to the oscillation measurement. Interpretation of oscillation

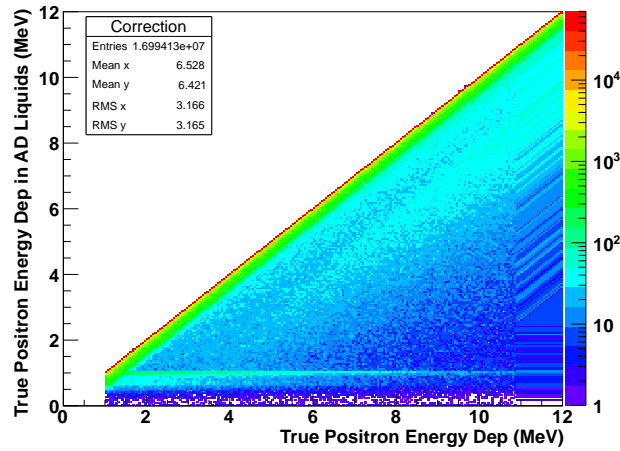


Figure 3.16 The IAV energy loss conversion matrix. From [107]

results involving the spectra requires a better-quantified understanding of the detectors' energy response. Evaluation of the mass-splitting requires an understanding of the absolute energy where the maximum deficit due to $\sin^2 2\theta_{13}$ occurs. Likewise, to understand the compatibility between the predicted and observed IBD spectra, it is necessary to have a model that relates the true physical energy of the prediction with the observed energy of the data. This section outlines the nominal model of the ADs' energy response.

3.9.1 Inner Acrylic Vessel Energy Loss

Positron and gamma energy deposited in the inner acrylic vessel is not converted to scintillation light. This leads to a downward shift in the observed energy. A Monte Carlo study was conducted to determine the amount of positron energy deposited in the scintillator compared to the total deposited positron energy[107]. The results imply that distortion is largely caused by energy loss of the electron-positron annihilation gammas in the acrylic. A correction matrix determined in this study and shown in Figure 3.16 relates true positron energy to energy deposited in the scintillator. When calculating the expected prompt IBD spectrum, this correction is applied to the prediction in "true" positron energy.

3.9.2 Nonlinearity of Energy Response

There are two intrinsic sources of nonlinearity in the energy response of Daya Bay's ADs. The first is from the scintillator light output, which varies with deposited energy and particle type. Scintillator quenching occurs when the energy deposited in the scintillator goes into excitations that do not lead to fluorescence. The amount of quenching depends on the particle type and energy. Scintillator nonlinearity can be described empirically, for example by Birks' Law[108].

The second source of nonlinearity comes from the detector electronics' response. This additional nonlinearity is introduced partly by the hit selection used in energy reconstruction. By default reconstruction algorithms use the first (primary) hit seen on each channel. This choice eliminates possible energy over-estimates due to PMT afterpulses or ringing, but it also removes any legitimate secondary hits, which will result in an under-estimate of the energy from events producing large numbers of p.e..

Elements of the nonlinearity are constrained by calibration and included in the energy reconstruction algorithm, with residual contributions accounted for by a nonlinearity model. Models of the detector nonlinearity relate energy deposited in the scintillator to reconstructed energy. There are several possible methods for constructing an overall nonlinearity model. One is chosen as a nominal model and uncertainties are set based on mixing the nominal and alternative models.

Daya Bay's current nominal nonlinearity model[109, 69] is determined by combining an empirical treatment of the scintillator nonlinearity and a double exponential function to model the electronics nonlinearity.

$$f_{scint} = \frac{E_{vis}}{E_{true}} = \frac{p_0 + p_3 \cdot E_{true}}{1 + p_1 \cdot e^{-p_2 \cdot E_{true}}} \quad (3.6)$$

$$f_{elec} = \frac{E_{vis}}{E_{rec}} = (1 - 0.05e^{E_{rec}/1.75}) \cdot (1 - \alpha e^{E_{rec}/\tau}) \quad (3.7)$$

where E_{true} is the energy deposited in the scintillator, E_{vis} is the energy converted into scintillation light, and E_{rec} is the corresponding energy obtained by the reconstruction algorithm. The parameters p_n , α , and τ are obtained with a fit to the ^{12}B background spectrum and a collection of single gamma calibration peaks. The result of the fit compared to the gamma peaks is shown in Figure 3.17. The measured ^{12}B spectrum compared to the nonlinearity fit results is shown in

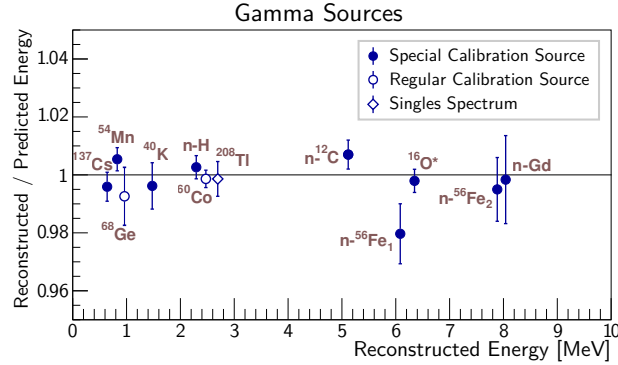


Figure 3.17 The ratio of reconstructed to expected energy from calibration sources and radioactive decays in the singles spectrum. From [69]

Figure 3.18. The nominal full nonlinearity is then given by

$$\frac{E_{rec}}{E_{true}} = f_{elec}/f_{scint} \quad (3.8)$$

where parameters have been replaced with their best-fit values. The consistency of the nominal nonlinearity has been checked against the continuous spectra from ²⁰⁸Tl, ²¹⁴Pb, and ²¹²Pb as shown in Figure 3.19. While uncertainties in the predicted shapes of these spectra are large compared to ¹²B, they are also generally consistent with the nonlinearity model.

Alternative nonlinearity models have been constructed based on different treatment of the scintillator and electronics components. They have been found consistent within 1.5% [109]. Conservatively, the uncertainties on the positron response model are calculated by mixing a combination of nominal and four alternative nonlinearity models:

$$\frac{E_{rec}}{E_{true}} = \frac{E_{rec}}{E_{true, i=1}} \times \left(1 + \sum_{i=2}^{i=5} \alpha \cdot \left(\frac{E_{rec}}{E_{true, i}} \right) \right) \quad (3.9)$$

The nominal model and resulting uncertainty band are shown in Figure 3.20. This nominal model can be applied to the predicted IBD spectra at each AD using a toy Monte Carlo, described in more detail in Chapter 4. The resulting AD and energy bin correlations and uncertainty on the predicted spectrum is shown in Figure 3.21.

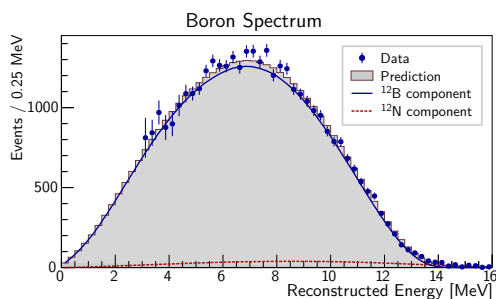


Figure 3.18 The measured ^{12}B spectrum compared to the expectation from the nominal detector nonlinearity model. From [69]

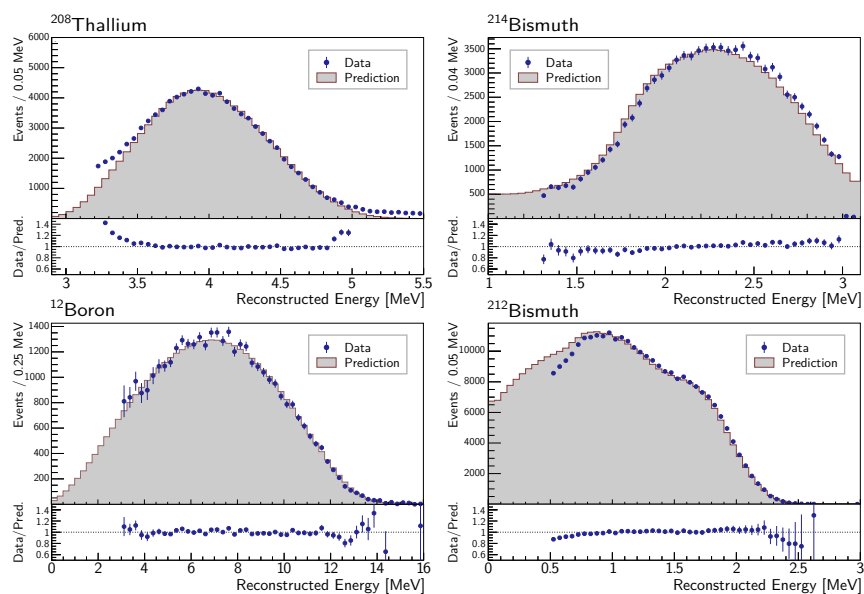


Figure 3.19 The nominal nonlinearity model compared to measured β spectra from ^{12}B and additional backgrounds. From [100]

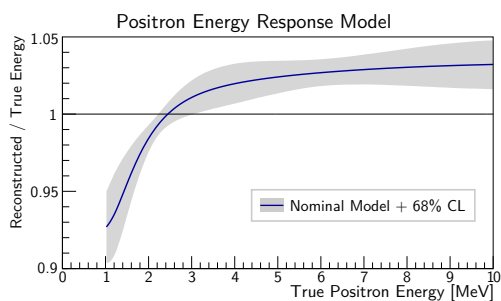


Figure 3.20 The nominal positron nonlinearity and uncertainty band obtained from combining alternative models. From [69, 109].

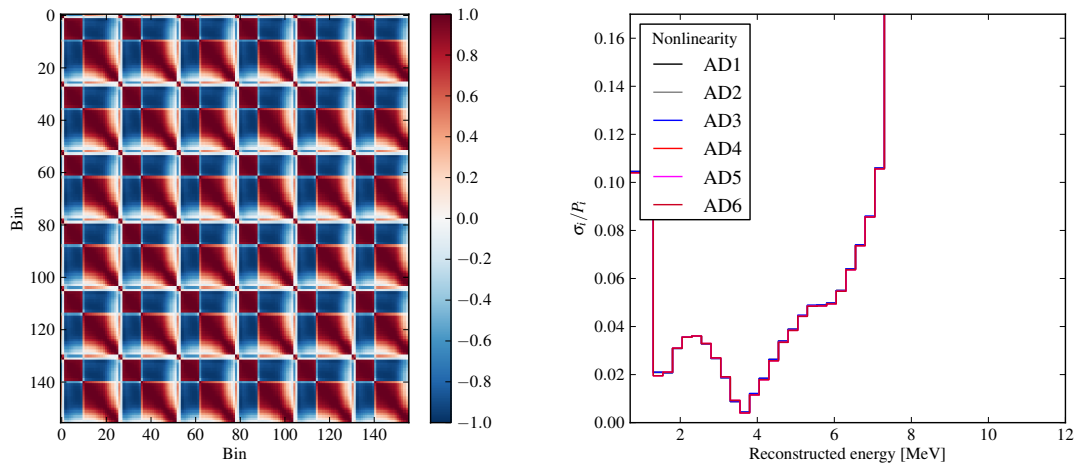


Figure 3.21 Correlation matrix (left) for detector energy nonlinearity uncertainties in detected IBD spectrum and corresponding fractional uncertainties at each AD (right).

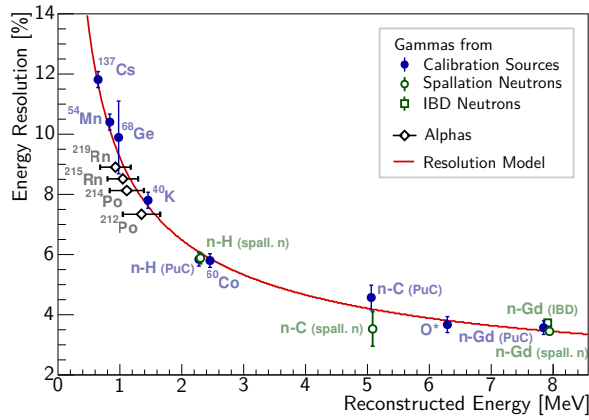


Figure 3.22 The energy resolution compared to peak positions of various gammas in the detector.
From [69]

3.9.3 Energy Resolution

The function form of the energy resolution is given by:

$$\frac{\sigma_E}{E} = \sqrt{p_0^2 + \left(\frac{p_1}{\sqrt{E}}\right)^2 + \left(\frac{p_2}{E}\right)^2} \quad (3.10)$$

Parameters p_0 , p_1 , and p_2 are determined from a fit to calibration and signal peaks in the data. Their values are 1.48%, 8.69%, and 2.71%. It is fixed in the oscillation analysis. Figure 3.22 shows the energy resolution compared to calibration source peaks.

3.10 Summary

The expected event rates in each AD depend on a collection of efficiencies. The values are summarized in Table 3.3. Absolute detection uncertainties are correlated between detectors. Relative detection uncertainties are uncorrelated between detectors and represent the degree to which the detectors are not identical. For the data analyzed in this work, relative uncertainties on the detection efficiency are used in the oscillation fit. Information on the background rates and a summary of the data collected are listed in Table 3.4.

Contribution	Efficiency \pm Absolute Uncertainty	Relative Uncertainty (%)
Target protons	$7.169 \cdot 10^{28} \pm 0.3\%$	0.02
Gd-capture	$83.8\% \pm 0.8\%$	0.1
Spill-in	$105.0\% \pm 1.5\%$	1.5
Livetime	$100.0\% \pm 0.002\%$	0
Cuts:		
Delayed energy	$90.9\% \pm 0.6\%$	0.1
Prompt energy	$99.88\% \pm 0.1\%$	0.01
Capture time	$98.6\% \pm 0.12\%$	0.02
Flasher	$99.98\% \pm 0.01\%$	0.01
Total:	78.8 ± 1.9	0.2

Table 3.3 Summary of detection efficiencies along with absolute (AD-correlated) and relative (AD-uncorrelated) uncertainties affecting the absolute expected rate. Numbers are consistent with those in [68]. Multiplicity and muon veto efficiencies vary by detector and are listed in Table 3.4.

IBD summary	AD1	AD2	AD3	AD4	AD5	AD6
Target mass [ton]	19.941	19.966	19.891	19.913	19.991	19.892
Livetime [d]	191.001	191.001	189.645	189.779	189.779	189.779
ϵ_{det}	0.798	0.798	0.798	0.798	0.798	0.798
$\epsilon_{\mu} \cdot \epsilon_{mult}$	0.795672	0.792652	0.82822	0.957655	0.95684	0.956643
IBD candidates	101290	102519	92912	13964	13894	13731
IBD rates [/d]	653.3 ± 2.31	664.15 ± 2.33	581.97 ± 2.07	73.31 ± 0.66	73.03 ± 0.66	72.60 ± 0.66
Backgrounds [/d]						
Accidentals	9.54 ± 0.03	9.36 ± 0.03	7.4 ± 0.2	2.96 ± 0.01	2.92 ± 0.01	2.87 ± 0.01
Cosmogenic	2.4 ± 0.9	2.4 ± 0.9	1.2 ± 0.6	0.22 ± 0.06	0.22 ± 0.06	0.22 ± 0.06
Fast neutron	0.92 ± 0.46	0.92 ± 0.046	0.62 ± 0.31	0.04 ± 0.02	0.04 ± 0.02	0.04 ± 0.02
C(α, n)	0.08 ± 0.04	0.07 ± 0.04	0.05 ± 0.03	0.04 ± 0.02	0.04 ± 0.02	0.04 ± 0.2
^{241}AmC	0.26 ± 0.12	0.26 ± 0.12	0.26 ± 0.12	0.26 ± 0.12	0.26 ± 0.12	0.26 ± 0.12

Table 3.4 The summary of IBD candidate events and expected backgrounds. From [69].

Chapter 4

Predicted Reactor Antineutrino Spectrum

The Daya Bay Experiment measures antineutrinos produced by the six pressurized water reactor cores at the Guangdong Nuclear Power Complex in outside of Shenzhen, China. Oscillation results depend on a comparison of the measured antineutrino flux and spectrum at multiple distances from the cores. Detectors placed in the near sites between 300 m and 500 m from the cores primarily serve to provide a normalization of the flux at a short distance where oscillation has not yet occurred. Comparing spectra measured between the near and far detectors allows the oscillation parameters $\sin^2 2\theta_{13}$ and Δm_{ee}^2 to be extracted with minimal impact from the reactor uncertainties. This strategy was suggested by [83] as a way of maximizing sensitivity to a potentially small $\sin^2 2\theta_{13}$, as the signal rate uncertainties related to the reactor flux are larger than 1% [62].

The spectrum of antineutrinos produced at a nuclear reactor is given by

$$S_{core}(E, t) = \frac{dN}{dE_{core}}(E, t) = \sum_i \left(\frac{W_{th}(t)}{\sum_i f_i(t) e_i} \times f_i(t) \times S_i(E) \times c_i(E, t) \right) \quad (4.1)$$

where W_{th} is the thermal power of the reactor and f_i , e_i , and S_i are the fraction of fissions, energy released per fission, and antineutrino spectrum of fission daughters, respectively, for each fissioning isotope, i , in the core. A correction, $c_{non-eq,i}(E, t)$, is applied to corrects for the S_i its time-dependence. The majority of fissions in a pressurized water reactor using UO_2 fuel come from ^{235}U , ^{239}Pu , ^{238}U , and ^{241}Pu . Except for ^{238}U , which fissions when bombarded with fast neutrons, these isotopes primarily undergo fission induced by thermal neutrons. Additional neutrinos above the inverse beta decay (IBD) threshold are also produced in spent fuel pools from β decays in decay chains where early elements have relatively long half-lives. The total neutrino spectrum produced

in and near the cores is thus approximately:

$$\frac{dN}{dE}_{total}(E, t) = \frac{dN}{dE}_{core}(E, t) + S_{SNFpool}(E, t) \quad (4.2)$$

The core-detector geometry at Daya Bay is relatively complicated compared to that at the Double Chooz[59] and RENO[63] experiments. This makes it important to account for the possibility of incomplete correlation in the reactor spectrum measured at each of the ADs. Covariance matrices are generated from a toy Monte Carlo calculation to capture the uncertainties and correlations between energy bins and detectors. Elements of each matrix are calculated as:

$$V_{ij} = \frac{1}{N} \sum_{n=0}^{N-1} (y_i(n) - Y_i) \times (y_j(n) - Y_j) \quad (4.3)$$

where the sum runs over N toy predictions, the Y s represent the nominal prediction, i and j run over the calculation bins in each detector, and the y s represent the prediction corresponding to the n^{th} toy prediction. The method of variation and outputs for each effect are discussed in subsequent sections. Predictions of the “true” neutrino flux at each detector are calculated based on power company-supplied thermal power and fuel composition data. This is combined with external information on the energy released per fission and neutrino spectrum for each fissioning isotope. Additional information is used to calculate time-dependent corrections to the neutrino spectra and additional neutrino flux due to spent fuel stored near the reactor cores.

Subsequent sections of this chapter discuss the elements of the reactor prediction and the evaluation of their uncertainties and correlations in the measured IBD spectrum. Section 4.1 summarizes the application of the nominal detector response model to the predicted spectrum. Section 4.2 describes the information provided by the power company about the power output and fission composition of each reactor. Section 4.3 discusses the energy released per fission. Section 4.4 discusses the treatment of the neutrino spectra from each of the isotopes in the reactors. Section 4.5 discusses the irradiation time correction to the isotope spectra. Section 4.6 discusses the contributions from spent fuel.

4.1 Conversion to Reconstructed Energy

To prepare covariance matrices that describe the uncertainties from the reactor models that apply to the observed prompt spectrum, the predictions must be converted from neutrino energy into reconstructed energy. Employing the reactor spectrum of Equation 4.1, the detected IBD spectrum in neutrino energy will be

$$\frac{dN}{dE_{ad}}(E) = \int dt \sum_{core} \frac{N_{p,ad}}{4\pi L_{ad,core}^2} P_{ee}(L_{ad,core}, \theta_{13}, \Delta m_{ee}^2, E) S_{core}(E, t) \sigma_{IBD}(E) \epsilon_{ad}(E, t) \quad (4.4)$$

where $N_{p,ad}$ is the number of target protons in the ad^{th} AD, P_{ee} is the electron antineutrino survival probability, σ_{IBD} is the inverse beta decay cross section, and $\epsilon_{ad}(E, t)$ encapsulates elements of the detection efficiency and energy response of a particular AD. We note that in Equation 4.4, the location of spent fuel can be accounted for by substituting $L_{ad,core} \rightarrow L_{ad,pool}$ and $S_{core} \rightarrow S_{SNFpool}$ and summing over both cores and spent fuel pools. Summing over cores and then integrating over time gives the expected IBD spectrum of events physically occurring in the target during the data period in terms of neutrino energy. The DAQ livetime for each hall and number of target protons for each AD are incorporated into this initial calculation.

Next, the prediction in neutrino energy is converted into prompt energy and scaled by the detection efficiencies and the combined muon+multiplicity veto efficiency. The prompt energy accounts for the positron kinetic energy and the mass energy from the annihilation gammas. To zeroth order, the prompt energy is given by $E_{prompt} = E_{\bar{\nu}} - (m_n - m_p) + m_e \approx E_{\bar{\nu}} - 0.78$. A more precise conversion, including angular dependence of the IBD cross section is calculated based on [91] and plotted in Figure 4.1.

The E_{prompt} prediction is converted to visible energy, E_{vis} by applying a correction for energy lost into the non-scintillating inner acrylic vessel (IAV)[107]. The IAV correction is summarized in Section 3.9.1. Next, the nominal positron nonlinearity model is applied to convert from visible, E_{vis} , to reconstructed energy, E_{rec} . This introduces an energy-dependent stretch of predicted spectrum. This model is described in [69] and illustrated in Figure 3.20. As a final step, the resulting spectrum is smeared to account for the energy resolution. The energy resolution is described in

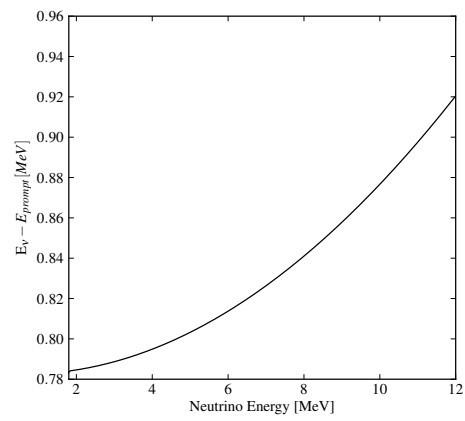


Figure 4.1 Neutrino energy to prompt (positron plus annihilation gamma) energy conversion.

Section 3.9.3 and shown in Figure 3.22. Plots in the remaining sections of this chapter have been converted into this nominally-reconstructed energy, unless otherwise indicated.

4.2 Power Company Data

The power company provides Excel spreadsheets with reactor operating information to a subset of the collaboration. The files contain daily average power of each core (W_{th}), simulated fission fractions for each fuel cycle of each core (f_i), and a set of burnup anchor points used to relate each core's fission fractions to specific points in time. Information on the fission fractions and power can be shared internally within the collaboration after averaging over time periods of weeks or longer. Information in the form of aggregate neutrino or IBD spectra can be released publicly.

Full power of all cores at the Daya Bay and Ling Ao power plants is 2.895 GW_{th} . The power company provides a daily average power for each core. Nominally, these averages are computed from 24 hourly measurements. For a particular physics analysis period, this may induce a bias in the observed antineutrino rates. For example, if the experimental data-taking time is not comparable to the hours over which the power company average is calculated. To avoid this, the collaboration provides information on experiment up-time, measured in terms of “good hours”, to the power company[110]. They then recompute the power averages so they are properly weighted to the correspond data-taking periods. The differences between these averages has generally been consistent to less than 0.1%. Occasionally, 1%-level differences occur on days when cores are being shut down for maintenance or turned back on after a shutdown.

Along with the daily power spreadsheet, the power company provides a collection of the burnup anchor points for each core. Burnup is a measure of the amount of energy released per mass of fuel during the current cycle, expressed in units of MWdays/MTU. MTU is the mass of Uranium oxide fuel in each core. The nominal value for the Daya Bay and Ling Ao cores is 72.2 tons (metric). At full power, the burnup will increase by approximately 40 MW/MTU per day. The supplied anchor points are provided at approximately semi-monthly intervals.

For use in daily calculations, the burnup is extrapolated from the provided anchors using the daily powers:

$$B(t) = B_{d=0} + MTU \cdot \sum_{d=0}^{d=t-1} W_{th}(d) \quad (4.5)$$

where $B_{d=0}$ is the burnup from the anchor point before the desired date, t , and the sum integrates the daily power since that anchor point. This extrapolation method reproduces the power company-supplied anchor points quite well for the four Ling Ao cores. However, it is consistently 0.4% too high for the D1 and D2 cores. This is handled by adjusting the nominal MTU of the Daya Bay cores to 71.9 tons.

Files containing simulated fission fractions, f_i , for each core are provided as a function of burnup. Isotopic fission fractions are given for ^{235}U , ^{238}U , ^{239}Pu , and ^{241}Pu as well as other isotopes which are not used in the predictions. For current fuel cycles, the simulation provided is based on ideal operating parameters. After the cycle ends, the power company provides an updated simulation file based on the actual operating parameters. The updated simulation files are used in the prediction when available, but they are similar to the ideal files. Burnup points begin at 150 MWdays/MTU and continue with points separated by approximately 1000 MWdays/MTU to the end of the fuel cycle.

The daily fission fractions are calculated by linearly interpolating between supplied points using the daily extrapolated burnup:

$$f_i(t) = f_{i,min} + \left(\frac{B(t) - B_{min}}{B_{max} - B_{min}} \right) \times (f_{i,max} - f_{i,min}) \quad (4.6)$$

For cases where the daily burnup falls outside the range of burnups given in the core simulation, the last specified values are used. In principle, this could introduce a small bias in calculations at the beginning of a fuel cycle where the fuel composition evolves most rapidly. However, given that it takes roughly four days of full-power operation for a core to reach the 150 MWd/MTU point, this will be negligible in data sets that span many months.

	^{235}U	^{238}U	^{239}Pu	^{241}Pu
^{235}U	1	-0.29	-0.62	-0.48
^{238}U	-0.29	1	0.38	0.39
^{239}Pu	-0.62	0.38	1	0.84
^{241}Pu	-0.48	0.39	0.84	1

Table 4.1 Correlations in simulated fission fraction variations between isotopes. From [111].

4.2.1 Fission Fraction Uncertainties

As noted in [111], reactor simulation codes can be validated by comparing their predicted fuel composition to the measured composition of sample fuel rods after removal from the core. There are approximately 5% (relative) uncertainties on the fission fractions produced by such codes. These have correlations between isotopes, which are reproduced in Table 4.1.

For Daya Bay, the power company employs the SCIENCE code to calculate the fission content of the six reactor cores[112]. Given the similar design of the cores and the consistency of the code used by the power company to simulate their operation, this is expected to introduce errors that are correlated between cores with the same burnup. In practice, calculating fluctuations of this variety within the flux prediction code is CPU time-intensive. For data sets where there is similar burnup exposure between different detectors, it is reasonable to treat these uncertainties as correlated in time and between cores. We note that rate-based oscillation results [68] have treated the uncertainty attributed to fuel composition uncertainty as uncorrelated. For relative comparisons, this is a conservative approximation. Meanwhile, for constructing uncertainties associated with the absolute measured spectrum the core-correlated treatment is conservative.

The effect of fission fraction uncertainties on the predicted IBD spectra is evaluated using a toy Monte Carlo simulation. A nominal spectrum is produced using the power company-provided fission fractions without modification. Variations are introduced in the composition of each isotope by generating an initial vector of four random, Gaussianly distributed fluctuations, δ_{init} , with ($\mu = 0$; $\sigma = 0.05$). To obtain proper correlations between isotopes, the Cholesky decomposition, U , of

the matrix in Table 4.1 is used to induce correlation in the variations:

$$\delta_{frac} = \delta_{init} \cdot U. \quad (4.7)$$

The expected IBD spectrum for the data period is then recalculated for each variation with fission fractions scaled by $(1 + \delta_{frac})$. Results for 500 toy spectra are shown in Figure 4.2.

4.3 Energy Released Per Fission, e_i

Roughly 200 MeV is released per fission in a nuclear reactor. Combined with information on the power and fuel composition, the precise values are needed to calculate the number of fissions that have occurred in a core:

$$N_{fission} = \frac{\int_t^{t+\Delta t} W_{th}(t) dt'}{\sum_i f_i e_i}. \quad (4.8)$$

This quantity is scaled by the fission fractions, f_i , to calculate the number of fissions due to each isotope, which in turn is needed to combine the individual $S_i(E)$ when calculating the total spectrum in Eq. 4.1. The energy released per fission for each isotope, e_i , was calculated by James[113] and more recently updated by Kopeikin[114]. Kopeikin notes that there is a slight time-dependence in the values of e_i . We use Kopeikin's mid-cycle values, treated as constants. A subset of the Daya Bay collaboration has also calculated the energy release per fission for the Daya Bay and Ling Ao cores and found an approximate 0.3% shift in the average e_i [115]. This will cause a shift in the expected signal rates, but at a lower level than the power and detection efficiency uncertainties. It will also be correlated between isotopes. Given that the overall correlated normalization is allowed to vary freely in the oscillation analysis and the predictions are normalized to data in the predicted-to-observed spectrum comparison, the shift has not been applied in this work.

4.4 Antineutrino Spectrum, $S_i(E)$

The antineutrino spectrum for each isotope is taken from conversion of β spectra measured at ILL for the three thermally-fissioning isotopes. The original conversion of Schreckenbach et al.[72, 73] is used for the ‘‘old’’ reactor model, referred to as the ILL model. The updated conversion from Huber[19] is used for the ‘‘new’’ reactor model. The expected IBD spectrum and uncertainties per

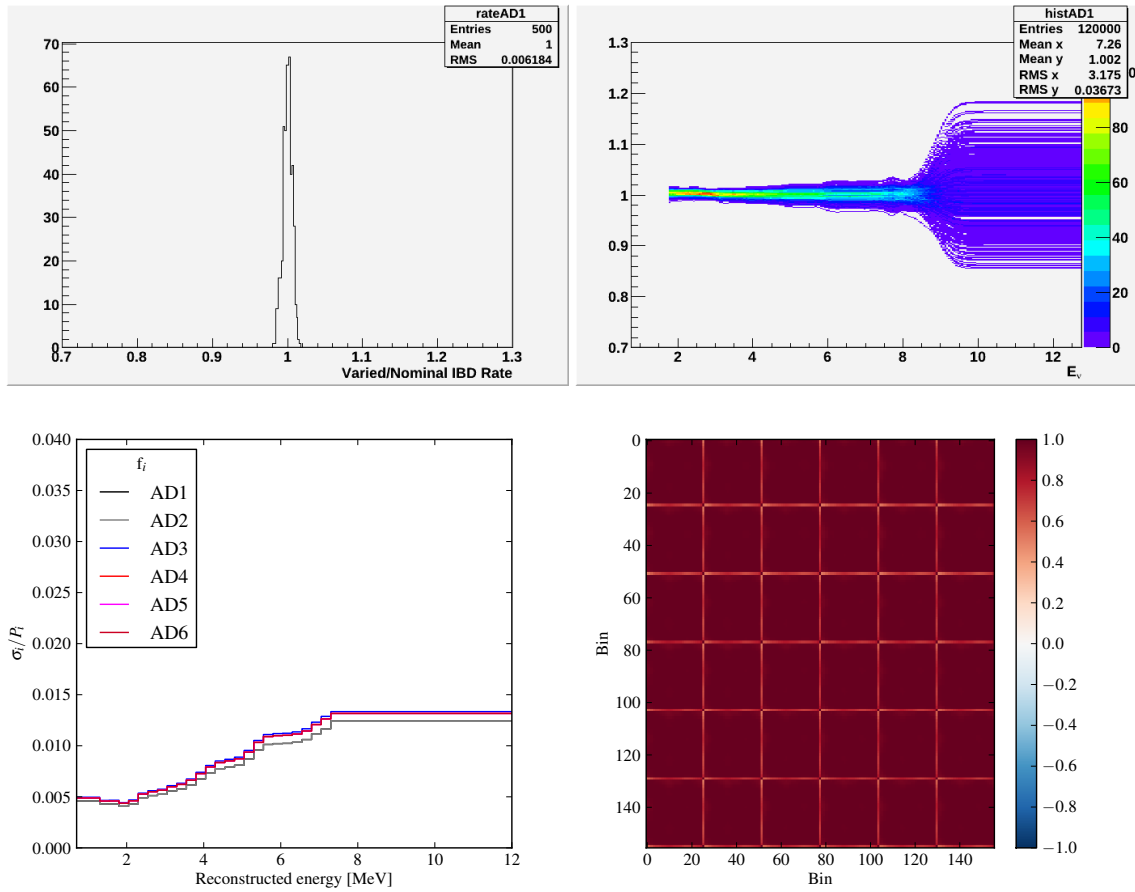


Figure 4.2 In neutrino energy, the IBD rate (top, left) and spectrum (top, right) variations induced at AD1 for 500 variations in the fission fractions. After conversion to reconstructed energy, the proportional uncertainties in the final analysis bins for the IBD spectrum at each AD (bottom left) and correlation matrix (bottom right) are also shown.

fission from each isotope, $S_i(E) \times \sigma_{IBD}$, are shown in Figure 4.3 for each model. Figure 4.4 shows the ratio between predictions based on the new and old reactor models in neutrino energy at each of the three Daya Bay experimental halls.

^{238}U undergoes fission by fast neutrons and until very recently [116, 117] had not been measured directly. Calculations based on theory or a combination of theory with published nuclear data are used for the analysis in this work. For the ILL model, the calculation by Vogel [88] is used. In the Huber model the ab initio calculation given by Mueller et al. [81] is used.

4.4.1 Interpolation and Extrapolation

The $S_i(E)$ tables provided by [72, 73, 88, 19, 81] do not cover the entire IBD region. The lowest energies are around 2 MeV and the high energies are around 8 MeV. Similarly, they list spectra in units [$\nu/\text{MeV}/\text{fission}$] in 0.25 MeV bins. To generate predictions at arbitrary energy, extrapolation must be used outside the supplied ranges and interpolation is used between energies given. A log-linear interpolation is used for arbitrary energy over the table ranges.

The extrapolation method for energies beyond the provided tables differs for each model. As the beta spectra were not measured at these energies, the choice of how to extrapolate is somewhat arbitrary. For the Huber conversion, fits to exponentials of form $e^{\sum_j a_j \cdot E^j}$ with parameters taken from [19] and [81] are used outside the 2-8 MeV window. For the ILL converted fluxes, log-linear extrapolation based on the last two specified points is used beyond the ends of the provided spectra. These choices maintain consistency of isotopic composition in each prediction's high energy region. Figure 4.5 illustrates the results of these treatments in terms of the fraction of predicted IBDs attributable to each isotope over the energies used in each prediction.

4.4.2 Measured Component Uncertainties

In [19], a detailed breakdown is given of the sources of uncertainty in the spectra, $S_{\nu,i}(E)$, from the measured β spectra conversions. Uncertainties are broken into components that are correlated between isotopes and energy bins and components that are uncorrelated between isotopes and energy bins. Supplied uncertainties are interpolated in the same way as the central values for each

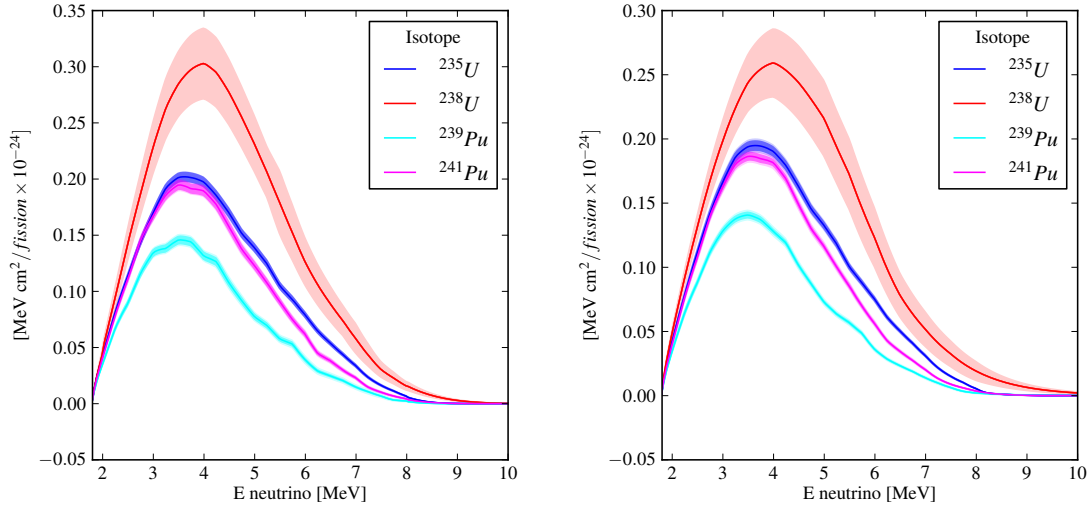


Figure 4.3 The IBD spectrum uncertainties from Huber[19] with ^{238}U from [81] (left) and original ILL conversion[72, 73] with ^{238}U from [88]. The outer band shows the total specified uncertainty for each isotope assuming 0.25 MeV bins; the inner band shows the energy and isotope-correlated components

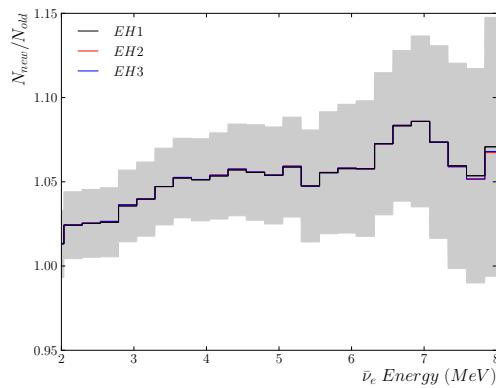


Figure 4.4 The ratio between the expected IBD spectrum calculated using the ILL converted beta spectra to the expectation using the Huber conversion. Differences at each hall are plotted separately to illustrate that differences in predicted IBD spectra are similar at each hall for the six-AD data period, irrespective of the reactor model.

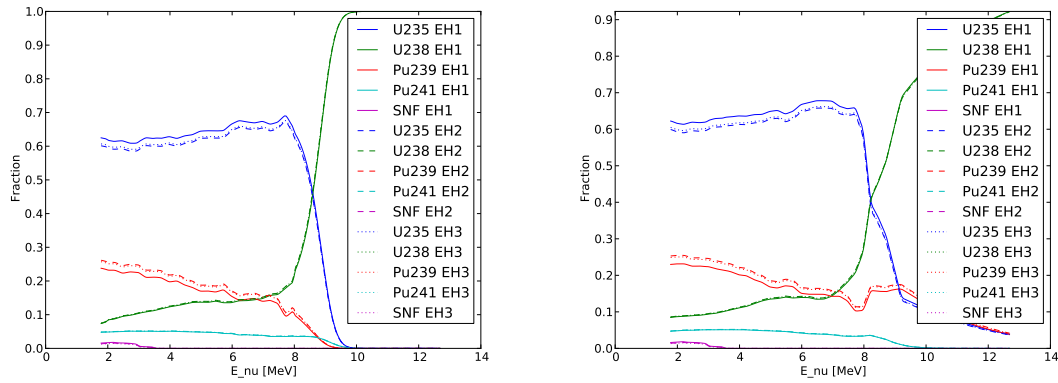


Figure 4.5 The fraction of IBDs coming from each isotope as a function of neutrino energy for the Huber (left) and ILL (right) models. The majority of IBDs come from ^{235}U , however extrapolation of the spectrum above 8 MeV leads to an apparent dominance of ^{238}U at higher energy. The actual composition above 8 MeV is not well known.

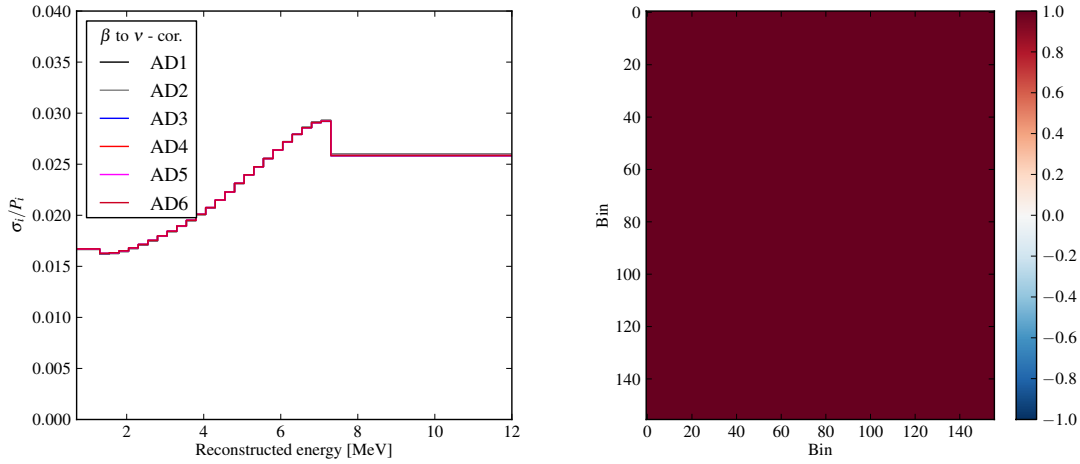


Figure 4.6 Fractional uncertainties at each AD from the energy and isotope correlated components of the β to ν conversion procedure (left). The corresponding correlation matrix is shown for final analysis bins in all detectors (right).

isotope in each model. An exception to this is in the uncorrelated uncertainty components, which are adjusted to ensure that the uncertainty does not become negligible when combining arbitrarily small bins. These are scaled by \sqrt{R} , where R is the ratio old-to-new bin width ($0.25/\Delta E_{new}$).

Correlated components A detailed breakdown of suggested treatment of correlations is given in [19]. For the Huber model, correlated components are taken as suggested and incorporate the uncertainties from the overall normalization of the original beta measurements and from physics effects underlying the conversion procedure. The effective Z effects both the Coulomb correction and the weak magnetism correction to the spectral slopes. In the treatment of the ILL model, only the quoted uncertainties attributed to the conversion procedure in [72] and [73] are included. In computing toy prediction spectra for the correlated components, a single random, Gaussianly distributed parameter, δ , ($\mu = 0$, $\sigma = 1$) is chosen. The toy spectra are computed by scaling all bins of all isotopes' contribution to the prediction for all cores by $(1 + \delta\sigma_{corr}(e))$. Results after application of the nominal detector response model are shown in Figure 4.6.

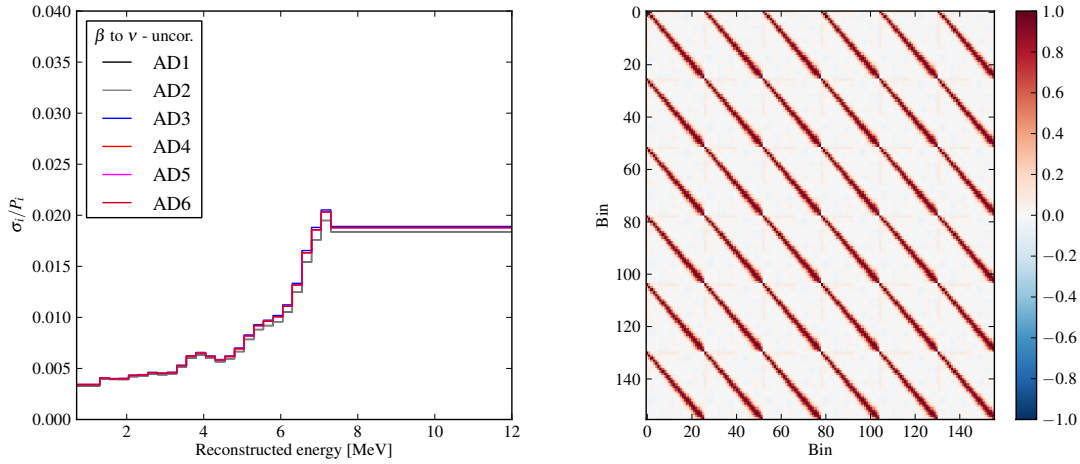


Figure 4.7 Fractional uncertainties at each AD from the energy and isotope uncorrelated components of the β to ν conversion procedure (left). The corresponding correlation matrix is shown for final analysis bins in all detectors (right).

Uncorrelated components In both flux prediction models, the uncorrelated components originate largely with the statistical errors of the ILL beta spectra measurements. In the case of the Huber model, an additional uncorrelated component comes from the Monte Carlo evaluation of the bias introduced by the conversion procedure[19]. In the case of the ILL model, the normalization has been included with the uncorrelated components. This will lead to a slightly greater reduction in the ILL uncertainties when combining bins and slightly less correlation between energy bins compared to the Huber model. In computing toy prediction spectra for the uncorrelated components, a set of δ_e random, Gaussianly distributed parameters ($\mu = 0$, $\sigma = 1$) are chosen for each isotope. The toy spectra are computed by scaling each bin of each isotope's contribution to the prediction for all cores by $(1 + \delta_e \sigma_{uncorr}(e))$. Results after application of the nominal detector response model are shown in Figure 4.7.

4.4.3 ^{238}U Component Uncertainties

The ^{238}U calculation uncertainties are larger than the other isotopes due to their theoretical origin. Their contribution to the IBD prediction uncertainties is calculated under extreme assumptions about the correlation between energy bins. By default, uncertainties are treated as completely

uncorrelated between bins. The uncorrelated case would be expected to yield slightly better agreement in the comparison between predicted and measured IBD spectra, making it conservative. The case in which they are treated as completely correlated has also been checked.

Toy spectra and covariance matrices are calculated for each case in a manner analogous to that for the correlated and uncorrelated uncertainties of the other three isotopes. In the energy-uncorrelated case, a set of random, Gaussianly-distributed parameters, δ_e , ($\mu = 0$, $\sigma = 1$) is generated. The varied spectra are computed by scaling the nominal ^{238}U contribution at all cores by $(1 + \delta_e \sigma_{U238}(e))$. In the energy-correlated case, a single random parameter, δ , ($\mu = 0$, $\sigma = 1$) is generated. The varied spectra are computed by scaling the nominal ^{238}U contribution at all cores by $(1 + \delta \sigma_{U238}(e))$. The resulting uncertainties in the IBD spectrum at each detector and the correlations between energy bins and detectors are shown in Figure 4.8 for each case.

4.5 Non-equilibrium Corrections, $c_i(E, t)$

The ILL spectra were measured at irradiation times of 0.5, 1.6, and 1.8 days for ^{235}U [72], ^{239}Pu [71], and ^{241}Pu [73], respectively. In a typical reactor, irradiation times are on the order of a year or more. The uncorrected ILL spectra will therefore underestimate the flux contribution from decay chains where parent isotopes have long half-lives compared to the ILL irradiation times. One example is the β -decay from ^{106}Ru to ^{106}Rh in which the former has a 372 day half-life ($Q=0.04$ MeV) and the latter has a 30 s half-life ($Q=3.5$ MeV). The contribution to the β and neutrino spectra from ^{106}Rh will increase over time as ^{106}Ru builds up in the cores. Thus the converted spectra should be corrected for a more realistic irradiation time[118].

Calculations for these corrections are made using reactor simulation codes. A specific calculation for the Daya Bay cores was done by a subset of collaborators[119]. Their results are consistent within uncertainties with the results of [81] and [118]. The rest of this section outlines how the calculation provided in [81] can be incorporated into the Daya Bay flux calculation.

Mueller et al.[81] provide off-equilibrium corrections for irradiation times of 1 day (for ^{235}U only) and 100, 115, 300, and 450 days (for ^{235}U , ^{239}Pu , and ^{241}Pu). The provided correction spectra have 500 keV intervals between 2.0 and 4.0 MeV. Above 4.0 MeV the corrections become

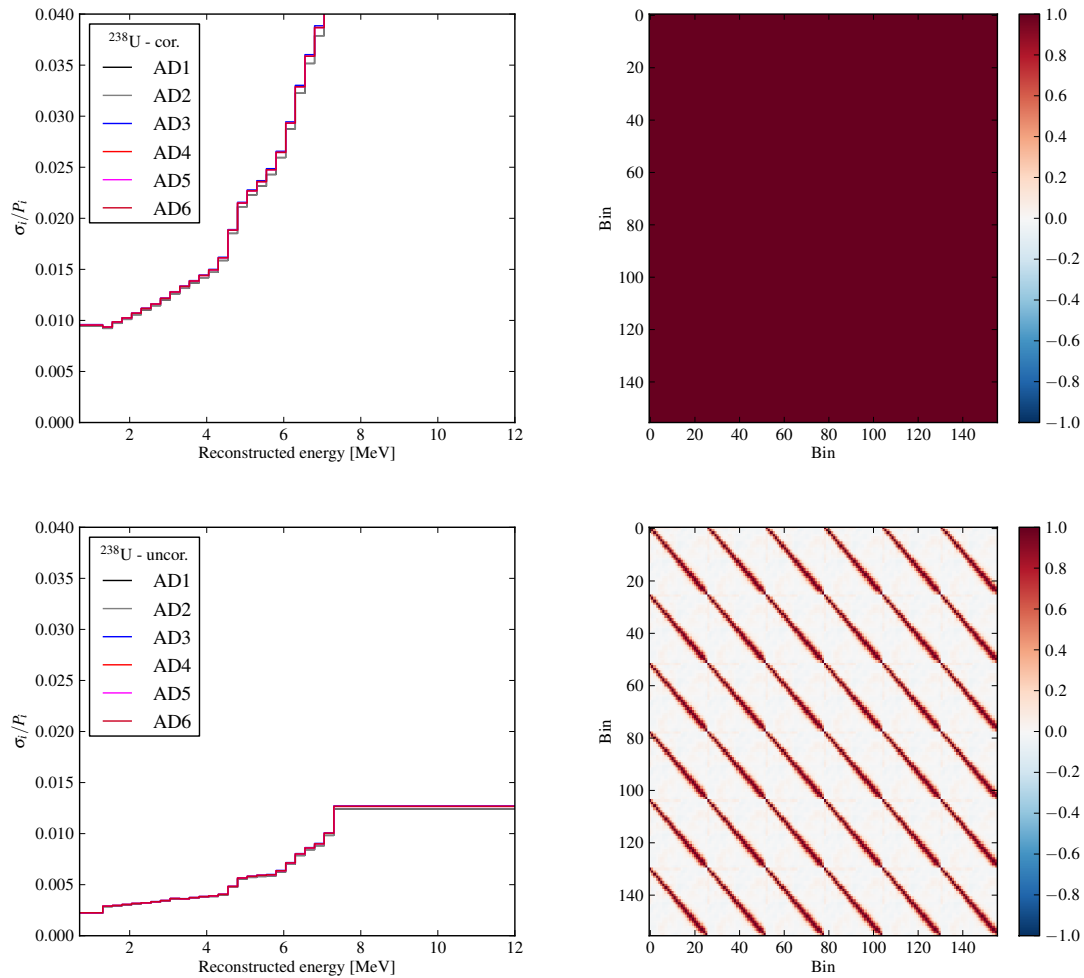


Figure 4.8 ^{238}U uncertainty bands and fractional uncertainties in the predicted IBD spectrum for each AD in the energy-correlated case (top left) and the corresponding correlation matrix (top right). Lower plots show the fractional uncertainties and correlations where ^{238}U uncertainties are treated as uncorrelated in energy.

	$c_{U235}(2 \text{ MeV})$ [%]	$c_{Pu239}(2 \text{ MeV})$	$c_{Pu241}(2 \text{ MeV})$	Avg. Fuel Age [days]
12 m cycle t0	5.0	1.8	1.6	360
12 m cycle tF	5.7	2.1	1.9	720
18 m cycle t0	5.1	1.9	1.7	540
18 m cycle tF	5.7	2.1	1.9	1080

Table 4.2 Magnitudes of non-equilibrium corrections applied to each isotope at 2 MeV at the beginning and end of each core’s fuel cycle. The values reflect the assumption that cores have 1/3 of the fuel irradiated for 0, 1, and 2 full fuel cycles. The size of the corrections falls of to zero by 4.5 MeV.

negligible. The authors consider the 450 day corrections equivalent to the infinite irradiation time values. The ^{238}U spectrum is given for irradiation times of 300 and 450 days. The authors suggest a 30% uncertainty on these corrections that is claimed to cover various consistency checks.

A multiplicative, energy- and time-dependent off-equilibrium correction used in these predictions is obtained by linearly interpolating between the supplied energies and times. For antineutrino energies below 2 MeV, the 2 MeV correction is used. Under the assumption that fuel is rotated through the core in thirds, irradiation time is estimated as:

$$c_i(t) = 1/3 \times (c(t) + c(t + T) + c(t + 2T)) \quad (4.9)$$

where T is the nominal length of a fuel cycle (1 year for L1-4 and 18 months for D1 and D2). Table 4.2 lists the magnitude of the 2 MeV correction for each isotope at the start and end of a fuel cycle from this calculation. The total fraction of IBD events attributed to the off-equilibrium effect is around 0.6% in each AD. Its contribution to the overall signal rate uncertainty is thus 0.2%. The fractional contribution from the non-equilibrium correction in the low energy bins of AD1 is shown in Figure 4.9.

To evaluate the correlations of the non-equilibrium correction between detectors, toy spectra are generated under the assumptions that the corrections are correlated in energy, but may vary independently between isotopes. For each toy spectrum, a set of four random, Gaussianly-distributed parameters, δ_i ($\mu = 0$, $\sigma = 1$), is generated. Each isotope’s contribution to the overall spectrum

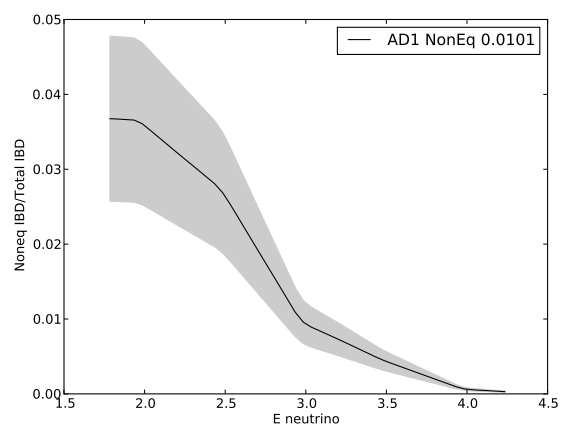


Figure 4.9 Fraction of IBDs attributable to the non-equilibrium correction at AD1.

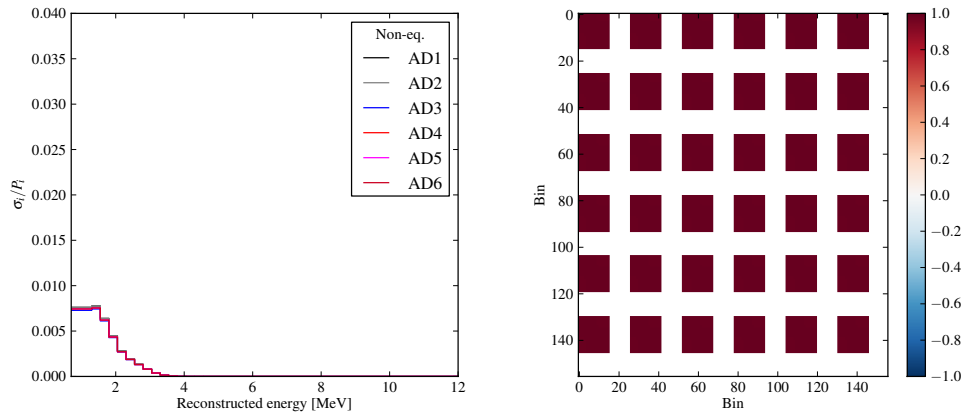


Figure 4.10 Fractional uncertainties at each AD from non-equilibrium corrections (left) and the associated correlation matrix for final analysis bins in all detectors (right).

is then scaled by $(1 + \delta_i \sigma_{noneq,i}(e))$. The resulting uncertainties in the expected signal spectrum at each AD and the correlations between energy bins in all ADs are shown in Figure 4.10.

4.6 Spent Fuel Neutrinos

Between fuel cycles, some fuel assemblies are removed from a core and placed in adjacent pools where they cool before they can be moved off-site. In general, we assume that 1/3rd of fuel assemblies, the spent fuel (SNF), are moved out of the core and replaced with fresh fuel during each shutdown. There will be additional neutrinos produced in the remaining 2/3rd of fuel assemblies that have been irradiated for one or two previous fuel cycles, these are treated as “effective SNF.” The power company does not provide specific details about the number of spent fuel assemblies in each pool or their detailed irradiation histories. Estimates are based on general knowledge of reactor operation and uncertainties are handled conservatively to cover possible deviations from our assumptions. In rate-only analyses[68], the SNF uncertainty is assumed to be 50% of the nominally calculated SNF rate, uncorrelated between cores. In analyses involving the spectral shape, a 100% uncertainty, also uncorrelated between cores, is assumed.

Two subgroups of the Daya Bay collaboration have looked at the SNF flux and its time-evolution[120, 121]. The calculations are generally consistent with each other. For oscillation

analysis results, the spectrum is taken from [120] with the normalization adjusted to peg the SNF flux at 0.3% of the nominal core flux. The calculation of $S_{SNF}(E, t)$ used in this work comes from P. Jaffke et al.[121]. An estimated antineutrino spectrum was calculated based on public irradiation history for the four oldest cores: D1, D2, L1, and L2. It provides antineutrino spectra in ν/MeV for 1/3rd of the core's fuel assemblies in 0.05 MeV intervals for times, t_i , ranging from 1 day after core shutdown and 2000 days after shutdown.

The total antineutrino spectrum from each pool at a given time is estimated as:

$$S_{SNF_{pool}}(E, t) = \begin{cases} \sum_{n=0}^N S(E, t' + nT) & : W_{th}(t) > 0 \\ 3 \times S(E, t') + \sum_{n=1}^N S(E, t' + nT) & : W_{th}(t) = 0 \end{cases} \quad (4.10)$$

where t is a day during the data period, t' is the age of the youngest batch of spent fuel (estimated as the number of days since the most recent shutdown started), T is the nominal length of a fuel cycle, and N is the number of batches of fuel assumed to be cooling in the pool. The multiplicative factor is applied to the most recent batch of spent fuel when the core is shut down to account for the “effective SNF.” Given the 18 month and 12 month fuel cycle lengths and the assumption that there are five years worth of cooling fuel assemblies in each pool, T (N) is 540 days (3) for the D1 and D2 cores and 360 days (4) for the L1 and L2 cores. For the recently built cores, L3 and L4, $T = 360$ and $N = 1$ or 0, respectively. We note here that the newest cores have not had three fuel cycles yet, leading to potential inaccuracy in the assumption that any spent fuel has been removed from these cores. Likewise, there is not public information on the irradiation histories yet, so the spectrum is assumed to match the L1 calculation of [121]. The nominal spent fuel flux and ages of the most recently removed fuel are shown in Figure 4.11. Core shutdowns can be noted in the upper portion of the figure: L2 shut down prior to data taking and turned back on in early January 2012, beginning its 10th fuel cycle. L1 was down from approximately the third week of January until the second week of February 2012, when it began its 11th fuel cycle. D1 shut down from approximately the beginning of April 2012 until the beginning of June 2012, at which point it started its 16th fuel cycle. L4 had its first shutdown from mid May through mid July 2012, when it started its 2nd fuel cycle.

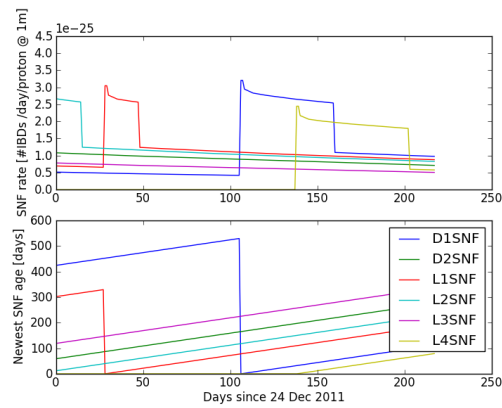


Figure 4.11 The estimated antineutrino flux from the spent fuel pool corresponding to the most-recently-removed fuel assemblies for each of the six reactor cores (top). Increases correspond to core shutdowns, for which fuel remaining in the core is treated as “effective” SNF. The approximate age of the most-recently-removed fuel assemblies calculated as days since the beginning of each core’s last shutdown (bottom).

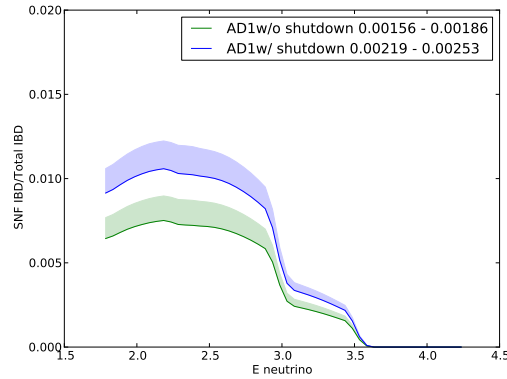


Figure 4.12 Total predicted SNF events over the data period corresponding to this analysis (left). Fraction of total expected IBD events ($/0.05$ MeV) attributed to SNF at AD1 illustrating the impact of in-core decays during reactor shutdown periods (right).

When calculating the expected IBD spectrum for the entire data period, Eq. 4.10 must be integrated over time. The $S_{SNF}(E, t)$ are interpolated between the calculated time points using two methods. By default, a low estimate is calculated by treating the spectrum between t_i and t_{i+1} as a constant, $S(E, t_{i+1})$. An upper bound is calculated based on linear interpolation between time points for each energy bin.

4.6.1 Estimated Magnitudes of SNF Contributions

The nominal expectation of the spent fuel contribution to the IBD rates includes treatment of the estimated amount of fuel sitting in the pools and an assumption that the overall flux is approximately tripled when cores are shut down. This is because the fuel that remains in the core (estimated as $2/3$ of the total assemblies) are also decaying during this time. The additional antineutrinos from the fuel remaining in the cores during shutdowns are treated as “effective SNF.” In all plots, bands indicate a prediction range due to approximations made in integrating the time evolution of the SNF spectrum as discussed above. Figure 4.12 shows the fraction of the IBD spectrum attributable to SNF where the “effective SNF” has been either included or ignored. We estimate that the “effective SNF” accounts for a roughly 40% increase in the nominal SNF-induced IBD events compared to ignoring it. Figure 4.13 indicates a similar increase from including previously

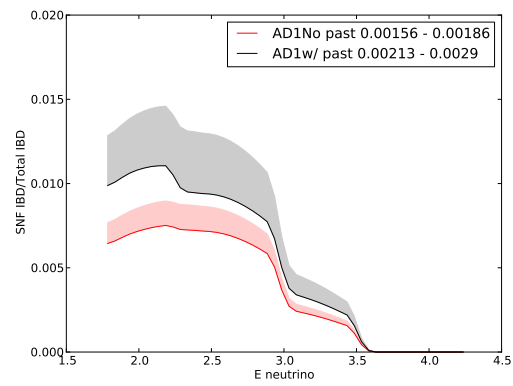


Figure 4.13 Total predicted SNF events over the data period corresponding to this analysis (left). Fraction of total expected IBD events (/0.05 MeV) attributed to SNF at AD1 illustrating the impact of previously unloaded fuel on the prediction (right).

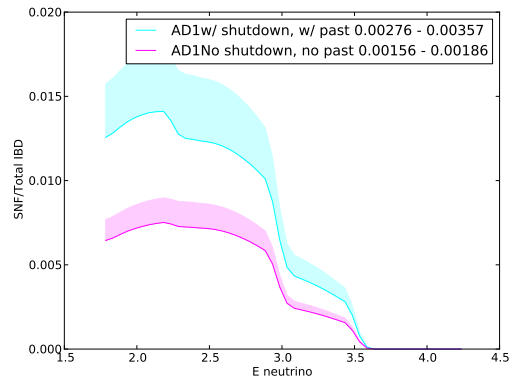


Figure 4.14 Total predicted SNF events over the data period corresponding to this analysis (left). Fraction of total expected IBD events ($/0.05$ MeV) attributed to SNF at AD1. Cyan corresponds to the nominal SNF prediction used (right).

unloaded fuel in the calculation compared to ignoring it. Figure 4.14 illustrates that including both the “effective SNF” and the contributions from previously unloaded fuel batches gives a roughly 100% increase in the spent fuel contribution to the overall IBD rate compared to ignoring them in the six-AD data period.

4.6.2 Correlations Between Bins and Detectors

The shape of the SNF-induced IBD spectrum is largely consistent between various calculations of the time evolution of the decaying fuel[122, 120, 121]. However, uncertainties about the quantities of fuel in each pool suggest that the SNF normalization may vary independently between pools. Thus, toy spectra for the spent fuel prediction are generated assuming correlation between energy bins but independence between different pools. A set of six random, Gaussianly distributed parameters, δ_{pool} , ($\mu = 0$, $\sigma = 1$) are generated. The toy predicted spectra are computed by scaling all bins of the spent fuel contribution at a given pool by $(1 + \delta_{pool}\sigma_{SNF,pool}(e))$. The resulting fractional uncertainties at each AD and correlations between energy bins in all ADs are shown in Figure 4.15.

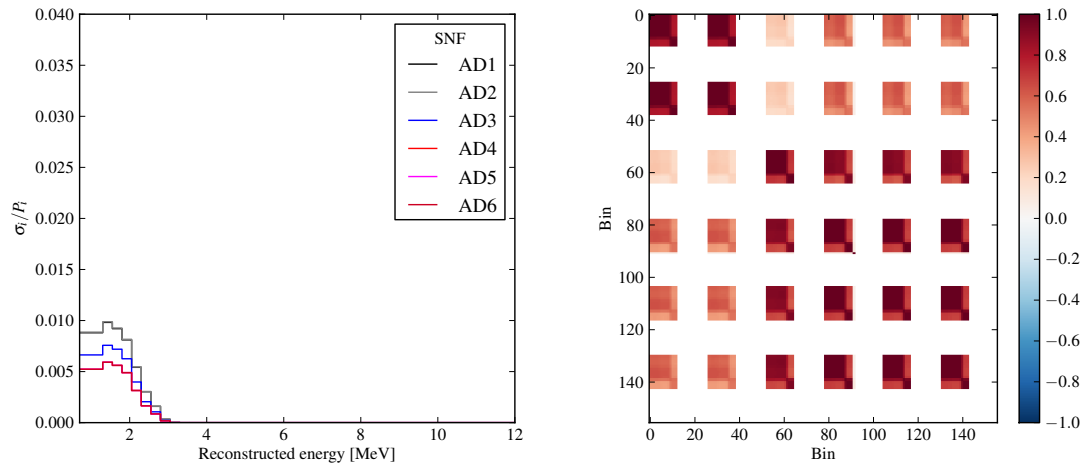


Figure 4.15 Fractional uncertainties at each AD from SNF (left) and the associated correlation matrix (right).

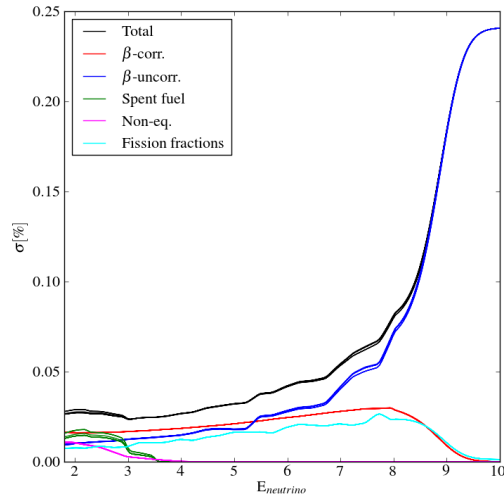


Figure 4.16 Fractional uncertainty in the IBD spectrum for each component of the reactor prediction that causes variations in the spectrum shape. ^{238}U uncertainties are treated as uncorrelated between energy bins and are included with uncorrelated β conversion uncertainty. Uncertainties are shown as a function of neutrino energy before adjustments for detector response.

4.7 Final Nominal Prediction and Uncertainties

For each flux model, the final predicted spectrum is initially determined in terms of true-neutrino energy at each detector. The DAQ livetime of the detectors is included. A nominal oscillation effect including both $\sin^2 2\theta_{13}$ and $\sin^2 2\theta_{12}$ is also included. The fractional uncertainties for each detector from each component of the prediction are shown in Figure 4.17. In this case, the ^{238}U uncertainties have been treated as uncorrelated between energy bins and are included with the uncorrelated β conversion uncertainties. The nominal expected spent fuel differs slightly between detectors due to the differing shutdown times between the Daya Bay and Ling Ao cores. Table 4.3 summarizes assumptions made about correlations for each reactor effect when predicting the IBD spectrum and its uncertainties. The final correlation matrix for the combined reactor spectrum uncertainties including all energy bins and ADs is shown in Figure 4.17. Finally, Table 4.4 provides the expected IBD rate variations for ADs in each of the three experimental halls.

Effect	Reactors	Isotopes	Bins
Fission fractions	Y	Y(p)	-
$\beta \rightarrow \bar{\nu}$ conversion (cor.)	Y	Y	Y
$\beta \rightarrow \bar{\nu}$ conversion (uncor.)	Y	N	N
U-238	Y	-	N(Y)
Non-equilibrium	N	N	Y
Spent fuel	N	-	Y
E/fission	-	Y	-
Core power	N	-	-

Table 4.3 Summary of correlations in various prediction components. The energy released per fission and power uncertainties are not considered in detail in this work as they have negligible impact on spectral uncertainties.

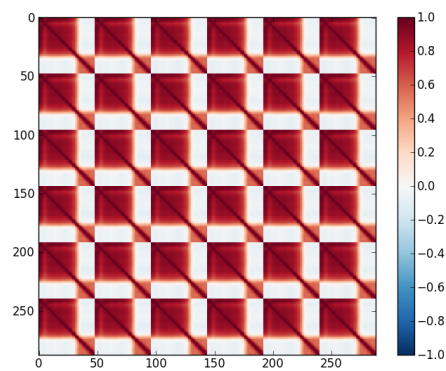


Figure 4.17 Correlations between 0.25 MeV bins due to the combination of reactor component uncertainties.

Rate uncertainty by effect	EH1 [%]	EH2 [%]	EH3[%]
Fission fraction (5%)	0.62	0.68	0.67
Non-equilibrium	0.15	0.15	0.15
Spent Fuel	0.28	0.25	0.23
β Conversion (corr.)	1.96	1.96	1.96
β Conversion (uncorr.)	0.20	0.21	0.21
^{238}U (E-corr.)	1.48	1.51	1.51
^{238}U (E-uncorr.)	0.1	0.1	0.1
Total (^{238}U corr.)	2.6	2.6	2.6
Total (^{238}U uncorr.)	2.1	2.1	2.1

Table 4.4 Percent uncertainties on the measured IBD rate at a single Daya Bay detector from each input uncertainty in the reactor calculation.

Chapter 5

Analysis

This chapter describes the oscillation fit results under each flux model and the relative agreement between the flux models and the data. Section 5.1 gives an overview of the data set used for the analysis. Section 5.2 describes the nominal prediction of the data. Section 5.3 describes the oscillation method used to produce the best-fit prediction given the data. The oscillation analysis is consistent with that used in [69]. Section 5.4 analyzes the agreement between the nominal predictions and the data.

5.1 Data Set

The data used was taken with six antineutrino detectors (ADs) over 217 days between December 24, 2011 and July 28, 2012. The oscillation analysis was blinded by incorporating nominal detector target masses and assuming reactor operation at full power with constant fuel composition. The dataset, selection algorithms, and response models are the same as those used in [69]. Summaries of the dataset, efficiencies, and detector response model and uncertainties are given in Chapter 3. The coincident inverse beta decay (IBD) signal candidates are selected after removing “flashing” PMTs from the single event data. Remaining events are grouped into coincidence pairs and kept if the prompt and delayed components satisfy energy and timing selection criteria corresponding to neutron captures on Gd. The prompt (delayed) portion of the event must have $0.7 < E_{rec} < 12$ MeV ($6.0 < E_{rec} < 12$ MeV) and the time between the events must satisfy $1 < \Delta t < 200$ μ s. Additionally, a multiplicity cut is applied to remove ambiguous cases where additional events in the detector occur in temporal proximity to an IBD candidate. Coincidences

are rejected if there are multiple prompt-like events in the 400 μs window before the delayed candidate. Likewise, they are rejected if there are any additional delayed-like event in a 200 μs window after the delayed candidate. IBD candidates are also rejected if they occur in various time windows following muons. The muon cut criteria depend on the energy of the muon and which experimental system(s) identify it. For muons that pass through the water pools and hit more than 12 PMTs in the IWS and OWS, IBD candidates are rejected when the delayed candidate is between -2 μs to 600 μs from the water pool trigger. For muons passing through ADs, the vetoed time window around the delayed candidate is -2 to 1400 μs when the total AD light yield is > 3000 p.e. or -2 μs to 0.4 s if the total AD light yield is $> 300,000$ p.e.

Consistent with the analysis of [69], the prompt data spectrum is binned from 0.7 MeV to 12 MeV in reconstructed energy. Bins have 0.25 MeV width, with the exception of the low and high bins, which go from 0.7 to 1.3 MeV and 7.3 to 12 MeV, respectively.

5.2 Nominal Model of the Inverse Beta Decay Spectra

The expected IBD signal in an AD from a single core is:

$$\frac{dN^2}{dE dt}_{IBD}(E, t) = \frac{N_p(t)}{4\pi L^2} P(\theta_{13}, \Delta m_{ee}^2, L, E) \epsilon(E, t) \sigma_{IBD}(E) \times \left(\sum_i \left(\frac{W_{th}(t)}{\sum_i f_i(t) e_i} \times f_i(t) \times S_i(E) \times c_{non-eq,i}(E, t) \right) + S_{SNF,i}(E, t) \right) \quad (5.1)$$

The terms in Equation 5.1 are the number of target protons N_p , the baseline L , a general detection efficiency ϵ , the IBD cross section σ_{IBD} , the thermal power of the core W_{th} , the fraction of fissions from each isotope f_i , the thermal energy released per fission for each isotope e_i , the antineutrinos produced per fission of each isotope S_i , a correction to the neutrino production spectrum from non-equilibrium effects $c_{non-eq,i}$, and the spent fuel spectrum S_{SNF} . Additionally, $P(\theta_{13}, \Delta m_{ee}^2, L, E)$ is the oscillation probability due to $\sin^2 2\theta_{13}$ and the mass-splitting Δm_{ee}^2 . To get a predicted neutrino spectrum for an arbitrary data period Equation 5.1 is integrated over time. In the final analysis, the reactor components of Equation 5.1 are taken from the weekly average values. The spent fuel contribution, S_{SNF} , is calculated based on the shape given in [122], normalized to contribute at a 0.3% level to the overall IBD rate. The non-equilibrium corrections c_{non-eq}

are applied from the 450 d calculation in [81]. For the six-AD data period, these yield consistent results with the time-dependent calculations described in Chapter 4.

The evaluation of the uncertainties and correlations on reactor-based components is described in Chapter 4. Reactor predictions are made with both the original beta spectra conversions from ILL [72, 73] and with the updated conversion by Huber[19]. For consistency, the ILL spectra is combined with a contemporaneous theoretical prediction of ^{238}U [88]. The Huber prediction is combined with the ^{238}U calculation from [81].

5.2.1 The Nominal Prediction of the Data

The nominal prediction of the data starts with the reactor prediction above. Oscillation parameters except $\sin^2 2\theta_{13}$ are included in the nominal model based on their values from the 2012 PDG[16]. For $\sin^2 2\theta_{13}$, the value determined in Daya Bay's previous rate-only result[68], 0.089, is used.

Equation 5.1 gives the expected IBD signal spectrum in terms of true neutrino energy. However, data is reduced in reconstructed positron energy. To reach a point for comparison, the prediction based on reactor information and corrections are converted into the reconstructed energy. The effects of reconstruction are applied in logical physical order. First the neutrino energy is converted to the true prompt energy, accounting for the difference between the incoming neutrino energy and the kinematic energy transferred to the positron and the 1.022 MeV of mass energy deposited when the positron annihilates with an electron in the detector[91]. The resulting spectrum is smeared by a matrix representing energy loss from non-scintillating volumes, namely the inner acrylic vessel[107]. The spectrum in visible energy is shifted to account for the combination of scintillator and electronics energy nonlinearity[109] and smeared to account for the energy resolution. Summaries of the IAV correction and the nonlinearity models can be found in Chapter 3. For the nominal prediction, these effects are applied based on their expected central values. After the prediction has been converted to nominal reconstructed energy, expected backgrounds can be added to give the total predicted prompt spectrum.

5.3 The Oscillation Results

The same rate+shape fit that was used for the result[69, 123] is used to produce a best-fit spectrum to match the data and extract oscillation parameters for each reactor model. The χ^2 expression used by the fitter is:

$$\chi^2 = \sum_{adi=1}^{adi=6} 2(X_{adi} - M_{adi} + M_{adi} \ln(\frac{M_{adi}}{X_{adi}})) + \sum_{adi=1}^{adi=6} \sum_{ei=1}^{ei=26} M_{adi,ei} \ln \frac{M_{adi,ei}}{X_{adi,ei}} + \chi_{penalties}^2 \quad (5.2)$$

where $X_{adi,ei}$ is the expected count in the ei^{th} bin of the adi^{th} detector and $M_{adi,ei}$ denotes the measured count in the same bin. When fitting the data, the minimizer adjusts the prediction constrained by uncertainties on each component of the overall model. Gaussian penalty terms, $\chi_{penalty}^2$ are used to constrain elements of the prediction (reactor, detector, background, etc.) within their uncertainties by increasing the χ^2 as the parameters are pulled away from their nominal values[123]. The penalties are summarized below:

$$\chi_{penalties}^2 = \delta_{\mathbf{r}}^T \mathbf{V}_{\mathbf{r}}^{-1} \delta_{\mathbf{r}} + \sum_{adi=1}^{adi=6} \left(\frac{\delta_{adi}^{AD}}{\sigma_{adi}^{AD}} \right)^2 + \sum_{adi=1}^{adi=6} \left(\frac{\delta_{adi}^{bg}}{\sigma_{adi}^{bg}} \right)^2 + \sum_{j=0}^{j=4} \left(\frac{\delta_j^{osc}}{\sigma_j^{osc}} \right)^2 \quad (5.3)$$

Effects originating with the reactor prediction are constrained using a covariance matrix, \mathbf{V} . Because of strong correlation between the reactor spectrum observed by ADs sitting in the same water pool, the matrix is composed of 26 bins in each of 3 halls-or 78×78 elements. These are generated by varying components of the reactor prediction at each hall in a similar manner to that described in Chapter 4. The reactor covariance matrix includes a combination of effects from the β conversion, ^{238}U calculation, and corrections from spent fuel and off-equilibrium decays. These effects contribute to uncertainties in both rate and shape. Thus the normalization produced by the oscillation fit is a biased measurement of the overall flux normalization.

The parameter δ^{AD} in Equation 5.3 includes nuisance parameters and uncertainties on components of the detector response. Six parameters govern the relative detection efficiency constrained by uncorrelated AD efficiency uncertainty $\sigma_{eff} = 0.168\%$. Six parameters govern the relative energy scale uncertainty constrained by $\sigma_{esc} = 0.35\%$. Four parameters govern the combination of possible positron nonlinearity models, each constrained by $\sigma_{NL} = 1$. The constraints on the

Parameter	New (Huber)	Old (ILL)
$\sin^2 2\theta_{13}$	0.090 ± 0.008	0.091 ± 0.007
Δm_{ee}^2 [eV ²]	$2.59 \pm 0.2 \times 10^{-3}$	$2.55 \pm 0.2 \times 10^{-3}$
χ^2 min/dof	163.2/153	162.6/153

Table 5.1 Best-fit oscillation results when starting from the new and old reactor models. Uncertainties listed on the oscillation parameters are directly from the fitter. They closely match the values obtained in a scan of the parameter space around the minimum.

energy scale and nonlinearity are treated conservatively to enable the minimizer to remove possible AD-correlated fluctuations caused by phenomena other than oscillation without biasing the oscillation results.

The parameter δ^{bg} in Equation 5.3 includes the nuisance parameters on the five sources of background. Six parameters govern the accidental rates between detectors constrained by σ_{acc} , which are listed in Table 3.4. Three parameters govern the cosmogenic background rates at each hall, constrained by $\sigma_{cosmo} = 30\%$. One parameter governs the mixture of ⁹Li to ⁸He in all detectors, constrained by $\sigma_{cosmo,9li/8he} = 5\%$. One parameter governs the quenching of α s and neutrons, constrained by $\sigma_{cosmo,k_B} = 100\%$. Four parameters govern the nonlinearity of the electrons in all ADs, they are constrained by a covariance matrix. Three parameters govern the fast neutron rates at each hall, constrained by $\sigma_{fastn} = 50\%$. One parameter governs the rate of the ²⁴¹AmC source background in all detectors, constrained by $\sigma_{AmC} = 40\%$. One parameter allows a modification of the exponential ²⁴¹AmC background shape at all detectors, constrained by $\sigma_{AmC,shape} = 15\%$. Finally one parameter governs the C(α ,n) at all detectors, constrained by $\sigma_{\alpha,n} = 50\%$.

The parameter δ^{osc} in Equation 5.3 includes the nuisance parameters on the solar oscillation terms. The central values and uncertainties on these are taken from the PDG [16].

In the minimization, three parameters, governing overall (detector-correlated) normalization, θ_{13} and Δm_{32}^2 respectively, are allowed to vary freely without χ^2 penalties. The fit compares data to the prediction in 26 bins in each detector, giving a total of 156 data points. Thus there are 156 – 3 degrees of freedom. Resulting normalization, θ_{13} , Δm_{32}^2 , and χ^2 are given in Table 5.1.

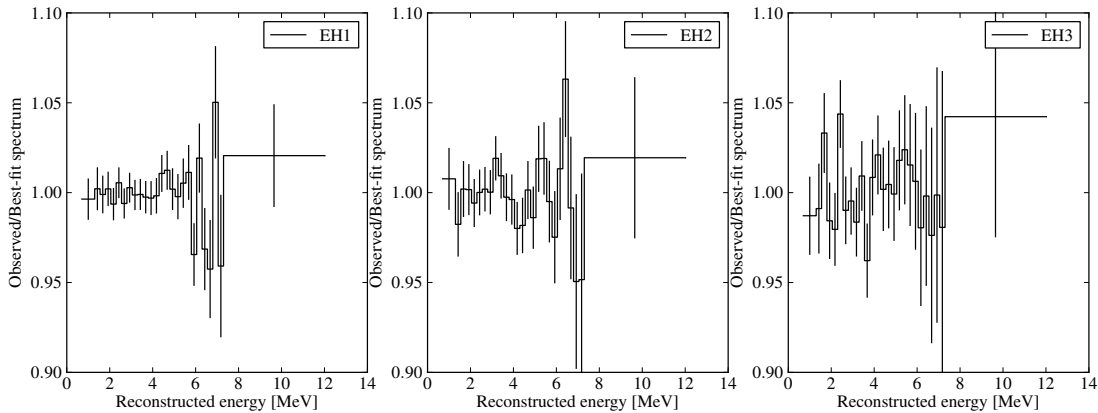


Figure 5.1 The ratio of data to best-fit spectrum in each hall. Error bars correspond to the statistical uncertainties on the data.

5.3.1 Discussion

Figure 5.1 shows the ratio of data to best-fit prediction at each hall with corresponding statistical uncertainties. ADs within each hall have been combined. These figures correspond to the difference between data and the best-fit oscillation line in Figure 2 of [69], except that backgrounds have been included in the best-fit prediction instead of subtracted from the data. The fitter succeeds in producing a best-fit model that is a statistically reasonable match to the data.

Most importantly, we note that the oscillation parameter results are consistent regardless of the initial flux model. The normalization varies between models, which is expected. Fitting the Huber model to the data produces a negative normalization and fitting to the ILL model produces a much smaller normalization. Note that the reactor model uncertainties in the rate+shape fit include effects that change both the AD-correlated rate and shape. This creates potential ambiguity between the role of the absolute reactor flux and the absolute detection efficiency in the final normalization. Therefore, the normalization returned from this fit should not be interpreted as the reactor flux normalization. However, the difference in normalizations obtained between the Huber and ILL models does generally match the size of the shift noted by Mueller et al.[81], so we infer that models have been implemented consistently.

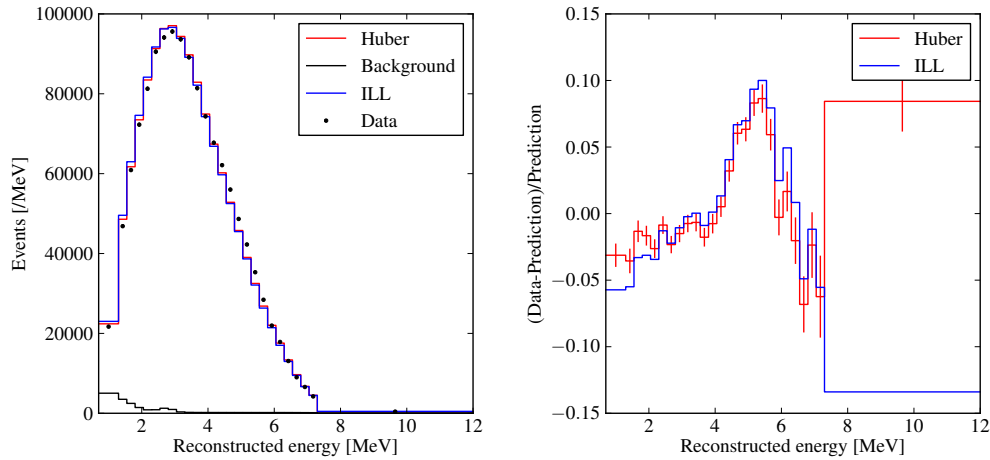


Figure 5.2 The expected total prompt spectrum for the six-AD data period based on the nominal ILL (blue) and Huber (red) flux models and nominal detector response (left). Each prediction has been normalized to the data and all ADs are combined. Measured prompt spectra are shown (black points) with statistical uncertainties. The right figure shows the fractional difference between the data and the prediction, with statistical errors added to the Huber model for reference.

5.4 Data Compared to Nominal Flux Models

Here, we check the difference between the nominal reactor model predictions and the observed spectrum. Figure 5.2 shows the ratio of data to the prediction including the best-fit oscillation parameters, but the nominal prediction model (nominal flux and detector response). There is a distortion in the ratio around 5 MeV when comparing the data and both models. Figure 5.3 reproduces the relative difference from Figure 5.2 for each individual AD, illustrating that the distortion is present in all detectors.

Using the prediction and data with all ADs combined, the prompt events in bins between 4.05 MeV and 6.05 MeV account for 24.5% of the nominal models' expected IBDs after normalizing the overall rate to match the data. This energy range accounts for 25.6% of the data. Thus the distortion can be attributed to roughly 1.1% of all events in the data. It will not affect rate-only oscillation results because, as shown in Figure 5.3, its magnitude is consistent between ADs.

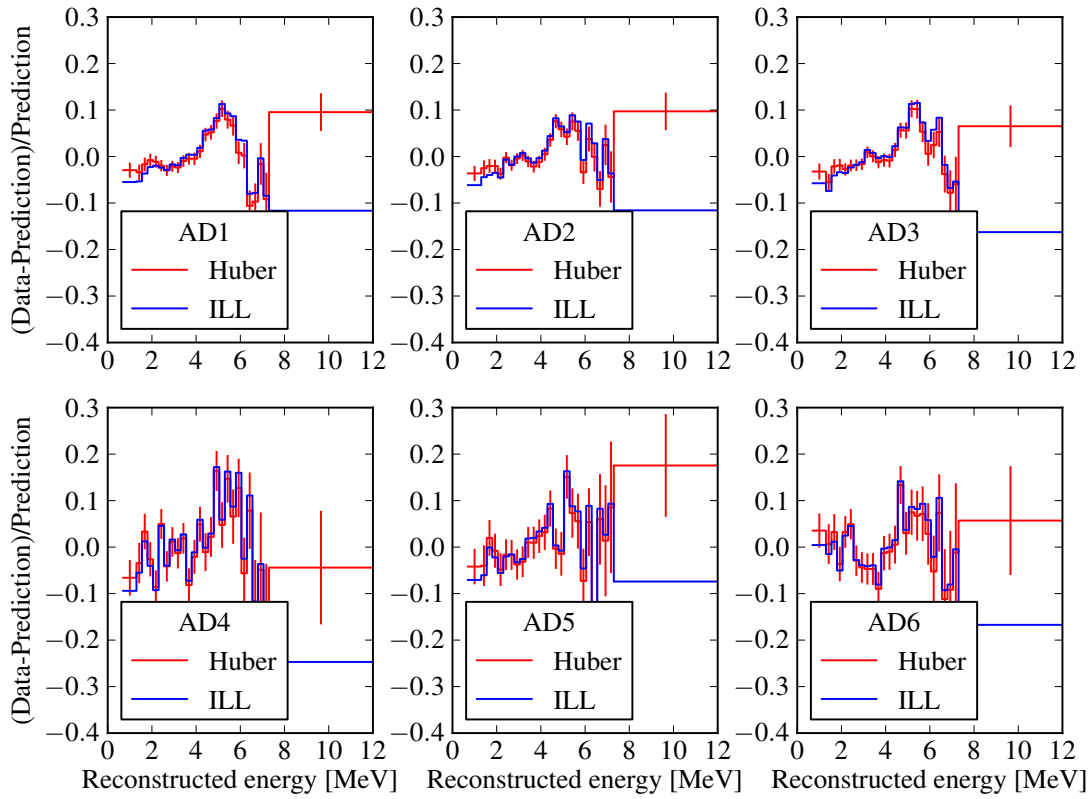


Figure 5.3 The fractional difference between nominal predictions and observed data for the Huber (red) and ILL (blue) models for individual ADs. Each predicted spectrum has been normalized to the data from the corresponding AD. Statistical errors are included on the Huber curve for reference.

To evaluate the consistency of the measured and predicted spectra given systematic uncertainties on the reactor (or detector response) model, we compute a χ^2 :

$$\chi^2 = \sum_i \sum_j (m_i - p_j) \mathbf{V}^{-1} (m_j - p_j) \quad (5.4)$$

where \mathbf{V} is a covariance matrix including all elements of the reactor model uncertainties, statistical uncertainties, and optionally also the positron nonlinearity. The calculation of elements of \mathbf{V} is described in the following section.

5.4.1 Covariance Matrices and Uncertainty Combination

Production of covariance matrices for each component in the reactor prediction was described in Chapter 4. Several components of the detector response can be considered similarly; of these, the positron nonlinearity is the dominant contribution. Here, we discuss the combination of uncertainties from individual effects to produce the combined covariance matrix.

Covariance matrix elements for each prediction component are determined from a toy Monte Carlo study. They are calculated using:

$$\mathbf{V}_{\text{effect},ij} = 1/N \sum_n (p'_{ni} - p_i) \times (p'_{nj} - p_j). \quad (5.5)$$

where \mathbf{p}'_n is the n^{th} varied prediction where **effect** has been modified, and \mathbf{p} is the binned prediction given the nominal central values of all effects. Binning in these predictions and matrices is initially at the 0.05 MeV level, giving initial 1440x1440 matrices and 1440 element prediction arrays (240 bins x 6 ADs). Bins in the new matrix can be expressed from a simple linear combination of bins in the initial matrices. The I new variables representing combined bins can be written in matrix form: $\mathbf{C}_{I \times j}$ [124]. The final covariance matrix is then:

$$V_{I,J} = \mathbf{C}^T \mathbf{V}_{\text{initial}} \mathbf{C} \quad (5.6)$$

Conveniently, the final analysis bins have edges corresponding to the edges of the initial bins. Thus elements \mathbf{C}_{Ij} will all be either zero or one depending on the specific combination of ADs and energy bins used. An example \mathbf{C} that converts initial calculation bins in each AD to final analysis bins in each hall is shown in Figure 5.4.

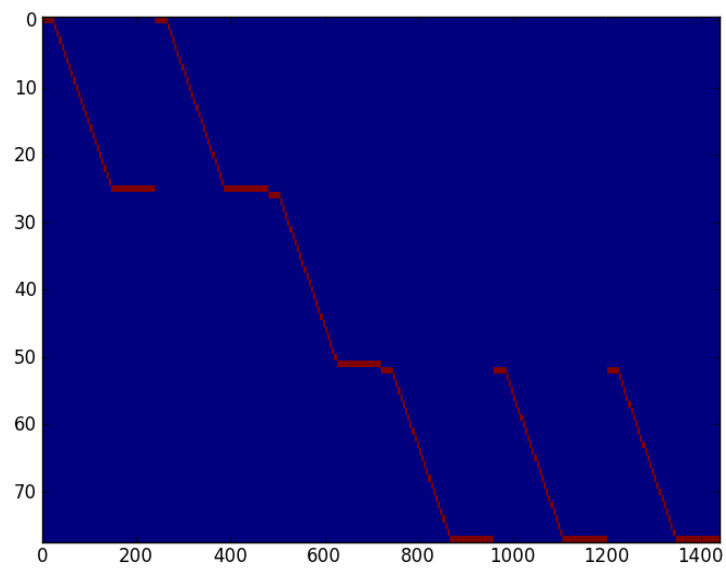


Figure 5.4 An example matrix, C , combining initial calculation bins for six ADs into final analysis bins for three halls.

Reactor model	R_{norm}	χ^2_{stats}	$\chi^2_{stats+reactor}$	$\chi^2_{stats+reactor+nonlin}$
Huber	0.956	359.3/25	111.6/25	65.5/25
ILL	1.000	561.9/25	128.3/25	39.5/25

Table 5.2 The χ^2/dof for the comparison of expected and observed spectra after normalizing each predicted spectrum to the data. The observed spectrum does not match either reactor model.

To get the final combined \mathbf{V} needed for Eq. 5.4, the individual covariance matrices from each prediction component ($\mathbf{V}_{\text{conversion,correlated}}$, $\mathbf{V}_{\text{conversion,uncorrelated}}$, $\mathbf{V}_{\text{U-238}}$, $\mathbf{V}_{\text{Noneq}}$, \mathbf{V}_{SNF} , $\mathbf{V}_{\text{fission fraction}}$, and potentially $\mathbf{V}_{\text{nonlinearity}}$) and the statistical uncertainties on the data (\mathbf{V}_m) must be combined. This is done by performing an element-wise sum for each individual matrix. The prediction covariance matrix elements are multiplied by a ratio, r , to normalize the prediction to match the data.

The final covariance matrix is:

$$\mathbf{V} = \mathbf{V}_m + r\mathbf{V}_p \quad (5.7)$$

The final covariance matrices including all reactor model components with a shape-dependence and the nonlinearity are shown in Figure 5.5. When comparing to the best-fit, uncorrelated uncertainties are included on the diagonal elements of \mathbf{V} based on the expected number of events in the best-fit. This will be similar to the statistics on the data that was used to produce the best-fit.

5.4.2 Results

With the final covariance matrix containing all reactor model uncertainties, the predicted spectrum can be compared to the observed data. Table 5.2 gives the χ^2 difference between the observed and expected spectra based on statistical, statistical+reactor, and statistical+reactor+positron nonlinearity uncertainties. Figure 5.6 shows the difference between the observed and nominally predicted spectrum where error bands are drawn from the diagonal elements of the prediction covariance matrix. For the Huber model, the contributions of individual bins to the overall χ^2 are shown in Figure 5.7. The bins surrounding 5 MeV are responsible for the majority of the χ^2 .

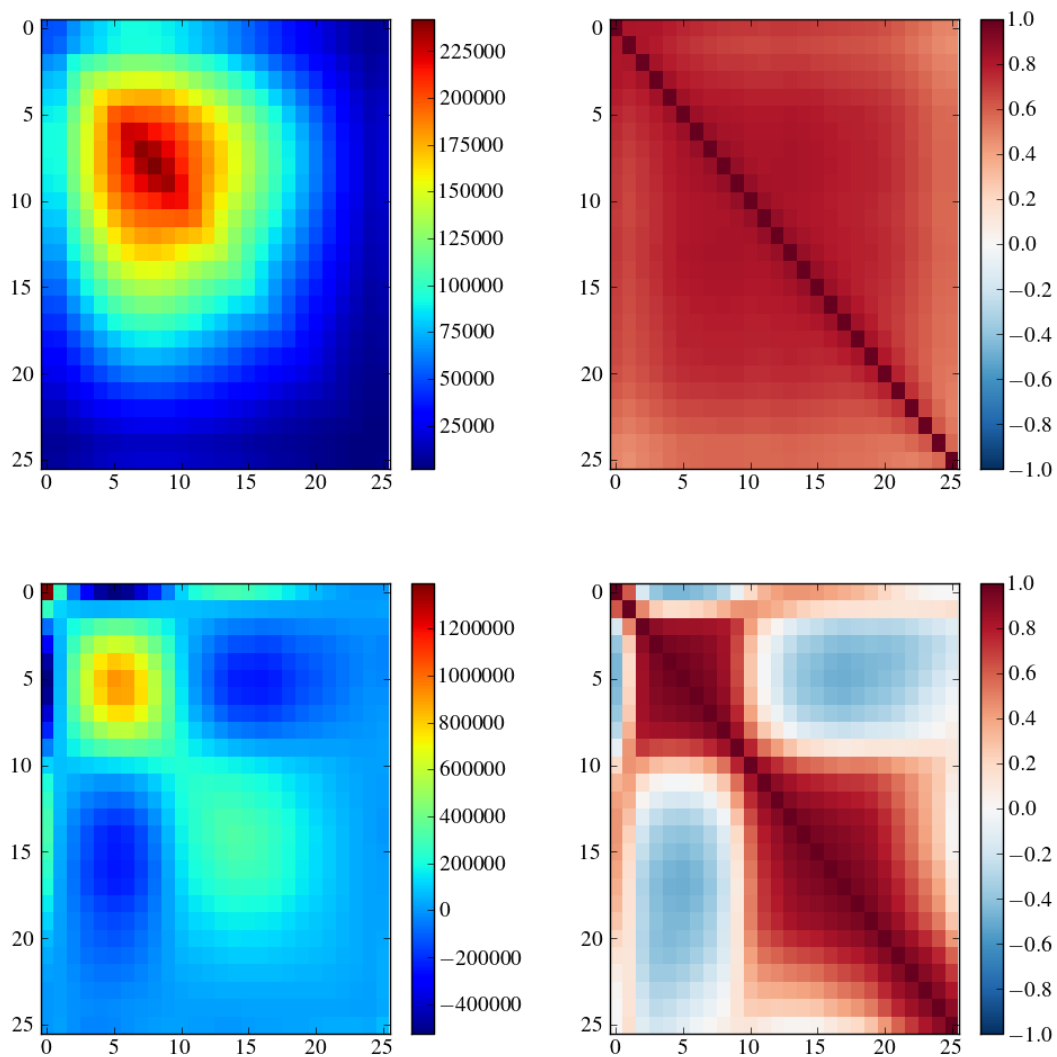


Figure 5.5 For the Huber reactor fluxes, the covariance (top left) and correlation (top right) matrices corresponding to the nominal reactor model. The lower figures show the covariance (left) and correlation (right) matrices with the conservative detector nonlinearity uncertainty also included.

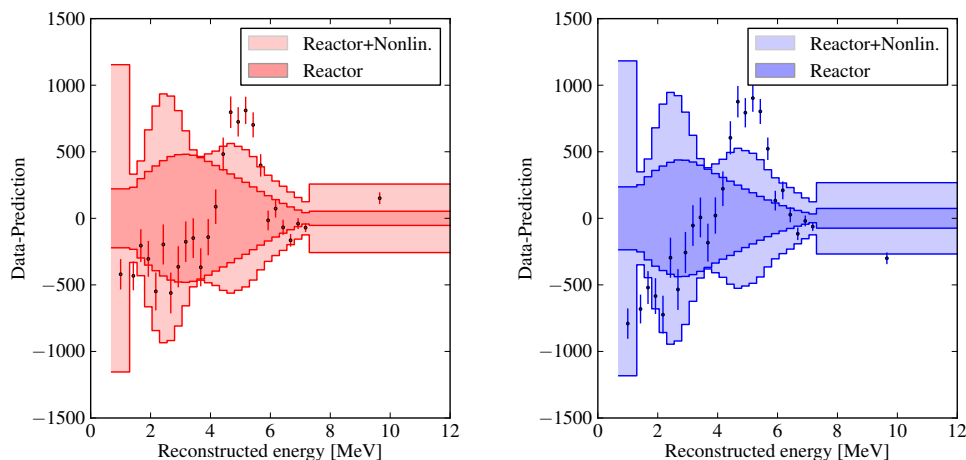


Figure 5.6 The difference between observed and expected events compared to the Huber (left) and ILL (right) reactor models and detector nonlinearity uncertainties. In each case, the predicted spectrum and prediction covariance matrix have been normalized to match the total number of observed events. Error bars represent the statistical uncertainty of the data with all ADs combined. The inner error bands are from the diagonal elements of the reactor prediction covariance matrix. The outer error bands are from the diagonal elements of the prediction covariance matrix where the positron nonlinearity uncertainty is also included.

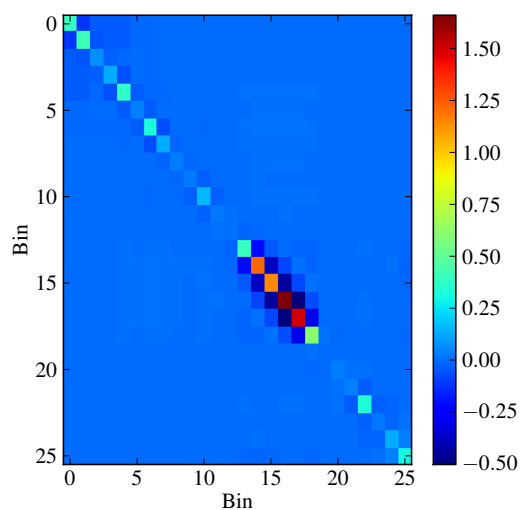


Figure 5.7 The contribution to the overall χ^2 from each analysis bin.

The measured IBD spectrum is not consistent with either reactor model given uncertainties suggested by [19], [81], [72, 73] and [88]. It is only marginally more compatible when uncertainties from the positron nonlinearity model are included at the conservative level used for Daya Bay's oscillation analysis. With the conservative detector response, only 3.3% of experiments would produce a disagreement of at least the observed level from a true ILL reactor spectrum. A less conservative treatment of the nonlinearity would be expected to reduce it to below the level below the reactor model uncertainties, leading to considerably larger χ^2 s in the case of both models. Therefore, we conclude that neither reactor model is sufficient to describe the measured spectrum due to the excess around 5 MeV.

5.4.3 Discussion

Preliminary investigations have been made of potential causes of the discrepancy. The fact that the 5 MeV excess is seen by all detectors suggests that it is probably not related to muon-induced backgrounds as the muon rates differ between sites. This restricts possibilities to either currently unhandled detector response features, correlated detector backgrounds, or reactor antineutrino production. Subsequent paragraphs present the possible causes and plausibility for each of these possibilities.

Detector Response When producing the oscillation results, a conservative treatment of the absolute detector response is employed. This provides Minuit with room to remove features of the spectrum that are correlated between detectors. Because rate+shape oscillation results are based on a spectral distortion that varies with the core-AD distance, obtained values of $\sin^2 2\theta_{13}$ and Δm_{ee}^2 and their uncertainties will not be biased in this treatment. The conservative model of detector response relies on forming five separate models of the conversion between true prompt event energy and the expected reconstructed energy. The nominal detector response model has been shown to reproduce the cosmogenic ^{12}B background spectrum accurately. The best-fit nonlinearity obtained in the oscillation fit causes tension in the fit to the cosmogenic ^{12}B spectrum[125]. Cross-checks of the nominal nonlinearity model against β spectra from ^{208}Tl , ^{212}Bi , and ^{212}Bi backgrounds are

found to be consistent within theoretical uncertainties on the shapes of those spectra, though endpoint energies of these are not high enough to address the 5 MeV region directly. This suggests that the detector model is not responsible for the distortion.

Neutrino Backgrounds The events in the region of the excess have been compared in terms of spatial, time, and energy distribution with IBD candidates in other energy regions and found consistent with the rest of the IBD signal[126]. There is no anomalous distribution of IBDs are uniformly distributed between the top and bottom of the detectors. Likewise, the neutron capture times and distances are comparable to those of IBD candidates in other energy regions. Energy and timing distribution of events occurring in the time window around the 5 MeV region are also consistent with those in other energy regions. Additional interactions between the neutrinos and nuclei in the detector could potentially play a role. Possible coincident neutrino backgrounds caused by neutrino-induced neutron emission from atoms in the ADs have also been preliminarily considered. In this case, the interactions would need to cause neutron emission from atoms in the detector in order to match the coincident data. Potential atoms in the target region of the detector, deuterium, ^{13}C , and ^{17}O have suitable energy thresholds for CC or NC-induced neutron emission[126]. Of these, the deuterium cross section is known to be too low to explain the excess.

Reactor Antineutrino Production Prompt spectra shown by other reactor experiments suggest that the excess is not unique to Daya Bay. Results shown recently by the RENO Collaboration[127] show that their Monte Carlo prediction clearly underestimates their data the 5 MeV region. Double Chooz's published prompt spectrum appears to show downward fluctuations around 4 MeV and 6 MeV, which may also indicate a similar feature in their data[61]. Less recently, Palo Verde's final results include a spectrum where two bins around 5 MeV that have higher rates than their prediction[79]. Likewise, the CHOOZ experiment also had a pair of bins around 5 MeV with upward fluctuations of roughly 1.12 and differ from their expectation by slightly more than 1σ [52] (reproduced in Figure 2.1). Notably, the Bugey-3 comparison between the ILL model and their data does not have an excess. However, Bugey-3's ILL model included a ^{238}U calculation from Klapdor

and Metzinger[77], not the Vogel calculation[88] that has been used subsequently. Bugey-3 considered an alternative model consisting of Klapdor and Metzinger’s calculations for all isotopes, and found that it agreed poorly with their measured spectrum. Unfortunately, the ^{238}U and ^{241}Pu components are cited to a private communication[77], making it challenging to determine whether this accounts for the apparent agreement.

None of the uncertainties or effects that are considered in the current reactor models have sufficient magnitudes or shapes to cause to the 5 MeV excess. However, there has been recent criticism of assumptions that go into the conversion of beta to neutrino spectra[82]. Specifically, Hayes et al. point out that forbidden decays and their associated shape factors introduce larger uncertainties than have been previously used. However, under extreme assumptions about the shapes of the forbidden decays shown in [82], the changes introduced in the IBD spectrum are also largely linear in energy. It is not obvious that these would lead to a bump in the spectrum either.

Finally, it should be noted for future investigation that, in Daya Bay’s case, the power company includes information on both fast and thermal fissions in the cores. At present, neutrino predictions do not differentiate between these despite the slight neutron energy-dependence of the fission yields. Depending on where in its fuel cycle it is, somewhere between 20% (beginning) and 15% (end) of fissions come from fast neutron-induced fissions of isotopes other than ^{238}U . Looking at the differences in fission product yields for specific nuclides may reveal specific candidate beta branches that are over or under-represented in the ILL measurements compared to in a power reactor.

5.5 Conclusion

A relative rate+shape analysis of the six-AD data set produces a robust result for $\sin^2 2\theta_{13}$ and Δm_{ee}^2 that is consistent with the rate-only and shape-only results and with measurements from contemporary experiments[69, 61, 64]. The mass-splitting is consistent with that measured in the muon neutrino disappearance channel[128]. Reactor antineutrino spectra between ADs are very similar for the data period analyzed. Correlations in the reactor spectra between energy bins

and detectors are handled using covariance matrices. In the oscillation results, a conservative model for the correlated detector response is used. This enables the minimizer to compensate for spectral features that are identical between detectors without effecting the oscillation results. The oscillation results are consistent regardless of the initial reactor flux model used to predict the spectrum at each AD.

When comparing the observed spectrum to the nominal prediction it becomes obvious that there is a detector-correlated excess of approximately 10% in the 5 MeV region of the prompt spectrum. This excess accounts for around 1% of the measured IBD candidates. Investigation of the excess is ongoing, but no simple explanations have been found.

Uncertainties and corrections currently applied to the reactor antineutrino spectra from both ILL or Huber conversions do not have appropriate shapes or magnitudes to explain the excess. Corrections to the antineutrino spectra of fissioning isotopes, possible core simulation errors, and spent fuel neutrinos have been incorporated into the reactor models and corresponding uncertainties. Suggestions of similar distortions can be seen in the prompt spectra of the Double Chooz[61], RENO[127], Palo Verde[79], and CHOOZ[52] experiments. We note that these experiments have a common neutron capture target (Gadolinium), but should otherwise have largely uncorrelated detection uncertainties. In contrast to the results from Bugey-3[77], we conclude that reactor models based on the converted ILL spectra are not sufficient to explain our data.

Chapter 6

Conclusions

This work describes the prediction of the inverse beta decay (IBD) spectrum and its comparison to data from the Daya Bay Reactor Neutrino Experiment in the context of a relative rate and spectral shape-based oscillation analysis. The data used corresponds to the full 217-day, six-AD dataset from December 24, 2011 to July 28, 2012. The reactor spectrum at and correlations between each AD have been explicitly calculated accounting for the unique geometry of the Daya Bay site. Additionally, this work shows that the oscillation results for $\sin^2 2\theta_{13}$ and Δm_{ee}^2 are consistent irrespective of outstanding questions about the reactor antineutrino fluxes and spectra [49, 19]. Finally, the reactor prediction machinery is employed to evaluate the consistency of the observed data with the expected prompt spectrum. Around 5 MeV, an excess of measured events relative to predictions (approximately 10% at 5 MeV and accounting for 1% of the overall events) is found.

6.1 Reactor Prediction

Chapter 4, describes the information used to determine the expected IBD spectrum at each of the Daya Bay antineutrino detectors (ADs). The complete prediction includes input from the power company about the thermal power outputs and simulated fuel compositions of each reactor core. It is combined with calculations of the energy released per fission from [114] and expected antineutrino spectra based on converted β spectra measurements and calculations [72, 73, 88, 19, 81]. The typical procedure for predicting the rate at in a reactor neutrino experiment have relied on β measurements of ^{235}U , ^{239}Pu , and ^{241}Pu , made at ILL in the 1980s[72, 73]. The roughly 10% contribution to the antineutrino flux from ^{238}U has been based on theoretical calculations[88].

Expected $\bar{\nu}_e$ spectra are converted from the measured β spectra by decomposing the spectrum into a number of virtual β -branches and applying corrections for the differences in interactions between electrons and neutrinos with the decaying nucleus. In the 1990s the Bugey-3 experiment produced a high-statistics measurement of the reactor antineutrino spectrum and found it to be in agreement with the ILL converted spectra[77].

However, in preparation for the current generation of high-precision $\sin^2 2\theta_{13}$ measurements, the ILL conversion procedure and influence of nuclear data were revisited in hopes of improving the uncertainty in the reactor antineutrino flux uncertainties[81, 19]. This reanalysis turned up an apparent anomaly, in which the expected IBD rates shifted by around 5% leading to apparent disagreement between data and prediction, was found. The difference between measured and expected cross-sections/fission, $\sigma_{IBD,meas.}/\sigma_{IBD,exp.}$, from past experiments shifted to 0.943 ± 0.023 [49]. Additionally, the updated calculations of the antineutrino spectra caused an increase in the expected antineutrino spectra at high energies[19].

Daya Bay's reactor spectrum has been predicted using both models. The new, Huber, model is based upon predicted antineutrino spectra from[19], with the ^{238}U calculation of [81]. The old, ILL, model is based upon the original conversion of[72, 73], with the ^{238}U calculation of [88]. In both cases, corrections are made to account for the off-equilibrium antineutrino flux[81, 120] and the contribution of antineutrinos originating in the spent fuel[122, 121, 120].

6.2 Reactor Antineutrino Spectrum Role in Oscillation Results

Regardless of the underlying reactor model, it is important to account for potentially incomplete correlations in the antineutrino spectra observed in Daya Bay's ADs. The suggestion of[83] is that uncertainties on $\sin^2 2\theta_{13}$ can be reduced to below the absolute uncertainties on both the reactor antineutrino spectrum and detector response by comparing relative event rates (or correspondingly spectra) between identical detectors at varying distances from the source. The Guangdong Nuclear Power complex has 17.4 GW_{th} of reactors, making it a good candidate site from a statistical perspective. However, the geographical distribution of cores along with their time-varying and potentially non-identical fuel composition and Daya Bay's use of multiple near sites complicate

the cancellation of reactor uncertainties between detectors. Thus it is important to demonstrate the level of correlation between expected spectra at the different sites. Along with the description of the prediction central values, Chapter 4 uses a toy Monte Carlo to produce a properly-correlated reactor model uncertainty covariance matrix for the Daya Bay detectors.

In Chapter 5, the spectral oscillation analysis in [69] is repeated with both updated and old reactor models. The reactor model based on the ILL model gives results $\sin^2 2\theta_{13}=0.091 \pm 0.007$, $\Delta m_{ee}^2 = 2.55 \pm 0.02 \times 10^{-3}$, and $\chi_{min}^2 = 162.6/153dof$. The updated model based on Huber conversions gives results $\sin^2 2\theta_{13}=0.090 \pm 0.008$, $\Delta m_{ee}^2 = 2.59 \pm 0.02 \times 10^{-3}$, and $\chi_{min}^2 = 163.2/153dof$. The uncertainties listed here for each model are from the fitter estimate; they differ from the uncertainties obtained from 1σ C.L. contours by no more than 0.001. As expected from the similar correlations arising from either reactor prediction, the oscillation results are consistent regardless of the model used.

6.3 Consistency of Nominal Reactor Predictions and Data

There is a spectral feature in the data around 5 MeV that is not accounted for by either reactor model. This feature is observed in the IBD data of all six detectors. The disagreement reaches 10% in bins around 5 MeV and represents approximately 1% of observed events. The probability that the observed spectrum would arise by chance given the uncertainties on current reactor models is negligible. Combining the detector nonlinearity model uncertainties as they applied to the oscillation analysis leads to only marginal agreement. Moreover, the uncertainties on the detector response model used in [69] are conservative and are expected to improve relative to the reactor model uncertainties. This seems to indicate a previously unaccounted feature in the reactor spectrum. Preliminary checks of the excess against a monoenergetic gamma, the simple addition of a beta branch, and possible neutrino interaction with atoms in the detector leading to neutron emission have not yet produced an explanation[126]. It does appear that other reactor experiments have a similar feature in their positron spectra[127, 61, 52, 79], suggesting that it is not unique to the Daya Bay detectors.

6.3.1 Impact of new U-238 Measurement

The calculated ^{238}U spectra of [81] and [88] were used in this work. Recently, N. Haag et al.[117, 116] measured the ^{238}U β spectrum for the first time. This spectrum differs somewhat from the calculated one, but as the ^{238}U contribution is nearly identical at each detector, it will not effect the oscillation results. Haag notes that the conversion of the measured ^{238}U spectrum produces an expected neutrino spectrum that has a roughly 10% distortion compared to that from [81].

6.4 Future Prospects

In an operating power reactor, the majority of ^{235}U , ^{239}Pu , and ^{241}Pu fissions are induced by thermal neutrons. However, data provided from the NPP indicates that at Daya Bay, approximately 15-20% of total fissions are from fast (around 0.5 MeV) neutrons. The original β spectra measured at ILL, which are the basis for currently-used flux predictions, used a more purely thermal neutron flux to irradiate their Uranium and Plutonium foils. Slightly differing yields between the fast and thermal fissions of each isotope suggest that checks of particular nuclides contributions at energies above 4 MeV may be useful.

The Daya Bay Reactor Neutrino Experiment has been taking data with all eight detectors since October 2012. This will more than double the amount of data used for the oscillation parameter measurement, which is still dominated by statistical uncertainties in the current work. Projected precisions of each oscillation parameter with currently collected data are shown in Figure 6.1.

Near-future results are expected to improve the precision of the oscillation results and provide the absolute flux normalization, the measured Daya Bay neutrino spectrum, and further discussion of the spectral feature. Data-taking is expected to continue through 2017. Ultimately, the uncertainty on $\sin^2 2\theta_{13}$ is expected to improve to 0.003 (3%) and the mass-splitting uncertainty will concurrently improve to approximately $7 \times 10^{-5} \text{ eV}^2$ (2.5%)[129].

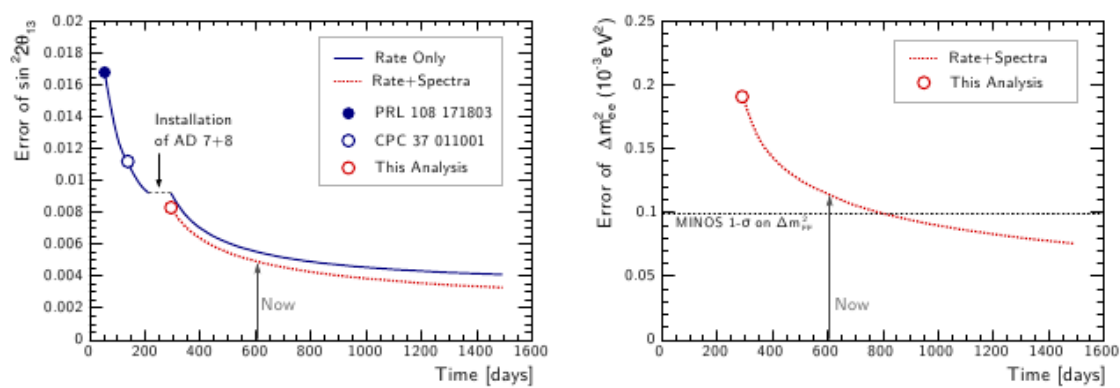


Figure 6.1 Measurement precision for this data set and projected sensitivity to the small mixing angle and mass splitting Δm_{ee}^2 including data from full eight detector running. From [129].

LIST OF REFERENCES

- [1] W. Pauli, Liebe radioaktiv damen und herren, (Dec. 1930).
URL <http://cdsweb.cern.ch/record/83282/files/>
- [2] E. Fermi, Versuch einer theorie der β -strahlen. I, Zeitschrift fuer Physik 88 (3-4) (1934) 161–177.
- [3] F. L. Wilson, Fermi's theory of beta decay, American Journal of Physics 36 (12) (1968) 1150.
URL <http://adsabs.harvard.edu/abs/1968AmJPh..36.1150W>
- [4] C. Cowan, F. Reines, F. Harrison, H. Kruse, A. McGuire, Detection of the Free Neutrino: A Confirmation, Science 124 (3212) (1956) 103–104.
URL <http://www.jstor.org/stable/1751492>
- [5] F. Reines, C. L. Cowan, Free antineutrino absorption cross section. I. measurement of the free antineutrino absorption cross section by protons, Physical Review 113 (1) (1959) 273.
URL <http://link.aps.org/doi/10.1103/PhysRev.113.273>
- [6] J. N. Bahcall, Solar Neutrinos. I. Theoretical, Physical Review Letters 12 (11) (1964) 300–302.
URL <http://link.aps.org/doi/10.1103/PhysRevLett.12.300>
- [7] R. Davis, Solar Neutrinos. II. Experimental, Physical Review Letters 12 (11) (1964) 303.
URL <http://link.aps.org/doi/10.1103/PhysRevLett.12.303>
- [8] D. Casper, et al., Measurement of Atmospheric Neutrino Composition with the IMB-3 Detector, Physical Review Letters 66 (20) (1991) 2561–2564.
URL <http://link.aps.org/doi/10.1103/PhysRevLett.66.2561>
- [9] Super-Kamiokande Collaboration, Evidence for Oscillation of Atmospheric Neutrinos, Physical Review Letters 81 (8) (1998) 1562–1567.
URL <http://link.aps.org/doi/10.1103/PhysRevLett.81.1562>

- [10] SNO Collaboration, Measurement of the Rate of $\nu_e + d \rightarrow p + p + e^-$ Interactions Produced by ^8B Solar Neutrinos at the Sudbury Neutrino Observatory, *Physical Review Letters* 87 (7) (2001) 071301.
URL <http://link.aps.org/doi/10.1103/PhysRevLett.87.071301>
- [11] KamLAND Collaboration, First Results from KamLAND: Evidence for Reactor Antineutrino Disappearance, *Physical Review Letters* 90 (2) (2003) 021802.
URL <http://link.aps.org/doi/10.1103/PhysRevLett.90.021802>
- [12] H. R. Band, et al., The Daya Bay antineutrino detector filling system and liquid mass measurement, *JINST* 8 (09) (2013) P09015.
URL <http://iopscience.iop.org/1748-0221/8/09/P09015>
- [13] S. L. Glashow, Partial-symmetries of weak interactions, *Nuclear Physics* 22 (4) (1961) 579–588.
- [14] S. Weinberg, A Model of Leptons, *Physical Review Letters* 19 (21) (1967) 1264–1266.
URL <http://link.aps.org/doi/10.1103/PhysRevLett.19.1264>
- [15] A. Salam, Weak and Electromagnetic Interactions, *Conf.Proc.* C680519 (1968) 367–377.
- [16] J. Beringer, Particle Data Group, Review of particle physics, *Physical Review D* 86 (1).
- [17] G. Gamow, E. Teller, Selection rules for the β -disintegration, *Physical Review* 49 (12) (1936) 895–899.
URL <http://link.aps.org/doi/10.1103/PhysRev.49.895>
- [18] C. Bertulani, *Nuclear Physics in a Nutshell*, Princeton University Press, 2007.
- [19] P. Huber, Determination of antineutrino spectra from nuclear reactors, *Physical Review C* 84 (2) (2011) 024617.
URL <http://link.aps.org/doi/10.1103/PhysRevC.84.024617>
- [20] D. Wilkinson, Evaluation of beta-decay: II. Finite mass and size effects, *Nucl. Instrum. Meth. A* 290 (23) (1990) 509–515.
URL <http://www.sciencedirect.com/science/article/pii/016890029090570V>
- [21] A. Sirlin, General properties of the electromagnetic corrections to the beta decay of a physical nucleon, *Physical Review* 164 (5) (1967) 1767–1775.
URL <http://link.aps.org/doi/10.1103/PhysRev.164.1767>
- [22] W. Bühring, The screening correction to the Fermi function of nuclear β -decay and its model dependence, *Nuclear Physics A* 430 (1) (1984) 1–20.
URL <http://www.sciencedirect.com/science/article/pii/0375947484901908>

- [23] P. Vogel, Analysis of the antineutrino capture on protons, *Physical Review D* 29 (9) (1984) 1918.
URL <http://link.aps.org/doi/10.1103/PhysRevD.29.1918>
- [24] B. Pontecorvo, Neutrino experiments and the question of leptonic-charge conservation, *Sov. Phys. JETP* 26 (1968) 984–988.
- [25] Z. Maki, M. Nakagawa, S. Sakata, Remarks on the unified model of elementary particles, *Progress of Theoretical Physics* 28 (5) (1962) 870–880.
URL <http://ptp.ipap.jp/link?PTP/28/870/>
- [26] L. Wolfenstein, Neutrino oscillations in matter, *Physical Review D* 17 (9) (1978) 2369.
URL <http://link.aps.org/doi/10.1103/PhysRevD.17.2369>
- [27] S. P. Mikheev, A. Y. Smirnov, Resonance enhancement of oscillations in matter and solar neutrino spectroscopy, *Sov. J. Nucl. Phys.* 42 (1985) 913–917.
- [28] R. Davis, D. S. Harmer, K. C. Hoffman, Search for Neutrinos from the Sun, *Physical Review Letters* 20 (21) (1968) 1205.
URL <http://link.aps.org/doi/10.1103/PhysRevLett.20.1205>
- [29] J. N. Bahcall, N. A. Bahcall, G. Shaviv, Present Status of the Theoretical Predictions for the Cl37 Solar-Neutrino Experiment, *Physical Review Letters* 20 (21) (1968) 1209.
URL <http://link.aps.org/doi/10.1103/PhysRevLett.20.1209>
- [30] SNO Collaboration, The Sudbury Neutrino Observatory, *Nucl. Instrum. Meth. A* 449 (1999) 172–207, [nucl-ex/9910016](http://arxiv.org/abs/nucl-ex/9910016).
URL <http://arxiv.org/abs/nucl-ex/9910016>
- [31] F. Reines, et al., Evidence for High-Energy Cosmic-Ray Neutrino Interactions, *Physical Review Letters* 15 (9) (1965) 429–433.
URL <http://link.aps.org/doi/10.1103/PhysRevLett.15.429>
- [32] C. Achar, et al., Detection of muons produced by cosmic ray neutrinos deep underground, *Physics Letters* 18 (2) (1965) 196–199.
URL <http://www.sciencedirect.com/science/article/pii/0031916365907122>
- [33] T. J. Haines, et al., Calculation of Atmospheric Neutrino-Induced Backgrounds in a Nucleon-Decay Search, *Physical Review Letters* 57 (16) (1986) 1986–1989.
URL <http://link.aps.org/doi/10.1103/PhysRevLett.57.1986>
- [34] K. Hirata, et al., Experimental study of the atmospheric neutrino flux, *Physics Letters B* 205 (23) (1988) 416–420.
URL <http://www.sciencedirect.com/science/article/pii/0370269388916905>

- [35] K. Hirata, et al., Observation of a small atmospheric ν_μ/ν_e ratio in Kamiokande, *Physics Letters B* 280 (12) (1992) 146–152.
URL <http://www.sciencedirect.com/science/article/pii/0370269392907886>
- [36] C. Kraus, et al., Final results from phase II of the Mainz neutrino mass search in tritium β decay, *The European Physical Journal C - Particles and Fields* 40 (4) (2005) 447–468.
- [37] KATRIN Collaboration, KATRIN: A next generation tritium beta decay experiment with sub-eV sensitivity for the electron neutrino mass, arXiv:hep-ex/0109033.
URL <http://arxiv.org/abs/hep-ex/0109033>
- [38] J. Wolf, The KATRIN neutrino mass experiment, *Nucl. Instrum. Meth. A* 623 (1) (2010) 442–444.
URL <http://www.sciencedirect.com/science/article/pii/S0168900210005942>
- [39] K. Assamagan, et al., Upper limit of the muon-neutrino mass and charged-pion mass from momentum analysis of a surface muon beam, *Physical Review D* 53 (11) (1996) 6065–6077.
URL <http://link.aps.org/doi/10.1103/PhysRevD.53.6065>
- [40] R. Barate, et al., An upper limit on the τ neutrino mass from three- and five-prong tau decays, *The European Physical Journal C - Particles and Fields* 2 (3) (1998) 395–406.
URL <http://link.springer.com/article/10.1007/s100529800850>
- [41] H. V. Klapdor-Kleingrothaus, A. Dietz, H. L. Harney, I. V. Krivosheina, Evidence for Neutrinoless Double Beta Decay, *Modern Physics Letters A* 16 (37) (2001) 2409–2420.
- [42] GERDA Collaboration, Results on Neutrinoless Double- β Decay of ^{76}Ge from Phase I of the GERDA Experiment, *Physical Review Letters* 111 (12) (2013) 122503.
URL <http://link.aps.org/doi/10.1103/PhysRevLett.111.122503>
- [43] EXO Collaboration, Search for Neutrinoless Double-Beta Decay in ^{136}Xe with EXO-200, *Physical Review Letters* 109 (3) (2012) 032505.
URL <http://link.aps.org/doi/10.1103/PhysRevLett.109.032505>
- [44] KamLAND-Zen Collaboration, Limit on Neutrinoless $\beta\beta$ Decay of ^{136}Xe from the First Phase of KamLAND-Zen and Comparison with the Positive Claim in ^{76}Ge , *Physical Review Letters* 110 (6) (2013) 062502.
URL <http://link.aps.org/doi/10.1103/PhysRevLett.110.062502>
- [45] A. S. Barabash, SuperNEMO double beta decay experiment, arXiv e-print 1112.1784 (Dec. 2011).
URL <http://arxiv.org/abs/1112.1784>
- [46] ALEPH, DELPHI, L3, OPAL, SLD Collaborations, the LEP Electroweak Working Group, the SLD Electroweak and Heavy Flavour Groups, Precision Electroweak Measurements on the Z Resonance, *Phys. Rept.* 427 (2006) 257.

- [47] LSND Collaboration, Evidence for neutrino oscillations from the observation of $\bar{\nu}_e$ appearance in a $\bar{\nu}_\mu$ beam, *Physical Review D* 64 (11) (2001) 112007.
URL <http://link.aps.org/doi/10.1103/PhysRevD.64.112007>
- [48] MiniBooNE Collaboration, Improved Search for $\bar{\nu} \rightarrow \bar{\nu}_e$ Oscillations in the MiniBooNE Experiment, *Physical Review Letters* 110 (16) (2013) 161801.
URL <http://link.aps.org/doi/10.1103/PhysRevLett.110.161801>
- [49] G. Mention, M. Fechner, T. Lasserre, T. A. Mueller, D. Lhuillier, M. Cribier, A. Letourneau, Reactor antineutrino anomaly, *Physical Review D* 83 (7) (2011) 073006.
URL <http://link.aps.org/doi/10.1103/PhysRevD.83.073006>
- [50] M. Apollonio, et al., Initial results from the CHOOZ long baseline reactor neutrino oscillation experiment, *Physics Letters B* 420 (34) (1998) 397–404.
URL <http://www.sciencedirect.com/science/article/pii/S0370269397014767>
- [51] M. Apollonio, et al., Limits on neutrino oscillations from the CHOOZ experiment, *Physics Letters B* 466 (2-4) (1999) 415–430.
URL <http://www.sciencedirect.com/science/article/B6TVN-3Y8VGK1-1R/2/0f8c137ef210aa00bc3d7d9a90b8ed86>
- [52] M. Apollonio, et al., Search for neutrino oscillations on a long base-line at the CHOOZ nuclear power station, *The European Physical Journal C - Particles and Fields* 27 (3) (2003) 331–374.
URL <http://link.springer.com/article/10.1140/epjc/s2002-01127-9>
- [53] MINOS Collaboration, New constraints on muon-neutrino to electron-neutrino transitions in MINOS, *Physical Review D* 82 (5) (2010) 051102.
URL <http://link.aps.org/doi/10.1103/PhysRevD.82.051102>
- [54] MINOS Collaboration, Improved Search for Muon-Neutrino to Electron-Neutrino Oscillations in MINOS, *Physical Review Letters* 107 (18).
URL <http://link.aps.org/doi/10.1103/PhysRevLett.107.181802>
- [55] MINOS Collaboration, Electron Neutrino and Antineutrino Appearance in the Full MINOS Data Sample, *Physical Review Letters* 110 (17).
URL <http://link.aps.org/doi/10.1103/PhysRevLett.110.171801>
- [56] T2K Collaboration, The T2K experiment, *Nucl. Instrum. Meth. A* 659 (1) (2011) 106–135.
URL <http://www.sciencedirect.com/science/article/pii/S0168900211011910>
- [57] T2K Collaboration, Indication of Electron Neutrino Appearance from an Accelerator-Produced Off-Axis Muon Neutrino Beam, *Physical Review Letters* 107 (4) (2011) 041801.
URL <http://link.aps.org/doi/10.1103/PhysRevLett.107.041801>

- [58] T2K Collaboration, Evidence of electron neutrino appearance in a muon neutrino beam, *Physical Review D* 88 (3) (2013) 032002.
URL <http://link.aps.org/doi/10.1103/PhysRevD.88.032002>
- [59] D. Greiner, T. Lachenmaier, J. Jochum, A. Cabrera, Double Chooz detectors design, *Nucl. Instrum. Meth. A* 581 (1-2) (2007) 139–142.
URL <http://www.sciencedirect.com/science/article/B6TJM-4P940H6-B/2/b1a9e201ef2d92b85173bbd9d4f50bfb>
- [60] Double Chooz Collaboration, Indication of Reactor $\bar{\nu}_e$ Disappearance in the Double Chooz Experiment, *Physical Review Letters* 108 (13) (2012) 131801.
URL <http://link.aps.org/doi/10.1103/PhysRevLett.108.131801>
- [61] Double Chooz Collaboration, Reactor $\bar{\nu}_e$ disappearance in the Double Chooz experiment, *Physical Review D* 86 (5) (2012) 052008.
URL <http://link.aps.org/doi/10.1103/PhysRevD.86.052008>
- [62] Y. Declais, et al., Study of reactor antineutrino interaction with proton at Bugey nuclear power plant, *Physics Letters B* 338 (2-3) (1994) 383–389.
URL <http://www.sciencedirect.com/science/article/B6TVN-4729D5F-1H/2/b7bd28e082d3b1d8d629883fdf168ef2>
- [63] RENO Collaboration, RENO: an experiment for neutrino oscillation parameter θ_{13} using reactor neutrinos at yonggwang, 1003.1391.
URL <http://arxiv.org/abs/1003.1391>
- [64] RENO Collaboration, Observation of Reactor Electron Antineutrinos Disappearance in the RENO Experiment, *Physical Review Letters* 108 (19) (2012) 191802.
URL <http://link.aps.org/doi/10.1103/PhysRevLett.108.191802>
- [65] Daya Bay Collaboration, A Precision Measurement of the Neutrino Mixing Angle θ_{13} using Reactor Antineutrinos at Daya Bay, arXiv:hep-ex/0701029.
URL <http://arxiv.org/abs/hep-ex/0701029>
- [66] Daya Bay Collaboration, A side-by-side comparison of Daya Bay antineutrino detectors, *Nucl. Instrum. Meth. A* 685 (2012) 78–97.
URL <http://www.sciencedirect.com/science/article/pii/S016890021200530X>
- [67] Daya Bay Collaboration, Observation of Electron-Antineutrino Disappearance at Daya Bay, *Physical Review Letters* 108 (17) (2012) 171803.
URL <http://link.aps.org/doi/10.1103/PhysRevLett.108.171803>
- [68] Daya Bay Collaboration, Improved measurement of electron antineutrino disappearance at Daya Bay, *Chinese Physics C* 37 (1) (2013) 011001.
URL <http://iopscience.iop.org/1674-1137/37/1/011001>

- [69] Daya Bay Collaboration, Spectral Measurement of Electron Antineutrino Oscillation Amplitude and Frequency at Daya Bay, *Physical Review Letters* 112 (6) (2014) 061801.
- [70] K. Schreckenbach, H. Faust, F. von Feilitzsch, A. Hahn, K. Hawerkamp, J. Vuilleumier, Absolute measurement of the beta spectrum from ^{235}U fission as a basis for reactor antineutrino experiments, *Physics Letters B* 99 (3) (1981) 251–256.
URL <http://www.sciencedirect.com/science/article/pii/0370269381911205>
- [71] F. von Feilitzsch, A. Hahn, K. Schreckenbach, Experimental beta-spectra from ^{239}Pu and ^{235}U thermal neutron fission products and their correlated antineutrino spectra, *Physics Letters B* 118 (13) (1982) 162–166.
URL <http://www.sciencedirect.com/science/article/pii/0370269382906220>
- [72] K. Schreckenbach, G. Colvin, W. Gelletly, F. Von Feilitzsch, Determination of the antineutrino spectrum from ^{235}U thermal neutron fission products up to 9.5 MeV, *Physics Letters B* 160 (4-5) (1985) 325–330.
- [73] A. A. Hahn, K. Schreckenbach, W. Gelletly, F. von Feilitzsch, G. Colvin, B. Krusche, Antineutrino spectra from ^{241}Pu and ^{239}Pu thermal neutron fission products, *Physics Letters B* 218 (3) (1989) 365–368.
- [74] B. Achkar, et al., Search for neutrino oscillations at 15, 40 and 95 meters from a nuclear power reactor at Bugey, *Nuclear Physics B* 434 (3) (1995) 503–532.
URL <http://www.sciencedirect.com/science/article/B6TVC-3YS905D-F/2/e5b54776228f070b30ab6095afa02cdc>
- [75] S. Ait-Boubker, et al., Thermal neutron detection and identification in a large volume with a new lithium-6 loaded liquid scintillator, *Nucl. Instrum. Meth. A* 277 (23) (1989) 461–466.
URL <http://www.sciencedirect.com/science/article/pii/0168900289907754>
- [76] M. Abbès, et al., The Bugey 3 neutrino detector, *Nucl. Instrum. Meth. A* 374 (2) (1996) 164–187.
URL <http://www.sciencedirect.com/science/article/pii/0168900296002203>
- [77] B. Achkar, et al., Comparison of anti-neutrino reactor spectrum models with the Bugey 3 measurements, *Physics Letters B* 374 (1-3) (1996) 243–248.
URL <http://www.sciencedirect.com/science/article/B6TVN-3VTNGY6-1T/2/ee51e9276c07f4cf4558085a79861199>
- [78] F. Boehm, et al., Results from the Palo Verde neutrino oscillation experiment, *Physical Review D* 62 (7) (2000) 072002.
URL <http://link.aps.org/doi/10.1103/PhysRevD.62.072002>
- [79] F. Boehm, et al., Final results from the Palo Verde Neutrino Oscillation Experiment, *Physical Review D* 64 (11) (2001) 112001.
URL <http://link.aps.org/doi/10.1103/PhysRevD.64.112001>

- [80] KamLAND Collaboration, Precision Measurement of Neutrino Oscillation Parameters with KamLAND, *Physical Review Letters* 100 (22) (2008) 221803.
URL <http://link.aps.org/doi/10.1103/PhysRevLett.100.221803>
- [81] T. A. Mueller, D. Lhuillier, M. Fallot, A. Letourneau, S. Cormon, M. Fechner, L. Giot, T. Lasserre, J. Martino, G. Mention, A. Porta, F. Yermia, Improved predictions of reactor antineutrino spectra, *Physical Review C* 83 (5) (2011) 054615.
URL <http://link.aps.org/doi/10.1103/PhysRevC.83.054615>
- [82] A. C. Hayes, J. L. Friar, G. T. Garvey, G. Jonkmans, Reanalysis of the reactor neutrino anomaly, arXiv e-print 1309.4146 (Sep. 2013).
URL <http://arxiv.org/abs/1309.4146>
- [83] L. A. Mikalyan, V. V. Sinev, Neutrino oscillations at reactors: What is next?, *Physics of Atomic Nuclei* 63 (6) (2000) 1002–1006.
URL <http://link.springer.com/article/10.1134/1.855739>
- [84] G. L. Fogli, E. Lisi, A. Marrone, A. Palazzo, A. M. Rotunno, Hints of $\theta_{13}>0$ from Global Neutrino Data Analysis, *Physical Review Letters* 101 (14) (2008) 141801.
URL <http://link.aps.org/doi/10.1103/PhysRevLett.101.141801>
- [85] G. L. Fogli, E. Lisi, A. Marrone, A. Palazzo, A. M. Rotunno, Evidence of $\theta_{13}>0$ from global neutrino data analysis, *Physical Review D* 84 (5) (2011) 053007.
URL <http://link.aps.org/doi/10.1103/PhysRevD.84.053007>
- [86] T. Schwetz, M. Trtola, J. W. F. Valle, Global neutrino data and recent reactor fluxes: status of three-flavour oscillation parameters, arXiv:1103.0734 [astro-ph, physics:hep-ex, physics:hep-ph].
URL <http://arxiv.org/abs/1103.0734>
- [87] G. L. Fogli, E. Lisi, A. Marrone, D. Montanino, A. Palazzo, A. M. Rotunno, Global analysis of neutrino masses, mixings, and phases: Entering the era of leptonic CP violation searches, *Physical Review D* 86 (1) (2012) 013012.
URL <http://link.aps.org/doi/10.1103/PhysRevD.86.013012>
- [88] P. Vogel, G. K. Schenter, F. M. Mann, R. E. Schenter, Reactor antineutrino spectra and their application to antineutrino-induced reactions. II, *Physical Review C* 24 (4) (1981) 1543.
URL <http://link.aps.org/doi/10.1103/PhysRevC.24.1543>
- [89] IAEA, PRIS - country details.
URL <http://www.iaea.org/PRIS/CountryStatistics/CountryDetails.aspx?current=CN>
- [90] H. Band, et al., Target mass monitoring and instrumentation in the Daya Bay antineutrino detectors, *JINST* 8 (04) (2013) T04001–T04001.

- [91] P. Vogel, J. F. Beacom, Angular distribution of neutron inverse beta decay, $\bar{\nu}_e + p \rightarrow e^+ + n$, Physical Review D 60 (5) (1999) 053003.
URL <http://link.aps.org/doi/10.1103/PhysRevD.60.053003>
- [92] J. Liu, et al., Automated calibration system for a high-precision measurement of neutrino mixing angle θ_{13} with the Daya Bay antineutrino detectors, Submitted to Nucl. Instrum. Meth. A arXiv:1305.2248.
URL <http://arxiv.org/abs/1305.2248>
- [93] M. Yeh, A. Garnov, R. Hahn, Gadolinium-loaded liquid scintillator for high-precision measurements of antineutrino oscillations and the mixing angle, θ_{13} , Nucl. Instrum. Meth. A 578 (1) (2007) 329–339.
URL <http://www.sciencedirect.com/science/article/B6TJM-4NF7Y33-8/2/9382cc7f28a3e6d4f5f0229668aedd6b>
- [94] Y. Ding, Z. Zhang, J. Liu, Z. Wang, P. Zhou, Y. Zhao, A new gadolinium-loaded liquid scintillator for reactor neutrino detection, Nucl. Instrum. Meth. A 584 (1) (2008) 238–243.
URL <http://www.sciencedirect.com/science/article/pii/S016890020702092X>
- [95] M. Ambrosio, MACRO Collaboration, The MACRO detector at Gran Sasso, Nucl. Instrum. Meth. A 486 (3) (2002) 663–707.
URL <http://www.sciencedirect.com/science/article/pii/S0168900201021696>
- [96] Daya Bay Collaboration, The muon system of the Daya Bay Reactor Antineutrino Experiment, In preparation Daya Bay-docdb 7795-v18 (Dec. 2013).
- [97] M. Berger, J. Coursey, M. Zucker, J. Chang, ESTAR, PSTAR, and ASTAR: Computer programs for calculating stopping-power and range tables for electrons, protons, and helium ions, National Institute of Standards and Technology.
URL <http://physics.nist.gov/PhysRefData/Star/Text/ESTAR.html>
- [98] M. Berger, J. Hubbell, S. Seltzer, J. Chang, J. Coursey, R. Sukumar, D. Zucker, K. Olsen, Xcom: Photon cross section database, National Institute of Standards and Technology.
URL <http://physics.nist.gov/xcom>
- [99] W. Leo, Techniques for Nuclear and Particle Physics Experiments A How-to Approach, 2nd Edition, 1994.
- [100] D. Dwyer, et al., Standard slides for spectral oscillation measurement, Daya Bay docdb-9211 (Aug. 2013).
- [101] J. Ochoa, C. Lin, Y. Nakajima, P. Tsang, Adsimple reconstruction, Daya Bay docdb-7734 (Jan. 2013).
- [102] M. Yeh, Daya Bay liquid analysis, Daya Bay docdb-6615 (Jan. 2013).

- [103] H.D. Choi, et al., Database of prompt gamma rays from slow neutron capture for elemental analysis, Tech. Rep. STI/PUB/1263, IAEA, Vienna (2007).
URL <https://www-nds.iaea.org/pgaa/tecdoc.pdf>
- [104] D. Tilley, J. Kelley, J. Godwin, D. Millener, J. Purcell, C. Sheu, H. Weller, Energy levels of light nuclei, *Nuclear Physics A* 745 (34) (2004) 155–362.
URL <http://www.sciencedirect.com/science/article/pii/S0375947404010267>
- [105] W. Gu, G. Li, J. Liu, AmC background note, Daya Bay docdb-8979 (Dec. 2013).
- [106] S. Harissopulos, H. W. Becker, J. W. Hammer, A. Lagoyannis, C. Rolfs, F. Strieder, Cross section of the $C^{13}(\alpha,n)O^{16}$ reaction: A background for the measurement of geo-neutrinos, *Physical Review C* 72 (6) (2005) 062801.
- [107] B. Littlejohn, IAV Shape Distortion Correction for a Shape Analysis, Daya Bay docdb-8104 (Sep. 2012).
- [108] J. B. Birks, Scintillations from organic crystals: Specific fluorescence and relative response to different radiations, *Proceedings of the Physical Society. Section A* 64 (10) (1951) 874.
URL <http://iopscience.iop.org/0370-1298/64/10/303>
- [109] S. Jetter, Review of the IHEP non-linearity model, Daya Bay docdb-8995 (Jun. 2013).
- [110] J. Cao, Private communication (2012).
- [111] Z. Djurcic, J. A. Detwiler, A. Piepke, V. R. Foster Jr., L. Miller, G. Gratta, Uncertainties in the anti-neutrino production at nuclear reactors, 0808.0747.
URL <http://arxiv.org/abs/0808.0747>
- [112] X. Ma, L. Wang, Y. Chen, W. Zhong, F. An, Uncertainty analysis of fission fraction for reactor antineutrino experiments using DRAGON, Daya Bay docdb-9562 (Jan. 2014).
- [113] M. F. James, *Journal of Nuclear Energy* 23 (1969) 517.
- [114] V. Kopeikin, L. Mikaelyan, V. Sinev, Reactor as a source of antineutrinos: Thermal fission energy, *arXiv:hep-ph/0410100* *Phys.Atom.Nucl.* 67 (2004) 1892-1899; *Yad.Fiz.* 67 (2004) 1916-1922.
URL <http://arxiv.org/abs/hep-ph/0410100>
- [115] X. B. Ma, W. L. Zhong, L. Z. Wang, Y. X. Chen, J. Cao, Improved calculation of the energy release in neutron-induced fission, *Physical Review C* 88 (1) (2013) 014605.
URL <http://link.aps.org/doi/10.1103/PhysRevC.88.014605>
- [116] N. Haag, Experimental determination of the antineutrino spectrum of the fission products of ^{238}U , Ph.D. thesis, Technische Universitaet Muenchen (2013).

- [117] N. Haag, et al., Experimental determination of the antineutrino spectrum of the fission products of ^{238}U , arXiv:1312.5601 [nucl-ex].
URL <http://arxiv.org/abs/1312.5601>
- [118] V. I. Kopeikin, L. A. Mikaelyan, V. V. Sinev, Inverse beta decay in a nonequilibrium antineutrino flux from a nuclear reactor, Phys.Atom.Nucl.64:849-854,2001; Yad.Fiz.64:914-919,2001arXiv:hep-ph/0110290.
URL <http://arxiv.org/abs/hep-ph/0110290>
- [119] X. B. Ma, Y. F. Zhao, Y. X. Chen, Non-equilibrium corrections to reactor antineutrino spectrum and uncertainty analysis, Daya Bay docdb-9076 (Jul. 2013).
- [120] Z. Bin, R. Xi-Chao, N. Yang-Bo, Z. Zu-Ying, A. Feng-Peng, C. Jun, A study of antineutrino spectra from spent nuclear fuel at Daya Bay, Chinese Physics C 36 (1) (2012) 1.
URL <http://iopscience.iop.org/1674-1137/36/1/001>
- [121] P. Jaffke, P. Huber, Private communication.
- [122] V. I. Kopeikin, L. A. Mikaelyan, V. V. Sinev, Antineutrino background from spent-fuel storage in sensitive searches for θ_{13} at reactors, Physics of Atomic Nuclei 69 (2) (2006) 185–188.
URL <http://link.springer.com/article/10.1134/S1063778806020025>
- [123] J. Ling, X. Qian, W. Wang, C. Zhang, BCW Rate+Shape Analysis Technote, Daya Bay docdb-8768 (Aug. 2013).
- [124] R. Johnson, D. Wichern, Applied Multivariate Statistical Analysis, 5th Edition, Prentice Hall, 2002.
- [125] S. Jetter, "The Bump" in RENO and Daya Bay IBD spectra, Daya Bay docdb-9282 (Sep. 2013).
- [126] D. Dwyer, Y. Nakajima, J. Ochoa-Ricoux, K.-B. Luk, H. Steiner, K. Tsang, H. Wong, internal communication, Daya Bay docdb-9283 (Sep. 2013).
- [127] S.-H. Seo for the RENO Collaboration, New Results from RENO (Mar. 2013).
- [128] MINOS Collaboration, Measurement of Neutrino and Antineutrino Oscillations Using Beam and Atmospheric Data in MINOS, Physical Review Letters 110 (25) (2013) 251801.
URL <http://link.aps.org/doi/10.1103/PhysRevLett.110.251801>
- [129] K. Luk, Run Plan of Daya Bay 2013, Daya Bay docdb-9560 (Jan. 2014).

APPENDIX

The Daya Bay Antineutrino Detector Target Mass

The Daya Bay antineutrino detector (AD) target mass is defined as the number of protons (Hydrogen atoms) contained in the Gadolinium-doped scintillator (GdLS) within the main volume of the inner acrylic vessel. This quantity is obtained by subtracting the number of protons in connecting volumes and AD overflow tanks from the total GdLS mass that was filled into the detector. Knowledge of the relative numbers of protons in the target volume of each AD was projected to be the largest detection uncertainty affecting a $\sin^2 2\theta_{13}$ measurement at Daya Bay[65]. The primary analysis goal of the filling system was to determine the total Gd-doped liquid scintillator (GdLS) mass added to each AD with a relative uncertainty of less than 0.1%.

This appendix consists of a paper written describing the design and operation of the filling system[12]. Information pertaining to the liquid mass measurement is emphasized.

A.1 Mass Monitoring

The overflow tanks were designed to allow the liquids in the vessels to expand and contract with changes in temperature. For the GdLS, the number of molecules in the entire detector is constant, but as the liquid expands, a higher fraction of them will be located in non-active regions of the detector. To keep the target mass uncertainties as small as possible, these changes are monitored and corrected for. The amount of mass in the overflow tanks is proportional to the liquid height from the bottom of the tanks. It is monitored with a redundant system consisting of ultrasonic level sensors and capacitance level sensors installed on the tank. The system is described in [90]. Readings from these sensors are combined with the knowledge of the tank geometry to determine the overflow mass, which is subtracted from the total filled mass when determining the target mass.

A.2 Detector Filling System

The Daya Bay Antineutrino Detector Filling System and Liquid Mass Measurement

**H.R. Band^a, J.J. Cherwinka^b, E. Draeger^c, K.M. Heeger^a, P. Hinrichs^a,
C.A. Lewis^{a*}, H. Mattison^b, M.C. McFarlane^a, D.M. Webber^a, D. Wenman^b,
W. Wang^d, T. Wise^a, Q. Xiao^b**

^a *University of Wisconsin–Madison, Physics Department
Madison, WI 53706, USA,*

^b *Physical Sciences Laboratory, University of Wisconsin–Madison,
Stoughton, WI 53589, USA,*

^c *Illinois Institute of Technology
Chicago, IL 60616, USA,*

^d *Department of Physics, College of William & Mary,
Williamsburg, VA 23187, USA*

E-mail: clewis@physics.wisc.edu

ABSTRACT: The Daya Bay Reactor Neutrino Experiment has measured the neutrino mixing angle θ_{13} to world-leading precision. The experiment uses eight antineutrino detectors filled with 20-tons of gadolinium-doped liquid scintillator to detect antineutrinos emitted from the Daya Bay nuclear power plant through the inverse beta decay reaction. The precision measurement of $\sin^2 2\theta_{13}$ relies on the relative antineutrino interaction rates between detectors at near (400 m) and far (roughly 1.8 km) distances from the nuclear reactors. The measured interaction rate in each detector is directly proportional to the number of protons in the liquid scintillator target. A precision detector filling system was developed to simultaneously fill the three liquid zones of the antineutrino detectors and measure the relative target mass between detectors to $<0.02\%$. This paper describes the design, operation, and performance of the system and the resulting precision measurement of the detectors' target liquid masses.

KEYWORDS: Detector design and construction technologies and materials, Neutrino detectors, Liquid detectors.

*Corresponding author.

Contents

1. Introduction	2
1.1 Antineutrino detectors	2
1.2 Target mass definition	3
2. Detector filling requirements	3
2.1 Detector liquid handling	4
2.2 Filling in pairs	6
3. Detector filling system components	6
3.1 Pump stands	7
3.2 ISO tank	8
3.3 Calibration stand	8
3.4 Antineutrino detector platform and filling probes	9
3.5 Cover gas and gas purging	11
3.6 Filling system DAQ and control	12
4. Detector filling	14
4.1 Post-filling liquid additions	16
5. Liquid Level Monitoring	16
5.1 Liquid level requirements	16
5.2 Liquid level monitoring	16
5.3 Liquid level control	19
6. Liquid mass measurement	20
6.1 Load cells	20
6.2 Coriolis massflow meters	22
6.3 Peristaltic pump	23
6.4 Calibration consistency and uncertainties	24
6.5 Target mass measurement and determination of target protons	24
7. Summary	26
A. Filling Schematic	28

1. Introduction

The Daya Bay Reactor Neutrino Experiment [1] has used antineutrinos coming from the six nuclear reactors at the Guangdong Nuclear Power Complex outside of Shenzhen, China to make a precision measurement of the neutrino oscillation parameter $\sin^2 2\theta_{13}$ [2], [3]. The experiment employs four pairs of functionally identical detectors placed underground in three experimental halls between 300 m and 2 km from the reactor cores. The comparison of antineutrino-induced inverse beta decay rates in detectors in different halls determines the measured value of $\sin^2 2\theta_{13}$. Original experiment design called for deploying one detector from each pair at one of the halls near the reactors and its twin at the far site to minimize the correlated detection rate uncertainties at different halls. Pairs of detectors are assembled [4] simultaneously above ground and transported to a designated underground hall for filling before being installed in an experimental hall. Each detector is filled with roughly 80 tons of organic liquid scintillator and inert mineral oil. Figure 1 shows the locations of the reactors and the experimental halls.

Filling the detectors with scintillator and mineral oil is one of the final steps in detector construction. The process must preserve the structural integrity of the detectors and the chemical and optical properties of the detector liquids. It must ensure that identical detector response is preserved. Finally, filling provides the only opportunity for a precision measurement of the total liquid masses of each detector. Daya Bay’s design requirements called for a baseline (goal) of 0.3% (0.1%) relative uncertainty on the amount of target scintillator in each detector. This report provides an overview of the Daya Bay filling system including its construction and operation and the steps taken to meet the technical and physics requirements above.

This note is organized as follows: Section 2 discusses filling requirements. Section 3 includes details on the components of the filling system. Section 4 describes the process employed to fill each detector. Section 5 provides additional details about the methods used to maintain liquid levels. Section 6 describes the calibration and mass measurement leading to our determination of the overall detector mass uncertainty.

1.1 Antineutrino detectors

The Daya Bay antineutrino detectors (ADs) are three-zone liquid scintillator detectors optimized for detection of the inverse beta decay signal, $\bar{\nu} + p \rightarrow e^+ + n$. A cut-away view of an AD is shown in Figure 2. The outermost zone of an AD is contained inside a 5-meter cylindrical stainless steel vessel. This vessel contains photomultiplier tubes, their supporting structures, and top and bottom light reflectors. It is filled with mineral oil (MO) to buffer the detector’s inner zones from radiation coming from the PMTs and welds in the stainless steel vessel. Nested within it is the 4-m outer acrylic vessel. The outer acrylic vessel is the gamma catcher region; it is filled with a linear-alkyl benzene (LAB)-based liquid scintillator (LS). Within it is the 3-m inner acrylic vessel, which is the main target volume of the detector. The 3-m vessel is filled with scintillator that has been doped with

gadolinium (GdLS), but is otherwise similar to that in the gamma catcher. The inner acrylic vessel is the main target volume of the detector. Above the buffer, gamma catcher, and target volumes of each AD are overflow tanks. These ensure that the detector can tolerate thermal expansions and contractions without breaking or leaving the main volumes partially empty. There are also three ports spanning the top of each AD that have automatic calibration units mounted on them. The calibration units house sources used in periodic calibrations of the detectors. Additional details of the AD design can be found in references [1] and [5].

1.2 Target mass definition

The target mass of an antineutrino detector is defined as the quantity of gadolinium-doped scintillator contained within the 3-m acrylic vessel. This volume accounts for the majority of observed inverse beta decay events. The target mass is determined by subtracting the calculated mass of GdLS in a detector's central overflow tank and structures connecting the vessel to the overflow tank from the total mass of GdLS pumped into the detector during filling. Because the overflow and connecting volume masses are small relative to the main volume of the 3-m vessel, the dominant uncertainty in the target mass calculation comes from the uncertainty on the total GdLS mass. Thus measuring this quantity as precisely and consistently as possible is an important requirement of the filling system.

2. Detector filling requirements

All Daya Bay detectors are transported underground to the liquid scintillator (LS) hall for filling. The layout of the LS hall can be seen in Figure 3. The first requirement in

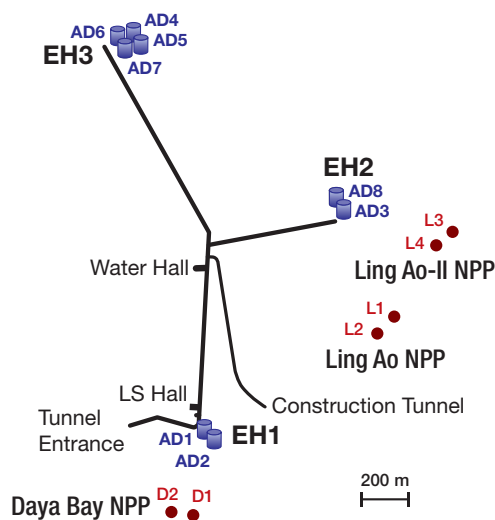


Figure 1. Layout of the Daya Bay experimental facilities and location of the underground liquid scintillator (LS) hall.

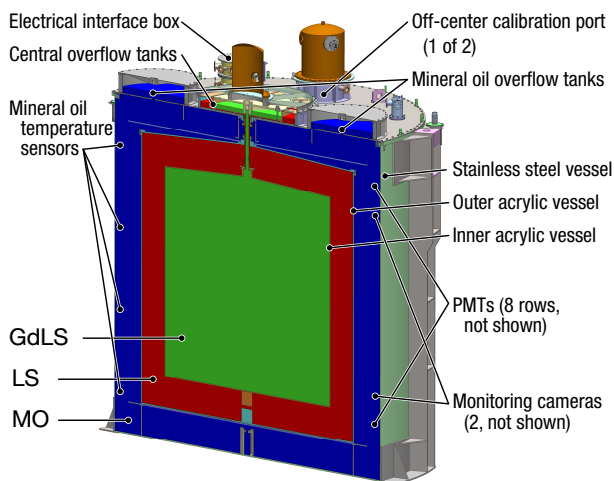


Figure 2. A cut-away view of the three-zone Daya Bay antineutrino detectors.

detector filling is to avoid causing physical damage to the vessels. This is accomplished by filling the three AD volumes concurrently and continuously monitoring liquid levels to keep hydrostatic pressures equal across the acrylic vessels. Liquids have similar densities and sit for several weeks in the temperature-controlled LS hall prior to filling.

A second requirement of the filling system is to determine the masses of each liquid delivered to each detector. The GdLS mass is especially important as it is directly related to the expected signal rates. Experimental requirements dictate that the mass measurement process must be kept as consistent as possible between detectors to minimize relative detection uncertainties that could cause a loss of precision in the $\sin^2 2\theta_{13}$ result. The requirement that a rate deficit caused by θ_{13} be distinguishable from a deficit caused by inconsistent quantities of target material puts a 0.3% limit on the allowed uncertainty in target mass between ADs. Thus we require that repeatability of the total GdLS mass measurement be well within the 0.3% limit. LS and MO masses are also measured by the filling system. However, aside from ensuring that all three detector vessels are completely filled, the quantities of LS and MO make negligible contributions to detector uncertainties.

Finally, filling must maintain the purity and identicalness of the liquids pumped into each detector. The system must avoid the introduction of contaminants that would raise the radioactive background rates (dust, radon, etc.) or degrade the light transmission properties of the scintillator (oxygen, iron). GdLS must also be drawn from storage and mixed to ensure that its chemical properties are identical between ADs.

2.1 Detector liquid handling

The ADs are filled with organic liquid scintillator (LS) and mineral oil (MO). Much of the Daya Bay Experiment's sensitivity to θ_{13} comes from the cancellation of systematic errors

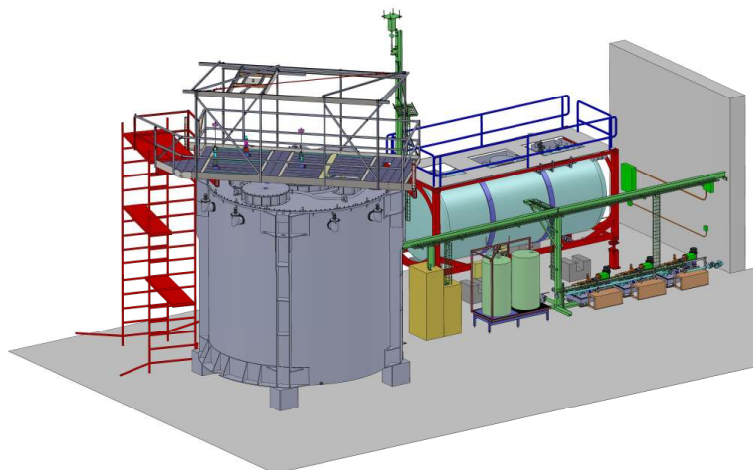


Figure 3. Engineering drawing of the filling system components in the LS hall. On the left are the scaffolding to the filling platform and an antineutrino detector. Proceeding to the right in the foreground are the electronics racks, calibration stand, and three pump stands. Behind these is the ISO tank used for GdLS weighing.

between nearly identical detectors. Thus it is important to maintain consistent chemical properties between liquids put into each AD.

Approximately 320 tons of linear alkylbenzene (LAB)-based liquid scintillator is produced in multiple batches. To ensure that any differences between batches do not cause non-identical detector response, the batches are mixed prior to detector filling.

The scintillator used in the target region is doped with natural gadolinium (GdLS) to increase its neutron-detection efficiency. Gadolinium has a large neutron-capture cross section and produces approximately 8 MeV of gammas after a neutron capture. This signal is used to distinguish inverse beta decay events from background. GdLS batches are divided between five storage tanks in the LS Hall during liquid production. This division would have minimized the loss of GdLS in the event of Gd precipitation from a faulty batch. In practice, no precipitation was observed in any storage tanks. Prior to filling a detector, GdLS is drawn equally from all five storage tanks into an ISO standard tank container, described in Section 3.2.

Undoped LS used in the gamma catcher region is transferred to a single 200-ton storage pool in the LS Hall. Like the LS, the mineral oil (MO) put into the outer buffer region of each AD is stored in a single 200-ton pool. The MO was produced in a single batch, but delivered to the filling hall in multiple deliveries, as more than 200 tons of MO were required to fill all eight detectors. The first delivery of MO was used to fill the first pair of

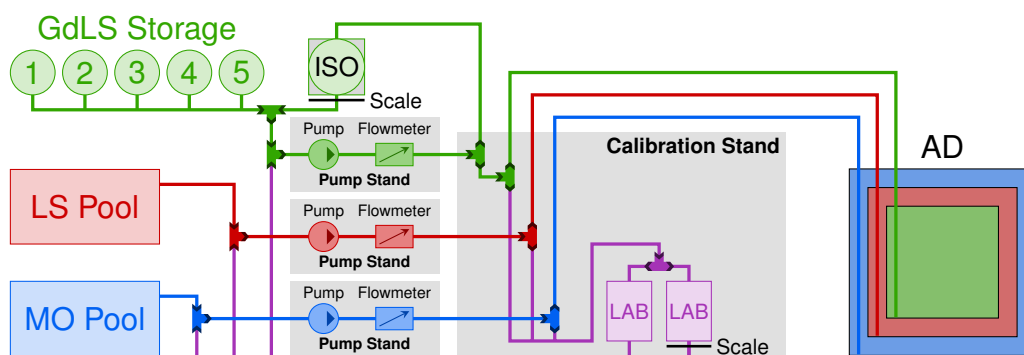


Figure 4. Simplified schematic of the liquid connections from the underground storage tanks for Gd-doped scintillator, plain liquid scintillator, and mineral oil in the underground liquid scintillator hall. Scales and flowmeters used for calibrations and detector liquid mass measurement are also shown. Component colors indicate the liquid in each line.

ADs; a second delivery was added to the pool before filling the second pair and the final delivery was added before filling the third pair of detectors.

Samples of detector liquids are collected at the beginning and end of filling for each detector. Analysis of these samples could reveal potential differences in the chemical or optical properties of the liquids put into a detector at the beginning versus the end of filling or between different detectors. To date, no significant differences have been observed. Densities of the filled liquids are 0.861 g/cm^3 for GdLS, 0.859 g/cm^3 for LS, and 0.85 g/cm^3 for MO at 22.2° , 22.4° , and 22.8° , respectively[6].

2.2 Filling in pairs

Emphasis on pair-wise identity of detectors led to planning filling campaigns for pairs of detectors. It is impractical to fill detectors simultaneously, but filling proceeds sequentially with as little delay as possible between the first and second ADs of a pair. This ensures that liquids in an AD pair are exposed to different conditions for no more than one week. In the event that detector liquids age differently in their storage pools than in the ADs, this would help preserve physics sensitivity in the event of unanticipated long-term liquid changes.

Additionally, there was initial concern that the mass measurement hardware might have a time-dependent calibration. Repeating identical calibration procedures in each filling campaign found that this was not a significant source of inconsistency between filling campaigns.

3. Detector filling system components

The detector filling system includes all physical and software components that enable detectors to be filled safely and efficiently in accordance with larger experimental goals. Pump stands house the metering pumps, liquid source selection valves, and supporting



Figure 5. Picture of GdLS pump stand with major components labeled.

plumbing and instrumentation used to direct each liquid around the liquid scintillator hall. An ISO tank container is used for intermediate target liquid storage. There is a calibration stand which holds two liquid tanks and a scale used for testing the mass flow meters. During filling campaigns, a platform installed on top of each detector gives filling team members safe access to the ports where plumbing and gas connections are made. The system data acquisition and control software is run through computers in an electronics stand. Figure 4 illustrates a simplified schematic of the plumbing components of the system. A more detailed schematic showing all valves and monitoring sensors can be found in appendix A.

3.1 Pump stands

There is one pump stand for each of the three detector liquids, consisting of the pump, liquid sensors, and supporting plumbing. Liquids are pumped by a Wanner HydraCell P600 metering pump with a 1-HP 480-V 3-phase AC motor. The pumps are controlled by TECO-Westinghouse N3 variable-frequency AC motor drives located in the electronics stand. Lines on the inlet (outlet) sides of the pumps have 1.5" (0.75") diameter. Each pump has an inlet and outlet valve for use in purging gas from the plumbing. The outlet valves are also used for collecting liquid samples at various points in the filling process. Each pump stand has a three-way valve to select a liquid source: either the filling hall storage containers or the tanks of the calibration stand. Additionally, the inlet and outlet lines contain pressure and temperature sensors. Behind each pump stand is a Coriolis flowmeter used for measuring the mass of each liquid. Over the pump stands are two sets of cable trays. The lower trays carry the liquid hoses and the Coriolis flowmeter cables, which are sensitive to electrical noise. The upper trays carry pump power cables, and less noise-sensitive sensor cables. Pumps and valve fittings were cleaned using vacuum component cleaning procedures during system assembly. The filling lines were cleaned with Citranox™ and rinsed with de-ionized water during system assembly. A labeled image of a pump stand is shown in Figure 5.

Components in contact with GdLS GdLS is sensitive to contact with metals, especially iron, although limited exposure to passivated SAE grade 316 stainless steel can be tolerated. For long-term contact, the allowed materials are limited to fluoropolymers, such as Teflon™ of all grades, including polytetrafluoroethylene (PTFE) and perfluoroalkoxy (PFA) resins, polyvinylidene fluoride (PVDF), acrylic, some grades of Viton™ fluoropolymer elastomers, and specific grades of polyurethane tubing. Extensive long-term compatibility testing was done to enumerate the allowed list of long-term-wetted materials. A special non-metallic PVDF pump head was used for the Wanner HydraCell P600 pump in the GdLS circuit. The metering pump used in the GdLS line was disassembled and the few remaining 316 stainless steel parts were passivated with nitric acid to remove loosely bound iron from their surfaces. Valves in contact with GdLS were entirely PVDF wetted. Hoses were Teflon™-lined with Teflon™ fittings and PVDF-lined Viton™ gaskets. Tygothane™ polyurethane tubing was used in the peristaltic pump. Liquid flow velocity was slow enough that electrostatic buildup was not a concern in the larger lines. In smaller lines, the Teflon lining was carbon-impregnated to increase conductivity and minimize charge build-up.

3.2 ISO tank

To ensure identical liquid response between detectors, GdLS is drawn in equal amounts from each of the five storage tanks. This liquid is collected in a 25,000-liter, completely PFA-lined buffer ISO tank container before being pumped into a detector. The tank was cleaned by the supplier (Nisshin Gulf Coast, Inc.) according to their procedures for high purity applications prior to delivery. During filling system assembly, it was rinsed with de-ionized water and dried with nitrogen.

After installation in the filling hall, nitrogen cover gas is supplied to the tank to avoid contamination of the GdLS with underground air. The ISO tank is instrumented with sensors monitoring the liquid level, liquid temperature, and cover gas exhaust pressure. The tank sits on four weigh-bridge load cells that are used to measure the liquid weight at the start and end of filling. During installation, the corners were shimmed to balance the weight at each load cell to within 6% of the nominal tank weight. A valve at the tank inlet allows liquids to be purged from the lines connecting the storage tanks to the ISO tank immediately prior to filling it. This removes potential contaminants or precipitates from the GdLS that will go into the detectors. Purged liquid is drawn mostly from a single storage tank, which is rotated with each filling campaign to maintain equal tank depletion rates.

3.3 Calibration stand

The calibration stand, shown in Figure 6, consists of a steel frame holding two 600-liter polyethylene (PE) tanks. Approximately 550 liters of plain LAB are held in these tanks for use in calibrations. The LAB from the calibration stand is also used to purge liquid lines when preparing the system for storage between filling campaigns. One tank sits on a scale, used to compare mass changes to the flow meters being calibrated. The scale is a Sartorius

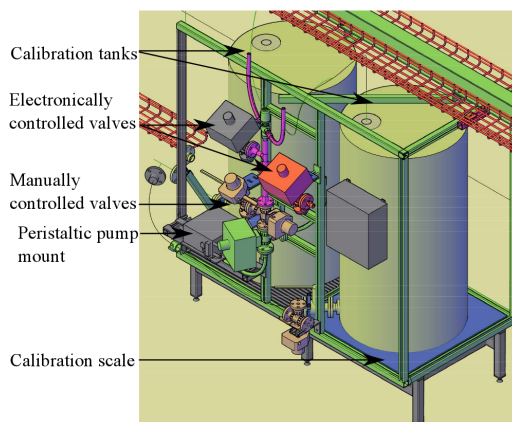


Figure 6. A model of the calibration stand showing the valve tree with major components labeled. Connecting hoses have been removed for clarity.

CAPP4U-2500KK-LU Combics industrial floor scale, controlled by a Sartorius CISL1U Combics 1 indicator. The scale contains four load cells, has a 1500 kg capacity, and has a precision (readability) of 0.05 kg. Each calibration tank has an outlet valve that can be opened to the pump inlet manifold.

The calibration stand frame holds the “valve tree,” a collection of valves to direct liquid into the calibration tanks or to a detector. Hoses connect the valve tree to each pump stand, the ISO tank, and the top of the detector installed in the hall. A fast-operating solenoid diverter valve is used to direct calibration stand flow into either of the calibration tanks. A combination of manually and electronically controlled valves are used. In both the LS and MO lines, a single electronically-controlled three-way valve allows liquid to be directed into the calibration stand or to the detector being filled. The GdLS plumbing has a more complicated topology. The calibration stand holds two manually-controlled valves to direct GdLS into the calibration stand or detector. An electronic valve in the GdLS line is used to select a pump line leading to the detector through the metering pump or through the peristaltic pump. There are additional manual valves for GdLS to allow liquid to flow into the ISO tank. All valves have electronic readouts used to supply operators with valve position information before and during pump operation.

3.4 Antineutrino detector platform and filling probes

Liquids are added to detectors through ports on their lids. When installed on stands on the filling hall floor, the top of each detector is nearly 6 meters from the floor. The filling team must access these ports to connect gas tubing, insert filling and level probes, connect the filling system hoses to the detector, and attach sensor cables. Additional hazards of

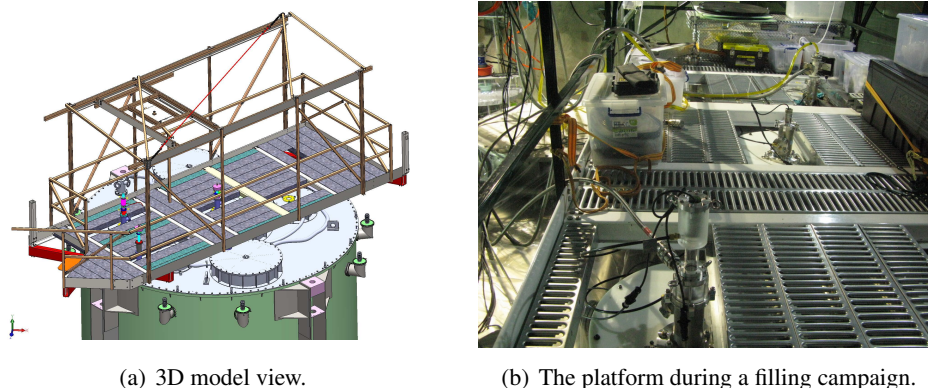


Figure 7. The detector filling platform, which provided a safe environment for working atop the detector during filling campaigns.

work atop a detector come from the numerous protrusions and hoses necessary for various detector systems. To conduct filling operations safely the filling platform shown in Figure 7 is hoisted on to and off of the detector lid using two balanced pick points. Decking on the filling platform is removable to give direct access to the lid for probe installation. The platform has a movable hoist, useful for holding the probes during their insertion and removal.

Filling and level probes Hoses from the filling system are connected to the detectors via tubes referred to as filling probes. Three such probes are inserted into each detector during filling preparations and removed after filling. Additionally, ultrasonic level sensors, used to monitor liquid heights during filling, are mounted on another set of probes. These are referred to as level probes. Drawings of three of the six probes are shown in Figure 8.

Prior to use in the LS hall, the filling and level probes and their corresponding flanges were cleaned on-site. Brushes or micro-wipes were passed over all probe surfaces in an Alconox solution bath. They were rinsed with de-ionized water exceeding 7 MOhm-cm until the rinsate resistivity was indistinguishable from the resistivity of the supply water. The probes were then air dried in the clean room used for AD assembly.

In preparation for filling, probes are inserted into each AD through temporary nylon cover plates installed on the lid in place of the automatic calibration units. During physics operation, these apertures provide a path for calibration sources to be lowered into the scintillator liquid. The GdLS and MO regions of the detector have separate probes for filling and level monitoring, but for the LS region, there is only one port available, so the filling and level probes are concentric.

Due to the high cost of underground rock excavation there is limited clearance between the top of a detector and the hall ceiling. Consequently each filling probe is assembled from multiple segments. Each segment screws onto the next, in a manner similar to well drilling.

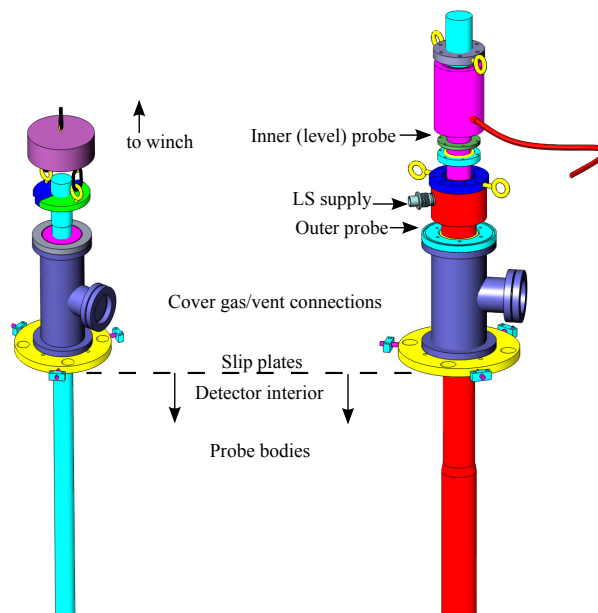


Figure 8. Engineering models of the mineral oil level probe (left) and the liquid scintillator level/fill probe (right). The top section of the LS probe illustrates the mounting of the ultrasonic level sensor used to determine liquid height in that probe’s central region.

The three filling probes extend to within centimeters above the bottom surface of their respective liquid vessels to guide the fluid and prevent excessive splashing. The three level probes rest on thin PTFE pads in contact with the floor of their designated vessel. Probes in contact with LS and GdLS were constructed from cast acrylic tubing. To accommodate the poor structural properties of acrylic a custom Stub Acme type thread (ANSI/ASME B1.8-1977) was used to connect the segments. The MO probes were stainless steel tubes. Sensitivity of ultrasonic sensors to stray reflections necessitated careful machining of the level probe segments to avoid creating steps at the joints.

3.5 Cover gas and gas purging

To keep liquids, particularly the scintillators, out of contact with oxygen, moisture, and radon, nitrogen cover gas from commercial grade boil-off liquid nitrogen is used extensively. For the supplied nitrogen, the oxygen content was found to be < 5 ppm, the room-temperature relative humidity $< 0.5\%$, and the radioactivity ≤ 5 Bq/m³. Gas lines run from an alcove outside the filling hall to manifolds inside. From there nitrogen is supplied to the ISO tank and detector via the AD cover gas system described in [7].

At the beginning of several filling campaigns, there were residual gases in the detectors from leak-checking internal seals during detector assembly. It was necessary to remove oxygen from the detector volumes to prevent its absorption and subsequent quenching

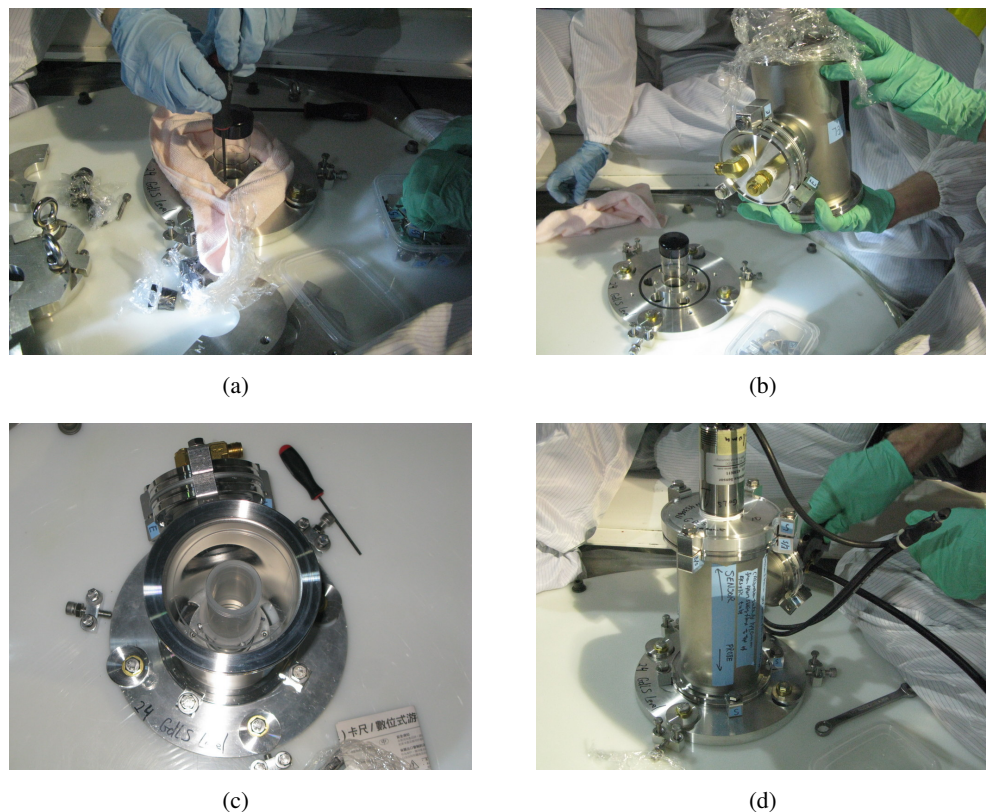


Figure 9. A sequence of images of the GdLS level probe being installed. The top acrylic section deployed through the port cover (a). The gas flange and ultrasonic support is placed over the probe end (b, c). Finally, the ultrasonic sensor is mounted to the top of the assembly (d).

of scintillator light. Additionally, the heavy leak checking gases argon and Freon have significantly lower speeds of sound than nitrogen and are undesirable due to their distortion of the ultrasonic liquid level measurements. Several volume exchanges of dry nitrogen were required to properly purge each AD prior to filling.

3.6 Filling system DAQ and control

The filling computer system collects data from the various sensors within the filling system. Its secondary purpose is to provide filling operators with an interface for monitoring this data and controlling both pump speeds and valve positions. A National Instruments PXI-8108 Core 2 Duo 2.53-GHz controller running the Phar Lap ETS real-time operating system communicates with the hardware and makes a primary log of the data. The user interface software is run on a Windows PC. The PC maintains a second log of the data, provides monitoring information to system operators, and allows operator control of the pumps and automatic valves. Communication between the PXI and the PC is via network variables. The software for the filling system was written in National Instruments LabView 2009.

Readout electronics Data from most sensors in the filling system is read and logged at 10 Hz. Several National Instruments DAQ cards are used to acquire information from the filling system sensors. The Coriolis flowmeters' analog outputs and the pump inlet and outlet pressure sensors produce 4–20 mA signals, read out by a NI PXI-6238 card. Pump inlet and outlet temperature sensors produce a 0–5 V signal, read out on an NI PXI-6281 card. Additionally, digital counters on the PXI cards are used for collecting the pulse output from the rotation encoder on the peristaltic pump and the incremental mass totals from each Coriolis flowmeter. Digital IO pins on these cards are also used to determine the current positions of switches on several filling system valves. The PXI controller has a single RS-232 port that is used to communicate with the floor scale in the calibration stand.

Additional sensors are grouped into RS-485 chains based on importance and communication protocol, and read out from a NI PXI-8433/4 card. The majority of RS-485 sensors use the Modbus/RTU protocol and are set to communicate at 9600 or 38400 baud. The load cell controller has a unique protocol and was therefore given its own designated port. The three metering pump controllers share an additional port. Three digital signal concentrators from DGH used for valve position monitoring and control also have their own port. Four Pt100 temperature sensors, which monitor the liquid temperatures are read out by a single Seneca Z-4RTD-2 temperature readout controller located on the calibration stand. Each Pt100 sensor is connected to the readout controller by a four-wire “Kelvin” connection in order to minimize the impact of lead lengths, which can be up to several meters. The readout controller is daisy chained with the ISO tank pressure sensor and the ultrasonic level sensors to the fourth RS-485 port.

Procedures and safety checks Avoiding contamination or spills of detector liquids is a high priority in detector filling operations. It is also important that liquids flow correctly through the system during filling to minimize uncertainties on the measured detector masses. To guarantee consistent and safe operation, all activities related to filling system operation were conducted according to detailed procedures. These procedures were extremely important as there were several months between filling campaigns and there was some rotation in filling personnel.

To assist operators in quickly determining the state of all valves in the system, a modified schematic of the filling system plumbing was created in the software. Components are labelled and colored according to the liquid they contact. Colored paths are used to show the direction of liquid flowing through the system given the valve states at any given time. Additionally, a software interlock was written to enforce strict adherence to valve manipulation procedures. The interlock would shut down and disable the pumps in the event of a valve found out of position, thus minimizing any potential loss of liquid. This was not consistently used after the initial pair of detectors was filled; the pumps were all stopped during stage transitions where valve manipulation was required and the filling team had adequate control over the system to prevent valve manipulation at other times.

4. Detector filling

Preparing and filling a single antineutrino detector takes approximately one week. Pairwise filling dictates that each filling campaign lasts approximately three weeks, accounting for initial sensor calibrations, transportation of detectors into and out of the filling hall, probe insertion and removal, ISO tank filling, and pumping of liquids into the detector.

While detector preparations are underway, the Coriolis flowmeters are calibrated and the ISO tank is filled from the GdLS storage tanks. During the ISO tank filling process, approximately 4 tons of GdLS is drawn from each storage tank in sequence. Between tanks, load cell calibration points are collected. The complete ISO tank filling and load cell calibration takes approximately 24 hours. This step is done on an around-the-clock schedule to minimize GdLS contact with the metering pump for material compatibility reasons discussed in section 3.1.

Detector filling proceeds when all preparations are complete. Filling is divided into stages based on the region of the AD the liquid level has reached, or equivalently, what liquids are being pumped into the detector vessels. The cutaway view of a detector in Figure 2 illustrates that cross-sectional areas filled by each liquid change as the lower and upper boundaries of each vessel are reached. At transitions between stages pump speeds are adjusted to compensate for the new ratios of cross-sectional area being filled by each liquid. Within transitions, pump speeds are adjusted as necessary to maintain equal liquid heights. Figure 10 shows mass flow rates as filling progresses for two different detectors. Diagnostic plots produced in real time in the control software display liquid height-versus-total mass pumped. The slopes of these plots are proportional to the cross-sectional area being filled by each liquid and change abruptly at vessel transitions.

Initially, roughly 6 tons of MO is pumped at approximately 1300 kg/hour until liquid has reached the bottom of the 4-m acrylic vessel. At this point, the cross-sectional area being filled by MO decreases from roughly 20 m^2 to 7 m^2 . This is observed as a change in the slope of the MO level sensor's height-versus-mass-pumped plot. LS pumping is then started with a massflow rate of approximately 940 kg/hour and the MO flow rate is adjusted to 520 kg/hour to maintain equal liquid levels in the two vessels. Then MO and LS are filled simultaneously until the 3-m acrylic vessel is reached. At the bottom of the 3-m vessel, the cross-sectional area of the LS region decreases and LS height-versus-mass-pumped plot rapidly increases analogous to that in MO at the previous transition. A second indication of this transition is the appearance of a dark band of LS just past the floor of the 3-m vessel in the bottom monitoring camera. Once this transition has occurred, the GdLS lines are purged, liquid samples are collected, and the initial ISO tank weight is collected. For weight collection, all valves in the GdLS line are closed and the nitrogen flow rate to the ISO tank is set to 30 liters/minute.

Filling continues with all three liquids. GdLS is pumped at a constant speed corresponding to 930 kg/hour with LS and MO rates adjusted to maintain equal liquid heights. Liquid heights increase at a rate of roughly 2 mm per minute during this stage. After

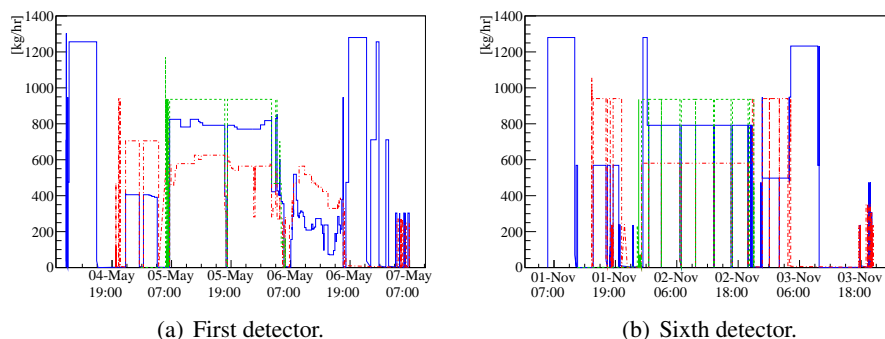


Figure 10. Approximate mass flow rates of MO (blue, solid), LS (red, dot-dashed), and GdLS (green, dashed) as a function of time during filling of the first and sixth detectors. Gross changes in the pump speed ratios are made as vessel boundaries are reached to compensate for the changes in cross-sectional area being filled by each liquid. Minor pump speed adjustments are made to the more slowly pumped liquids to maintain equal liquid heights across the three volumes. Brief pauses of all liquids were used to reestablish the siphon drawing LS out of its storage pool. Longer breaks prior to and after the conclusion of GdLS pumping were planned to ensure that major transitions would occur at the desired times. The diminishing number of pump speed adjustments between AD 1 and AD 6 attests to the identity of detectors and increasing expertise of the filling crew. The increasing number of short pauses indicate the difficulty in maintaining a siphon out of the LS storage pool as it emptied.

approximately 24 hours with continuous pumping, the 3-m lid is reached. The lid of the 3-m vessel is a shallow cone. Level sensors for GdLS begin to show an increase in the slope of the height-versus-mass-pumped curve with a corresponding decrease in the LS level slope. This transition is also visible in the top monitoring camera, although reflections from the liquid surfaces and vessel edges can complicate interpretation of the images. For this reason, in later filling campaigns, a small liquid level difference was intentionally imposed near the beginning of this transition. GdLS pumping is stopped once either the camera or level sensor indicates that liquid is just above the top of the cone. LS and MO pumping are continued to the top of the 4 m vessel and stainless steel vessel lid, respectively. The entire process takes approximately two days. During the late filling stages, the inner (outer) acrylic vessel is compressed slightly by the rising LS (MO), which causes the GdLS (LS) liquid level to continue increasing in the small volumes connecting each vessel to the overflow tanks.

After MO reaches the top of the detector, several dozen kilograms of each liquid is added to fill the overflow tanks to a level approximately 8 cm above the detector lid. This is one third of the overflow tank capacity. GdLS is added through the peristaltic pump at this stage, since the liquid in the metering pump lines has been in contact with stainless steel for many hours and repurging would reduce accuracy of the mass measurement. LS and MO are added using their respective metering pumps at a low speed.

4.1 Post-filling liquid additions

After liquids have reached the desired height in the overflow tanks, pumps are shut down and all valves are closed. The ISO tank is weighed to determine the amount of GdLS in the AD. The final tank weighing is done with ISO tank nitrogen flow held at the same rate as in the initial weighing and all GdLS line valves are closed in both cases to avoid biasing the relative mass measurement. Final liquid samples are drawn from the filling system. The filling probes are removed, monitoring cables to the AD are disconnected, and the AD is prepared for transportation to an experimental hall.

During filling, bubbles can become trapped in more complicated geometric areas around the tops and bottoms of AD vessels. In transit, some of these bubbles are released and liquid heights observed in the overflow tanks decrease. To ensure that there is sufficient liquid to keep the overflow liquid heights in a measurable range, additional LS and MO are added manually from ports in the top of each detector. The liquid is put into 5-liter bottles which are weighed before and after pouring into the AD to measure the change in liquid mass. After filling the first detector, approximately 15 kg of LS and 117 kg of MO were added in this manner. Knowledge gained in the first fill led to modifications of the main filling procedures and subsequent detectors required smaller amounts of additional liquid. It was not necessary to manually add GdLS after filling for any of the detectors. The relatively simple geometry of the inner acrylic vessel interior reduced the amount of trapped gas in the GdLS volume, which led to less dramatic height differences. Additionally, flexibility of the acrylic vessels allowed some cross-talk between liquid heights and the GdLS level could to be raised by a few millimeters through additions of LS when necessary.

5. Liquid Level Monitoring

5.1 Liquid level requirements

Daya Bay's antineutrino detectors (ADs) are cylindrical and approximately 5 meters in diameter. Their volume is divided into three regions by two acrylic vessels with diameters of 4 m and 3 m. The walls of these vessels have thicknesses between 9 and 20 mm[5], making them moderately fragile. Thus a sustained pressure differential between the inside and outside of each vessel could cause them to craze or break. To prevent damage, all three volumes of a detector are filled simultaneously. A major priority for the filling system is to maintain liquid level differences of a few centimeters or less, corresponding to equal hydrostatic pressures on both sides of each vessel. This is accomplished using ultrasonic level sensors mounted on the level probes and visual inspection with the detector's internal monitoring cameras.

5.2 Liquid level monitoring

Liquid levels in each vessel are monitored using ultrasonic level sensors and two cameras mounted inside the detectors. The ultrasonic sensors are placed atop acrylic or stainless

steel tubes hereafter referred to as level probes. The level probes sit on thin teflon pads on the bottom of each vessel and have multiple openings near the bottom to allow liquid to enter. The cameras are mounted between the stainless steel vessel and the outer acrylic vessel on the photomultiplier support structures. Data from the combination of level sensors and cameras allows the filling team to make pump speed adjustments as necessary to maintain approximately equal liquid heights.

Ultrasonic sensors To continuously monitor the liquid heights in each of AD vessels, we use three SENIX ToughSonic TSPC-15S ultrasonic distance sensors mounted to hollow level probes inserted at the top of the AD as described in section 3.4. These sensors were chosen for their optimal range, roughly 0.25 to 6 m, which allows the same model sensor to be used to determine liquid heights through the entire volume of the 3-, 4-, and 5-m vessels. The level probes serve as stilling tubes, providing a clear path for the ultrasonic pulse to the liquid surface.

The ultrasonic sensors measure a number of counts proportional to the time between the emission of a sound pulse from the ultrasonic sensors and the reception of the reflected pulse. Prior to their use in AD filling, the sensors were calibrated at 6-inch intervals along their respective level probes using a system of threaded rods with a flat stopper attached to the leading end. The goal of this calibration was to develop a simple conversion of the raw data into a liquid height relative to the bottom of each vessel. Optimal settings for sensor gain and internal averaging were also determined. When filling the actual detectors, the conversion was adjusted to compensate for the slight difference in the speed of sound between air and pure nitrogen.

In practice, the ultrasonic sensors were somewhat problematic. During testing and sensor calibration the sensors were found to be extremely sensitive to reflections of the sound pulse from interior gaps or edges in the level probes. Level probe designs were modified to accommodate this behavior. During the first filling campaign, noise in the LS level sensor made interpreting its height measurements challenging. It was eventually determined that the sensors did not function completely reliably in environments with mixtures of different gases. Additionally, minor changes in the LS pump speed caused sudden jumps in the reported height. We hypothesize that gas pressure differences between the filling probe and AD together with liquid sloshing may have contributed to this and other periodic fluctuations in the measured liquid heights of all sensors. These difficulties led to increased reliance on the AD camera system to monitor and maintain liquid levels. Example of height-versus-mass information from the level sensors at some of the filling transitions is shown in Figure 11.

Cameras Each AD has two cameras mounted inside the stainless steel vessel on the PMT support structure, as described in detail in [8]. The cameras have both visible and infrared light sources. During the majority of filling stages the cameras provide visual confirmation of the liquid levels. Initially, they were intended to provide a cross-check of

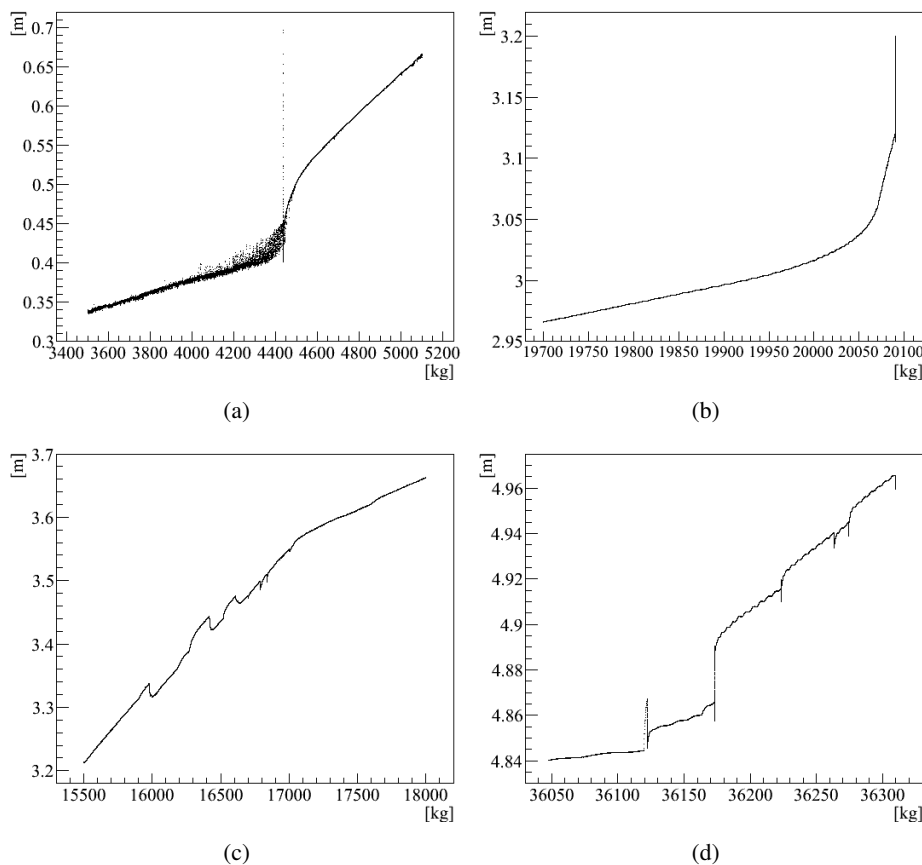


Figure 11. Example height data versus mass data from a) the LS transition at the bottom of the inner acrylic vessel, b) the GdLS transition at the top of the inner acrylic vessel, c) the LS transition at the top of the outer acrylic vessel, and d) the MO transition at the top of the outer acrylic vessel. Similar plots are made in real time during detector filling to determine when the various filling transitions have been reached.

the ultrasonic sensors. In practice, the ultrasonic sensor noise made the cameras the primary means of checking liquid height variations between vessels and setting pump speeds. The level sensors were used primarily to confirm the large changes in vessel cross section that occurred at each vessel boundary.

The two cameras provide nearly full vertical viewing coverage of the acrylic vessels, with one camera located at the top of the detector and one at the bottom. They look inward, centered on the transition regions where the cross-sections of the detector volumes change quickly, such as the tops and bottoms of the acrylic vessels. The cameras provide visual confirmation of liquid levels in these areas, giving feedback to properly adjust the pump speeds, which change abruptly in the transition regions. At times, the cameras allowed the team to pause the filling process to easily and safely equalize liquid levels as illustrated in

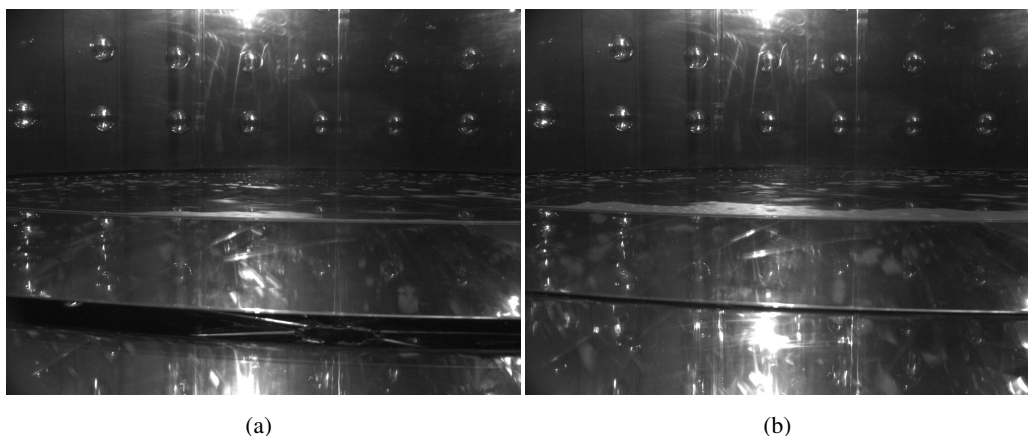


Figure 12. Two example camera images used to confirm the correction of a small offset in the liquid scintillator and Gd-doped scintillator heights. In the figure at left, the plain scintillator was slightly higher. Stopping the corresponding pump for a few minutes equalized the levels and caused the dark reflection to go away.

Figure 12. The cameras run continuously during filling, saving images every 60 s. This allows review of the filling process during and after completion. Over 2,000 images per detector were taken during each AD fill. Video made from images collected during some fills can be found at [9]

5.3 Liquid level control

Pump speed adjustments during filling maintain equal liquid levels across the detector volumes. The HydraCell P600 metering pumps have a reliably linear relationship between motor speed and fluid pumping rate. The practical dynamic range of these pumps ranges from 0–1100 liters/hour for the liquid scintillator lines and 0–1500 liters/hour for the mineral oil line. The upper range is determined by the power required to pump liquids of our viscosity through the smallest apertures in the line, the Coriolis flowmeters. The variable-frequency motor drives can adjust the pump motor speeds in increments as small as 0.2 liters/hour.

For the majority of a detector fill, liquid heights increase at roughly 2 mm per minute. The maximum liquid level difference the vessels could safely sustain is between 100 and 150 mm, thus pump speed adjustments are rarely time critical. Adjustments were made manually by the system operators as infrequently as possible to preserve the accuracy of the mass flowmeters, which perform best with constant flow rates. During stages with multi-liquid pumping, the pump speed for the liquid filling the largest cross-sectional area is kept constant. The range of massflow rates used during filling is generally between 200 and 1300 kg/hour due to the need to stay within the Coriolis flowmeters' most accurate performance ranges (see also section 6.2). Due to the near-identicalness of AD construction, knowledge of the previously used average pumping speeds makes liquid level matching

increasingly straightforward. As illustrated in Figure 10, between filling the first and the sixth detector, the number of speed adjustments during each stage of filling decreased significantly as the filling team gained experience.

6. Liquid mass measurement

As discussed in section 2, the filling system is required to keep mass measurement biases consistent to better than 0.3% between each detector with a goal of 0.1% or less. In practice, the filling and calibration scheme employed exceeded this goal and kept the relative target liquid mass uncertainty within 0.02%. The primary Gd-doped scintillator mass is determined by weighing the ISO tank at the beginning and ending of each fill, then applying corrections for the scale's calibration and weight of nitrogen displacing liquid in the tank. Coriolis massflow meters in each liquid line are used to measure the plain scintillator and mineral oil masses and to provide a backup measurement of the Gd-doped scintillator mass.

6.1 Load cells

As discussed in Section 2.1, enough GdLS to fill one AD is drawn into an ISO tank prior to filling the detector. The total liquid mass is determined by subtracting the final tank weight from the initial tank weight and applying corrections for the load cell calibration and mass of N₂. To enable weighing, the ISO tank is mounted on four Sartorius PR6221 compression load cells. Each load cell is OIML class C6, corresponding to 0.008% accuracy over the maximum range of 20 t, or an uncertainty of 1.6 kg. Individual load cells connect to a Sartorius X5 (PR5610) controller that converts a voltage signal, integrated over 1 s, from each load cell into a weight.

Studies of the load cells found that the dominant contribution to the relative load cell uncertainty comes from long-term electronic drift. Drift data was collected over several-day periods with the ISO tank full and empty to ensure consistency of the drift behavior. Example drift results are shown in Figure 13. The load cells demonstrated relatively high-frequency noise, which was electronic in origin but was not traceable to any known sources; it was consistent over and between filling campaigns and does not impact the relative mass uncertainties. The noise was reduced by averaging load cell readings over a 15-minute period. The uncertainty caused by longer-term drift is taken to be the maximum variation seen in a running 15 minute average over several days of drift data: ± 3 kg (or 0.015% of 20 t). This uncertainty contributes to both our absolute and relative understanding of the detector masses. Drift data was collected on various occasions with weights representative of the maximum and minimum ISO tank weights during filling.

Load cells are calibrated during ISO tank filling prior to filling each detector. Calibration points are collected by hanging four 1000 kg calibration masses (OIML class M1, 50 gram mass accuracy) from the tank frame. One mass is suspended near each corner of

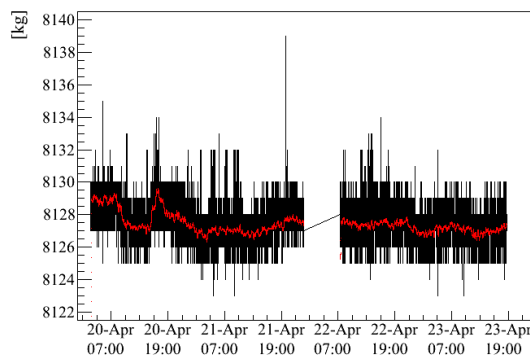


Figure 13. Example of load cell drift data acquired from letting the ISO tank rest undisturbed for several days. The red line represents a 15-minute average, which reduces noise. The maximum variation observed is taken as the relative uncertainty on the total filled GdLS mass due to the load cells.

the ISO tank with nylon straps. Six calibration points are taken: one at the beginning of the ISO tank fill and an additional one after liquid has been drawn from each of the GdLS storage tanks. These calibration points allow us to confirm that the load cell linearity is a negligible contribution to the absolute mass uncertainty.

A load cell correction factor is determined from the calibration data collected at the time of each detector fill. By repeating this procedure for each detector, the calibration serves as a diagnostic of the system and ensures that possible variations over the sixteen months between filling the first and last detector would not contribute to relative proton uncertainty. All collected load cell calibration points are shown in Figure 14. The measured weight of the calibration masses was consistent in all filling campaigns, and thus does not contribute to the relative mass uncertainty between detectors.

The combined calibration mass was read out as approximately 3992.8 kg, roughly independent of the mass of GdLS in the ISO tank. Thus it is concluded that a +0.18% correction should be applied to the load cell-reported GdLS mass. A probable cause of this correction is that g used by the load cell controller is 9.81379 meters/s², which is a few tenths of a percent higher than local g at the latitude of Daya Bay. The uncertainty on the correction to the load cell readings, given by the standard deviation from the mean of all calibration points, is ± 0.35 kg (0.01% of the calibration mass).

When evaluating the detector GdLS mass, an additional correction is applied to the load cell mass data to include the weight of nitrogen displacing GdLS removed from the ISO tank. This correction is made by scaling the calibrated load cell reading by a factor of $1 + \frac{\rho_{\text{gas}}}{\rho_{\text{liquid}}}$. The density of GdLS is measured by the Coriolis flowmeter, and the density of nitrogen in the ISO tank is calculated using the temperature and pressure measured by sensors inside the ISO tank. The magnitude of the correction is approximately 0.13% for dry nitrogen and GdLS.

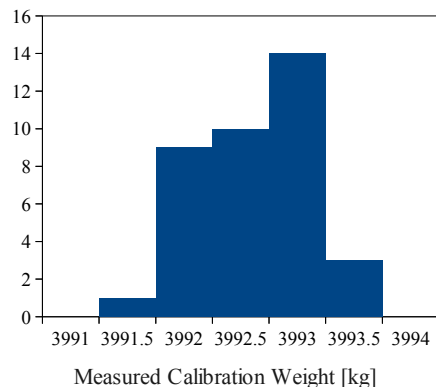


Figure 14. The distributions of measured weights of the four 1000 kg calibration weights collected at intervals during filling of the ISO tank in each filling campaign.

6.2 Coriolis massflow meters

Coriolis mass flowmeters are used to determine the mass of LS and MO in each detector. An additional Coriolis flowmeter is used as a backup measurement for GdLS in the event of problems with the load cells. Siemens Sitrans Massflo 2100 meters are used. For GdLS and LS, the specific model is the DI 6. MO's higher viscosity necessitates use of the slightly larger and less accurate model DI 15. Manufacturer specifications for the sensors indicate a maximum linearity error of 0.1% and a repeatability error of 0.05% (0.2%) for massflows greater than 50 kg/hr (280 kg/hr) for the DI 6 (DI 15).

Calibrations of the Coriolis flowmeters are done as part of each filling campaign and involve the calibration stand's polyethylene (PE) tanks and floor scale. The floor scale is calibrated using six 25 kg OIML class M1 calibration weights. After determining the scale calibration factor, LAB is pumped from one of the PE tanks into the other, through the flowmeter being calibrated. The LAB used was left over from scintillator production and differs from the LS (and GdLS) only in terms of wavelength-shifting components (and Gd dopant). For each meter, a total of ten calibration points are taken at two pump speeds. The GdLS flowmeter calibration point must be taken prior to starting the first ISO tank fill of a filling campaign, as LAB needs to be purged from the GdLS pump line prior to filling the ISO tank. The LS flowmeter calibration is typically done during the first ISO tank fill of each filling campaign. The MO flowmeter was calibrated twice - once before the first filling campaign and once before the last filling campaign. For each set of calibration points a correction factor is determined to bring the total Coriolis-measured mass into agreement with the mass difference measured by the calibration stand floor scale. In this comparison, scale readings are corrected for the mass of air replacing LAB in the calibration tank. Calibration factors are given by $C_{\text{scale}} \times (\Delta m_{\text{scale}} / \Delta m_{\text{Coriolis}})$ where C_{scale} is the previously-determined calibration scale correction. Results of these calibrations are

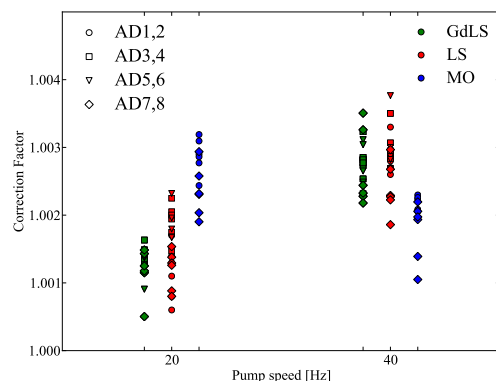


Figure 15. Correction factors determined from the calibration of the GdLS, LS and MO Coriolis flowmeters. Calibrations are conducted at two pump speeds so that a flow-rate dependent correction may be applied if required. The liquids have been visually separated for clarity.

shown in Figure 15.

6.3 Peristaltic pump

The GdLS metering pump cannot be used during the overflow tank filling due to materials compatibility concerns. By this time it has been stopped for several hours, and the stagnant GdLS inside the pump has been exposed to stainless steel, which can catalyze breakdown of the GdLS. Repurging the metering pump lines would be undesirable at this point, due to the complication this would cause in the detector liquid mass measurement. Thus a second pumping system with an independent, stainless steel-free, pump line is used to fill the GdLS overflow tanks. A small peristaltic pump moves liquid through this line.

Peristaltic pumps are commonly used for accurate delivery of small volumes of liquid, because the volume delivered by each stroke of the pump head is nearly constant. The peristaltic pump used for this application was a Cole-Parmer Masterflex I/P model EW-77970-27 digitally controlled peristaltic pump system. The tubing used was Saint-Gobain Performance Plastics Tygothane C-210-A, selected primarily for its good compatibility with GdLS. While Tygothane is not specifically designed for peristaltic pump use, our tests showed that it was well suited for light duty use in our pump. It is relatively stiff (Shore durometer hardness 82A), requiring a powerful pump to compress. It is inexpensive and could have been replaced between each detector fill, though this was not necessary.

The peristaltic pump line bypasses the GdLS Coriolis flowmeter. To maintain a completely redundant target mass measurement system, the peristaltic pump was instrumented with a rotary encoder. We mounted an AMT-103 rotary encoder from CUI Inc. to the outer casing of the peristaltic pump motor. Its quadrature outputs were connected to a counter input channel on one of the NI PXI-6283 DAQ cards.

We collected calibration points of the peristaltic pump system by delivering an arbitrary volume of liquid into a storage container, weighing the container before and after, and dividing the delivered mass by the number of rotations of the pump head. This was primarily used by the filling team to estimate GdLS mass added during overflow tank filling. It is also sufficiently accurate when combined with the GdLS Coriolis flowmeter uncertainty to provide a backup to the load cell-determined GdLS mass.

6.4 Calibration consistency and uncertainties

To increase confidence in the consistency of GdLS mass measurements, we compare the Coriolis-determined GdLS mass filled into the ISO tank to the difference in load cell weights when filling the tank in preparation for an AD fill. Similarly, we can compare the GdLS mass pumped through the GdLS coriolis meter into the AD to the difference in load cell weights when emptying the ISO tank into a detector. In addition to the individual instrument calibrations, this gives another sixteen points to check the repeatability of our mass measurement scheme. In this comparison, the Coriolis and load cell masses disagreed with each other by roughly 0.2%. Results are shown in Figure 16. This implies a potential bias in the absolute Coriolis or load cell calibration. Alternatively, there may be a difference in Coriolis flowmeter behavior between calibration and filling. The disagreement was consistently within 0.05%, which is the Coriolis flowmeter’s specified repeatability. Therefore, we conclude that the relative mass uncertainties between detectors is consistent within our ability to check it. This disparity does contribute to the absolute mass uncertainty. When determining the absolute number of expected inverse beta-decay events in each detector, our knowledge of the chemical composition of GdLS, not the total mass delivered, is the dominant uncertainty. Therefore, there is no physics motivation to resolve the disagreement.

6.5 Target mass measurement and determination of target protons

The expected number of inverse beta decay events in each Daya Bay antineutrino detector (AD) is directly proportional to the number of protons (Hydrogen atoms) in the target region of the AD. This number is proportional to the mass of gadolinium-doped liquid scintillator (GdLS) in the AD and the Hydrogen mass fraction in the GdLS. The measurement of $\sin^2 2\theta_{13}$ comes from a deficit of events observed in the far site ADs relative to the ADs at the two near sites. Thus, it is especially important to understand the relative difference between detector target masses. The filling system measures precisely the amount of GdLS put into each AD in total. To determine the mass in each AD’s target volume, corrections are made based on calculations of the volumes connecting the inner acrylic vessel to the overflow tanks and the time-dependent measurement of the volume of liquid in the overflow tanks. A summary of correction factors and their contributions to the relative and absolute target mass uncertainties are listed in Table 1. Contributions from the overflow tank mass measurements are discussed in detail in reference [10]. Overall, the relative uncertainty

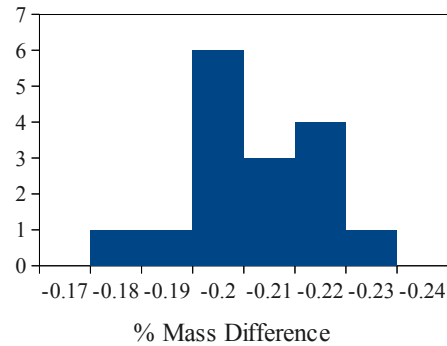


Figure 16. The percentage difference in mass measured by the GdLS Coriolis flowmeter compared to the load cells. The value of this difference is within the absolute uncertainty on the AD GdLS mass measurements and the spread is comparable to the GdLS Coriolis flowmeter’s repeatability specification.

Uncertainty source	σ [kg]
Total filled mass	3
Overflow tank volume	1.32
Overflow sensor calibration	1.14
Overflow tank tilt	1.37
Connecting volumes	0.5
Total	3.8

Table 1. Uncertainties on the target masses of Daya Bay’s antineutrino detectors that are uncorrelated between detectors. The dominant uncertainty is from the total filled GdLS mass. There is an additional 0.3% uncertainty on the absolute number of protons per kilogram and 0.2% uncertainty on the absolute mass calibration, but these are correlated between detectors and therefore do not impact the relative measurement of $\sin^2 2\theta_{13}$.

on target mass is dominated by the drift uncertainty from the load cells. It is nevertheless several times smaller than the originally projected uncertainty. The total filled masses and resulting target masses (averaged over the data period from [3]) for each detector are listed in Table 2.

Converting from target mass to target protons requires understanding of the chemical properties of the Daya Bay GdLS. Chemical analysis of the composition of samples from the detectors determined that the Daya Bay GdLS contains 7.169×10^{25} protons/kg [6]. Within the intrinsic measurement (0.3%) uncertainties, the measured hydrogen contents were identical for the two detectors. From these measurements, combined with the liquid mixing strategy discussed in Section 2.1, we conclude that the liquid is chemically identical in each detector and thus neglect the chemical composition contribution to the relative proton uncertainties. The 0.3% composition uncertainty is included in the absolute normalization

Detector	GdLS Mass/kg	Target Mass/kg
1	19992 ± 3.0	19941 ± 3.8
2	20022 ± 3.0	19966 ± 3.8
3	19954 ± 3.0	19889 ± 4.0
4	19988 ± 3.0	19913 ± 3.8
5	20049 ± 3.0	19989 ± 4.0
6	19963 ± 3.0	19891 ± 3.8

Table 2. Total Gd-doped scintillator masses and the corresponding target masses for the first six Daya Bay detectors. The masses of the seventh and eighth detectors are not currently known because of collaboration blinding during ongoing data analysis. Listed uncertainties are for components uncorrelated between detectors (the relative uncertainties).

uncertainty.

7. Summary

All eight antineutrino detectors have been successfully filled and installed. The filling pumps, valves and control programs worked reliably as designed. Although the in-situ liquid level measurements suffered from occasional noise the filling process was always well controlled. Detector monitoring cameras provided a reliable check on the liquid levels and arrival at filling stage transitions.

The mass of Gd-doped scintillator in each detector was determined by weighing the GdLS filled ISO-tank before and after filling. The relative total GdLS masses of different ADs were determined to 0.02% which is significantly more precise than the baseline 0.3% and original goal of 0.1% of the Daya Bay Technical Design Report [1]. The absolute expected signal rates in ADs scale with the number of target protons, requiring knowledge of the GdLS composition. A 0.2% disagreement was observed between the two mass measurement schemes for GdLS which may also be included in the absolute target proton uncertainty. In the determination of the absolute proton/kg, the 0.3% uncertainty in the chemical composition is assumed to dominate. Careful blending of GdLS sources during filling ensured that all ADs contain the same liquid composition. Calibrations and filling operations were conducted consistently between filling campaigns. We conclude that the relative uncertainty in the number of target protons between all filled detectors is 0.02%. For operational detectors in different halls, the inclusion of uncorrelated temperature fluctuations increases this uncertainty to 0.03%.

Acknowledgements

This work was performed with support from the DOE Office of Science, High Energy Physics, under contract DE-FG02-95ER40896 and with support from the University of Wisconsin.

The authors would like to thank Amy Pagac for supporting the design and drafting work for this project and providing several of the figures shown in this paper. We also thank Darrell Hamilton, Jack Ambuel, and Phil Robl for their assistance in the assembly and testing of the Daya Bay filling and target mass measurement system at the Physical Sciences Laboratory. We also gratefully acknowledge Raymonk Kwok, Kin Keung Kwan, Yadong Wei, Kai Shi, Kexi Cui, Ka Yu Fung, Talent Kwok, Jimmy Ngai, Henocho Wong, Patrick Tsang, Richard Rosero, and James Wilhelmi for their participation in filling the Daya Bay antineutrino detectors.

References

- [1] **Daya Bay** Collaboration, X. H. Guo et al., *Proposal of Daya Bay Experiment*, 0701029.
- [2] **Daya Bay** Collaboration, F.-P. An et al., *Observation of electron-antineutrino disappearance at Daya Bay*, *Phys.Rev.Lett.* **108** (2012) 171803, [arXiv:1203.1669].
- [3] **Daya Bay** Collaboration, F.-P. An et al., *Improved Measurement of Electron Antineutrino Disappearance at Daya Bay*, *Chinese Physics* **C37** (2013) 011001, [arXiv:1210.6327].
- [4] H. Band et al., “Assembly and Installation of the Daya Bay Antineutrino Detectors.” In preparation, 2013.
- [5] H. Band, R. Brown, J. Cherwinka, J. Cao, Y. Chang, et al., *Acrylic Target Vessels for a High-Precision Measurement of θ_{13} with the Daya Bay Antineutrino Detectors*, *JINST* **7** (2012) P06004, [arXiv:1202.2000].
- [6] M. Yeh et al., “Daya Bay Liquid Analysis.” Private communication, 2013.
- [7] H. Band, J. Cherwinka, M.-C. Chu, K. Heeger, M. Kwok, et al., *Daya Bay Antineutrino Detector Gas System*, *JINST* **7** (2012) P11029, [arXiv:1210.0643].
- [8] H. Band, J. Cherwinka, K. Heeger, P. Hinrichs, M. McFarlane, et al., *Low-Background Monitoring Cameras for the Daya Bay Antineutrino Detectors*, *JINST* **7** (2012) P08005, [arXiv:1204.3500].
- [9] Daya Bay Filling Team, <http://www.youtube.com/user/dybfilling>, 2013.
- [10] H. R. Band, J. J. Cherwinka, L. S. Greenler, K. M. Heeger, P. Hinrichs, et al., *Target Mass Monitoring and Instrumentation in the Daya Bay Antineutrino Detectors*, *JINST* **8** (2013) T04001, [arXiv:1206.7082].

